DEVELOPMENT AND VALIDATION OF HYBRID AUTOMATION INSPECTION AND ALGORITHM FOR AUTOMATIC DETECTION OF SURFACE DEFECTS IN PIPE MILL PROCESSES USING NON-DESTRUCTIVE TESTING

Lucas Kling e Silva

Tese de Doutorado apresentada ao Programa de Pós-graduação em Engenharia Metalúrgica e de Materiais, COPPE, da Universidade Federal do Rio de Janeiro, como parte dos requisitos necessários à obtenção do título de Doutor em Engenharia Metalúrgica e de Materiais.

Orientador(es): Gabriela Ribeiro Pereira

Werner Daum

Rio de Janeiro
Dezembro de 2020

DEVELOPMENT AND VALIDATION OF HYBRID AUTOMATION INSPECTION AND ALGORITHM FOR AUTOMATIC DETECTION OF SURFACE DEFECTS IN PIPE MILL PROCESSES USING NON-DESTRUCTIVE TESTING

Lucas Kling e Silva

TESE SUBMETIDA AO CORPO DOCENTE DO INSTITUTO ALBERTO LUIZ COIMBRA DE PÓS-GRADUAÇÃO E PESQUISA DE ENGENHARIA DA UNIVERSIDADE FEDERAL DO RIO DE JANEIRO COMO PARTE DOS REQUISITOS NECESSÁRIOS PARA A OBTENÇÃO DO GRAU DE DOUTOR EM CIÊNCIAS EM ENGENHARIA METALÚRGICA E DE MATERIAIS.

Orientadores: Gabriela Ribeiro Pereira
                 Werner Daum

Aprovada por: Profª. Gabriela Ribeiro Pereira
                Dr. Werner Daum
                Dr. Pedro Dolabella Portella
                Prof. Cesar Giron Camerini
                Prof. Leonardo Sales Araújo
                Prof. Juan Manuel Pardal

RIO DE JANEIRO, RJ - BRASIL

DEZEMBRO DE 2020

"Cause every night I lie in bed
The brightest colors fill my head
A million dreams are keeping me awake
I think of what the world could be
A vision of the one I see
A million dreams are all its gonna take
A million dreams for the world we're gonna make"

Benj Pasek

*Dedico este trabalho a minha amada
esposa e aos meus queridos pais que são
os pilares e a motivação da minha vida.*

ACKNOWLEDGEMENTS

Resumo da Tese apresentada à COPPE/UFRJ como parte dos requisitos necessários para a obtenção do grau de Doutor em Ciências (D.Sc.)

DESENVOLVIMENTO E VALIDAÇÃO DE INSPEÇÃO AUTOMÁTICA HÍBRIDA E ALGORITMO PARA DETECÇÃO AUTOMÁTICA DE DEFEITOS SUPERFICIAIS EM PROCESSOS DE PRODUÇÃO DE TUBOS UTILIZANDO ENSAIOS NÃO DESTRUTIVOS

Lucas Kling e Silva

Dezembro/2020

Orientadores: Gabriela Ribeiro Pereira
Werner Daum

Programa: Engenharia Metalúrgica e de Materiais

Produtos tubulares de alta performance e qualidade são essenciais para a indústria de óleo e gás desde a extração destas commodities até a distribuição do produto para a sociedade. Os produtos tubulares e as ferramentas utilizadas para fabricação destes produtos são rigorosamente controladas pelos processos de qualidade industriais, tendo como sua principal etapa as inspeções não destrutivas. Desta forma, o desafio de detectar, monitorar e avaliar em tempo real estados de dano e defeitos são de grande relevância. Neste contexto, a inspeção de superfícies por tecnologias que possam ser aplicadas e monitoradas durante o processo produtivo, sem afetar o ciclo de produção, ganham grande importância, pois asseguram ainda mais a qualidade dos materiais produzidos além de habilitarem o ambiente fabril para as novas possibilidades da indústria 4.0. Neste trabalho foi desenvolvido uma metodologia de inspeção não destrutiva, baseada em correntes parasitas e métodos ópticos 3D, visando a automação da inspeção de superfícies para a indústria de produtos tubulares. Para tal, um protótipo foi construído e testado em ambiente fabril e um algoritmo para análise e classificação dos defeitos foi também desenvolvido. Os resultados alcançados com o sistema de inspeção, sensores e algoritmo, desenvolvidos neste trabalho, demonstraram a viabilidade da aplicação do sistema em ambientes industriais visando tanto a inspeção de ferramentas, quanto de produtos tubulares.

Abstract of Thesis presented to COPPE/UFRJ as a partial fulfilment of the requirements for the degree of Doctor of Science (D.Sc.)

DEVELOPMENT AND VALIDATION OF HYBRID AUTOMATION INSPECTION AND ALGORITHM FOR AUTOMATIC DETECTION OF SURFACE DEFECTS IN PIPE MILL PROCESSES USING NON-DESTRUCTIVE TESTING

Lucas Kling e Silva

December/2020

Advisors: Gabriela Ribeiro Pereira
          Werner Daum

Department: Metallurgical and Materials Engineering

High performance and quality tubular products are essential to the oil and gas industry, from the extraction of these commodities to the distribution of the product to society. Both the tubular products and the tools used to manufacture these products are strictly controlled by the industrial quality processes, having as its main stage the non-destructive inspections. Therefore, the challenges of detecting, monitoring and evaluating in real time the damage and defects are very relevant. Within this context, the inspection of surfaces by technologies that can be applied and monitored during the production process, without affecting the production cycle, gain great importance since they further ensure the quality of the materials produced and enable the manufacturing environment for the new possibilities of industry 4.0. The work carried out in this thesis develops a non-destructive inspection methodology, based on Eddy currents and 3D optical methods, aiming at the automation of surface inspection for the tubular products industry. For this purpose, a prototype was built and tested in a factory environment and an algorithm for analysis and classification of defects was also developed. The results achieved with the inspection system, sensors and algorithm developed in this work, demonstrates the feasibility to apply the system in industrial environments aiming at both the inspection of tools and tubular products.

Table of Contents

List of Figures

List of Tables

List of abbreviations

Automatic Defect Classification (ADC)

Computer Numeric Control (CNC)

Discrete Cosine Transforms (DCT)

Eddy Current (EC)

Finite Element (FEM)

Fuzzy Logic (FL)

Hall sensor Geometric Profilometer (HGP)

Laser Line (LL)

Membership Function (MF)

Multi-Layer Perceptron (MLP)

Naïve Bayes Network (NBN)

Non-Destructive Testing (NDT)

Photon Mixer Device (PMD)

Singular Value Decomposition (SVD)

Structured Light Scanning (SLS).

Support Vector Machine (SVM)

Time Of Flight (TOF)

1. Introduction

High performance and quality tubular products are essential to the energy sector, as an example, the oil and gas industry, where tubular goods are used to extract these commodities, in onshore or offshore environments, to the distribution of the final product to society. Both the tubular products and the tools used to manufacture these products are strictly controlled by an industrial quality process, having as its main stage the non-destructive inspections. Therefore, the challenge of detecting, monitoring and evaluating in real time damage and defects in both the production tools and the products are very relevant. Within this context, the inspection of surfaces by technologies that can be applied and monitored during the production process, without affecting the production cycle, gain great importance since they further ensure the quality of the materials produced and enable the manufacturing environment for the new possibilities of industry 4.0.

Non-destructive testing (NDT) methods are being used on a pipe mill, but there is still a gap for new developments for the automation of the NDTs for surface inspection. The most relevant companies of tubular goods industry have an integrated and continuous pipe mill, producing on average one pipe every minute. These pipes are submitted to several quality processes during its production, held trough non-destructive inspections to attend the necessary quality standards of the product and specification of the customers, being the surface inspection one of the most important and strategic inspection stage (EN 13018, 2016). The surface inspection of pipes has to detect superficial defects that are typically created on inner and outer surfaces of pipes. These defects mostly occur on the outer surface of pipes, due to imperfections on the outer surfaces of the rolling tools used during the rolling process, heavy mechanical handling, and up to the very last handling process. Generally, these defects are superficial holes, dents, "molly whopper" or bore slag, mechanical marks and straightening machine marks that make the traditional NDT techniques not efficient enough in detecting them. Besides these defects, the mechanical-metallurgical process used in the production of seamless pipes can itself cause the formation of other defects, such as folds and bends.

However, the surface inspection usually performed through visual inspection is highly dependent on the inspector who performs it, since the only document generated after the inspection is the technical report created by the operator that determines

whether or not the pipe is to be sent to the next inspection steps. Thus, the surface inspection, does not produce enough information for a later verification of the test results, when necessary, and do not attend the new time frame of the production line, so that companies remain competitive on the market. In addition, there is also a physical limitation and time constraints for this kind of procedure, since the inspector would have to inspect a nearly twelve meters long pipe about every minute. These issues can lead to occasional approvals of non-conforming pipes resulting not only in wastage of resources in further stages of the quality process, but also undermine the reliability of the quality assurance process. Therefore, the need for a new way to improve the visual inspection evaluation is clearly needed to, perceptible that not only meets the needs of production line speed, but also the necessity and inherent quality of the pipes (AZANI, GUITIERREZ *et al.*, 2008).

A surface inspection solution that embraces inspection methodology and data processing regarding the boundary conditions of industrial production is not currently found commercially on the market to be applied respecting the industrial production environment. To this end, the present work studied electromagnetic and optical techniques in order to develop an inspection methodology capable of detecting surface defects that occur during the production of seamless tubes. Besides that, it is of fundamental importance that the process does not interfere with the lead time of production and therefore data should be evaluated automatically and in real time. The defects evaluation is understood not only in the detection of imperfections, but also in their dimensioning and possible classification. For that purpose, an algorithm was developed to evaluate simultaneously the raw data from these techniques in order to automatically recognize and classify the defects in-line and on-line.

For the development of this project, the structured light system was initially used to inspect the surface of the pipes samples with the defects, generating the reference data of this project. Based on the data obtained, the algorithm of the proposed algorithm was developed and validated. Additionally, two inspection methodologies based on Eddy current and laser scanning were developed and optimized to meet the presented boundary conditions, as well as their results were processed and analyzed in the developed algorithm.

The results obtained show the efficiency and complementation of the electromagnetic and optical techniques developed, being able to detect defects with approximate dimensions of up to 1 mm³ and the algorithm developed showed to be able

not only to recognize the defects automatically, but also to classify them based on their geometry and orientation, having just small deviations. Thus, the proposed solution has a great potential for industrial application in order to improve the quality of pipes' surface without modifying the production lead line.

2. Theoretical bibliographic review

1.1 Electromagnetic techniques

2.1.1. Eddy current

The Eddy Current (EC) test, also known as Foucault Current, is a non-destructive inspection technique based on the introduction of an alternating electrical current in the material to be inspected and the observation of the interaction between the magnetic field generated by the probe and the induced one in the material inspected (BOWLER, 2019).

The basic principle of EC operation is similar to that of a transformer, where the probe coil corresponds to the primary component and the material inspected to the secondary component of the transformer. According to the law of Ampère, when a coil is excited by an alternating current, a primary alternating magnetic field is generated. By approaching this coil to the surface of an electrically conductive material, the field generated by the coil induces an electric current in the material, named as "eddy currents". These generated currents give rise to a new magnetic field, known as a secondary field, which if opposes the variations of the primary field. The interaction between the primary and secondary fields modifies the electrical impedance of the coil and such a variation of impedance is the physical variable monitored during the test, as can be seen in Figure 2.1 (CAMERINI, 2018) (MARTIN, 2011).
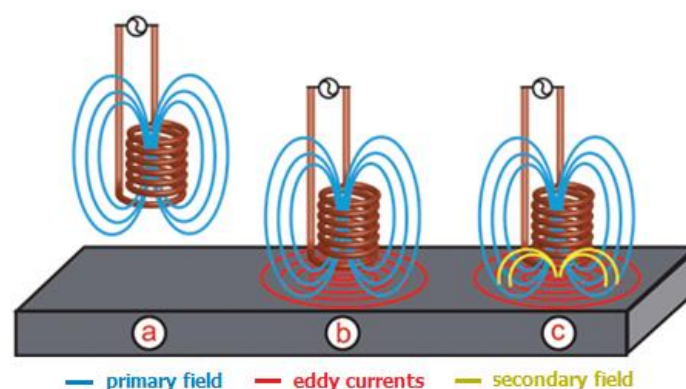
Figure 2. 1: EC inspection principle: a) generation of primary magnetic field, b) induction of an electric current, c) generation of secondary magnetic field. Adapted from (OLYMPUS, 2019).

If the region of the inspected material has some discontinuity, it will present a flow of ECs smaller than the regions exempt from them, because the defective region will have greater resistance to the passage of electric currents. This difference in EC flow results in a change in coil impedance, which is constantly monitored, being possible to differentiate between regions with and without defect. On the other hand, if the material presents microstructural variations, they also generate changes in the flow of ECs, locally modifying permeability and electrical conductivity, making it possible to compare the microstructure between different materials. The signal measured thereon will depend on the geometrical characteristics of the coil, the test frequency, the electrical and magnetic properties of the material, the sample dimensions and the existence of discontinuities in the sample (CORREA, 2017).

In the testing of ECs, the use of reference standards in the adjustment and calibration of the equipment is essential, since the signals are affected by many different variables. In consequence, small changes (gain, rotation and etc) in the configuration of the equipment can drastically change the appearance of a signal, defining this technique as comparative. As with most non-destructive testing methods, the most useful information is obtained when you compare the results of an unknown object with the results of a similar object, with well-known characteristics and defects (CORREA, 2017). Some of the advantages and limitations of the ECs over other non-destructive techniques are resumed in the Table 2.1 (SILVA, 2018).

Table 2. 1: Advantages and limitations of EC test (SILVA, 2018).

Advantages	Limitations
It is highly sensitive to small cracks and defects on the surface and subsurface.	The material needs to be conductive.
The material to be analyzed needs little or no preparation.	More operational ability and training are needed to use this technique.
The probe could have no contact with the material.	The location of the discontinuity cannot be parallel to ECs.
Capable of inspecting materials with complex geometries and various sizes.	Calibration reference is needed.
In general, the equipment has relatively low cost.	Limited penetration depth.
Several sensors can be associated to perform a full body inspection at once.	Surface roughness can cause high interference.

One of the great advantages of EC technique over other non-destructive methods is that it does not require physical contact between the coil and the specimen to be inspected, because it is based on the principle of electromagnetic induction. However, a limitation compared to other conventional NDT techniques, such as ultrasound, is the penetration capability into the inspected material. In thick and/or high magnetic permeability materials, limited penetration of the EC technique makes the inspection only possible for the surface or subsurface layers (CAMERINI, 2012). This occurs because electric currents have maximum density on the surface that decreases as they penetrate the material. The pellicular effect, or skin effect, is responsible for this fall and acts as follows: ECs are generated on the surface, which create a secondary field that opposes the primary, reducing it. Thus, the layer just below the surface is influenced by a smaller primary field, reducing the induced currents (GRIFFITHS, 1999). It has been verified that there is an exponential relationship between the depth and density of currents. The depth at which the current intensity is decreased to 36.8% (1/e*100%) of its surface value is defined as the standard penetration depth (δ). A relationship can be developed between the frequency of excitation (f), the electrical conductivity (σ) and the magnetic permeability (μ) with the standard depth of penetration of the material, as observed in the Equation 2.1 (SILVA, 2016).

$$\delta \cong \frac{1}{\sqrt{\pi f \mu \sigma}}$$ Equation 2. 1

Since electrical conductivity and magnetic permeability also influence penetration depth, ferromagnetic materials (which have high magnetic permeability) will exhibit induced ECs with reduced penetration depth. By reducing the frequency of excitation, a greater depth of penetration is achieved; however, the current density at the surface is reduced. Therefore, it is necessary to select a given optimal operating frequency, so that it is sufficient to ensure the flow of ECs with a good penetration depth, as illustrated in Figure 2.2 (CORREA, 2017).
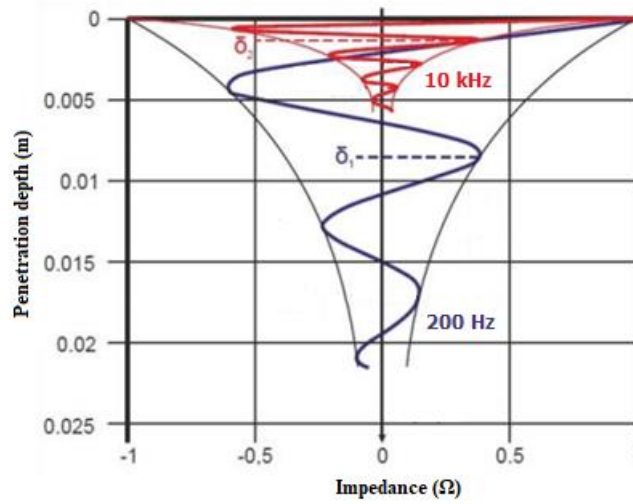
Figure 2. 2: Penetration depth for frequencies of 200 Hz and 10 kHz for a ferromagnetic steel. Adapted from (CORREA, 2017).

Electrical impedance (Z) is the total opposition that a circuit offers to the flow of an electric current variable in time. Impedance is measured in ohms (Ω) and can be expressed as a complex number, having a real part, equivalent to resistive component (R), and an imaginary part, given by inductive reactance (X_L) and capacitive reactance (X_C), as can be seen in Equation 2. However, operating in frequency bands up to a few MHz, the influence of capacitive reactance is negligible, so only the inductive reactance is usually considered (ABU-NABAH, NAGY, 2007) (ABU-NABAH, 2018).

$$Z = R + j(X_L + X_C) \xrightarrow{f>MHz} Z = R + jX_L$$ Equation 2. 2

The relevant components are, therefore, X_L and the R that can be represented in a vector diagram in which X_L is on the ordinate axis and R on the abscissa axis, as can be seen in Figure 2.3 (NDT RESOURCE CENTER, 2019). The term "impedance plane" is used to designate this diagram, which, in general, is how the EC equipment presents the results to the operator. What the equipment measures are the amplitude and phase of a received signal in relation to the coil excitation signal (FREITAS, 2009).
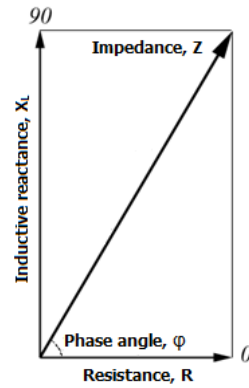
Figure 2. 3: Impedance plane diagram. Adapted from (NDT RESOURCE CENTER, 2019).

Generally, the variation in signal amplitude shows discontinuities, and the variation in phase angle shows changes in material properties. The analysis of the results of an EC inspection from the impedance plane is the most usual way and is present in most commercial equipment (BOWLER, 2019). The impedance plane, of Figure 2.4, illustrates the variation of impedance according to the magnetic properties of the material (SILVA, 2016).
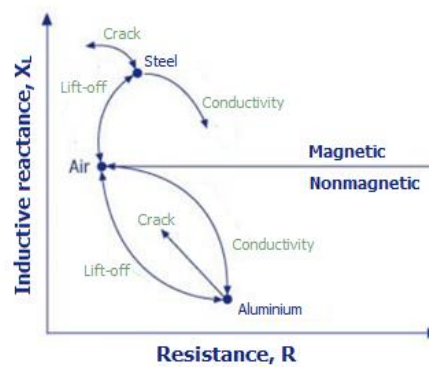
Figure 2. 4: Impedance variation generated by the change of the inspected material properties. Adapted from (SILVA, 2016).

The curve behavior is different for ferromagnetic and non-ferromagnetic materials. Although, in the both cases, they have the same starting point, called the "equilibrium point". It indicates when the probe is in the air, acting only with the primary magnetic field (SILVA, 2018). Approaching the probe, positioned in air, to a non-ferromagnetic material, (as the aluminium in Figure 2.4), the resistive component

increases as the ECs are generated in the material, draining energy from the coil. The inductive reactance, however, decreases due to the magnetic field generated by the currents that opposes the coil, resulting in a smaller magnetic field for the inductance. In other hand, when the probe approaches a ferromagnetic material (as the steel in Figure 2.4), there is a different behavior than that of non-ferromagnetic materials. In this case, the inductive reactance increases given its high magnetic permeability, which concentrates the magnetic field of the coil in the steel. This concentration overlaps with the magnetic field generated by ECs, becoming a predominant field (GARCÍA, GIL *et al.*, 2011) (CHAIBA, AYAD *et al.*, 2018).

A major advantage of EC testing is that the probe can be developed according to the desired application. There are several types of EC probes that are classified according to the mode of operation and the configuration of the coil. Below will be described the main arrangements used in inspections.

Differential inductive probes:

Consisting of two coils, the differential probes are characterized by their response being a signal of difference between the coils that compose the probe. Being the constituent's coils of the probe with the same parameters, however with the inverted polarity, the field generated by both coils is the same in module, but with inverted direction. Figure 2.5 presents an example of a differential probe composed by two independent coils and the signal generated by a differential probe passing through a defect. This signal in format of a "loop" or a butterfly tie is characteristic of differential probes and is known as lissajou (García, Gil *et al.*, 2011) (CAMERINI, 2012).

a)   b)
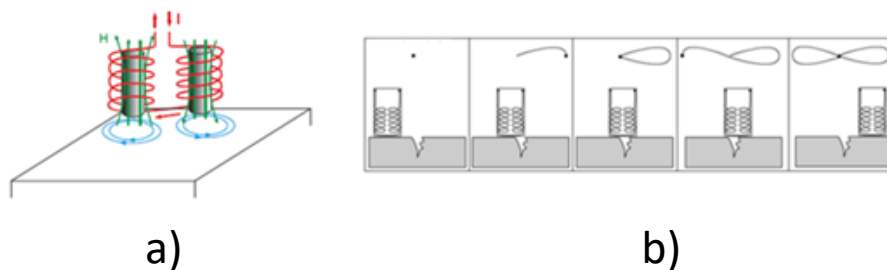
Figure 2. 5: Smaller characters: a) Example of a differential probe composed by two independent coils; b) Illustration of the signal generated by a differential probe passing through a defect (CAMERINI, 2012).

The most notably advantage of this configuration is the capacity to detect small defects due to its great sensitivity. However, one disadvantage is that the signals may be difficult to interpret, since they are composed by a difference of two absolute signals, increasing the data analysis complexity. Many methodologies directly applied to analyze the absolute signals, therefore, must be adapted to this kind of signal, and, oftentimes, the information given by them is intrinsically different. For example, when it comes to very large defects, where the length of the defect is greater than the spacing between the coils, the signal inside the defect can often be "zero", or have its intensity greatly reduced. This happens because both coils are with the same response of the defect, what does not mean, however, that the defect does not exist (CAMERINI, 2012).

Hybrid probes:

They are probes based on magnetic field measurement using magnetic field sensors. These sensors can be: SQUID, Hall effect, anisotropic resistance magnet (ARM), giant magneto resistance (GMR), etc, and will be further explored in the next section (KRAUSE, KREUTZBRUCK, 2002) (EISENBEIS, 2014). These sensors usually have small dimensions, high sensitivity for a wide frequency range, low noise and low cost (CORREA, 2017).

A very common hybrid configuration is the mixing of differential and reflection probes, where the windings for detection are in a differential configuration and the coil of excitation involving them (CAMERINI, 2012). The sensors are placed close to the surface where the ECs are created, as can be seen in Figure 2.6 (CORREA, 2017). It can also be noted that although the combination of the solid state sensor with EC is an excellent tool to improve the test response, it is important to note that solid state sensors generally have a limitation in relation to their frequency and EC testing is usually performed at higher frequencies. Therefore, it is important to pay attention to the compatibility of the frequencies of action during the test.
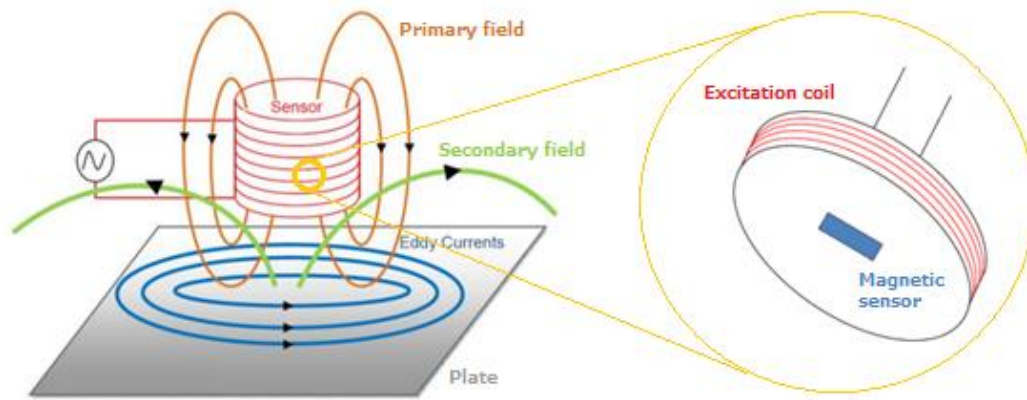
Figure 2. 6: Positioning of the magnetic sensor in the center of a coil. Adapted from (CORREA, 2017).

An example of a hybrid probe is one that uses a Hall effect sensor to detect changes in the magnetic flux leaking from the test surface. Hybrid probes are usually specially designed for a specific inspection application (NDT RESOURCE CENTER, 2019). However, these secondary sensors can be also applied independently of the EC probes, even though associated to its results. For example, when Hall sensors are used in profilometry systems, been capable of reconstruct surface defects in parallel with the EC, as will be showed in the next section.

Comparison between different magnetic field sensors:

The selection of the most suitable sensor type for the EC probe depends of several parameters that determine its efficiency. These parameters include, for example, the magnetic field range, the operating frequency band and sensor dimensions (GARCÍA, GIL *et al*., 2011). As showed before, in the common EC test probes, the coil acts as the magnetic sensor itself, but other types of sensors can be used in hybrid probes.

The use of coils as transducers offers the advantage of being very precise, robust, easy to build, and have a good signal-to-noise ratio (PEREIRA, 2014). As well, they have a huge dynamic range and the possibility of focusing the sensor. Although, the main disadvantages of their utilization are the high induction voltage at the start of the signal and the fact that, at a certain scale, they are difficult to make smaller, different of Hall sensors, for example, that can be easily miniaturized and integrated within microelectronic circuits (GARCÍA, GIL, *et al.*, 2011). Silva (2018) organized several

works with different probes highlighting the most important parameters used during inspection, as can be seen in Table 2.2 and Table 2.3.

Table 2. 2: EC studies using different magnetic field sensors for subsurface crack detection – Part 1 (SILVA, 2018).

Author	Year	Frequency	Defect width (mm)	Defect length (mm)	Defect height (mm)	Depth (mm)	Type of core
PICK-UP PROBES							
MOOK	2006	350 Hz	3	100	3	8.5	Air
		100 Hz	<0.1	-	25	22.5	Air
		50 Hz	<0.1	-	25	28.8	Air
ALMEIDA	2013	100 kHz	-	-	7	3	Air
CARISTEDT	2014	100 Hz	12	2	2	6	Air
ABSOLUTE PROBES + GMR SENSOR							
DOGARU	2001	1.5 kHz	15	0.5	2	1.5	Air
SIKORA	2003	10 - 120 Hz	0.5	-	4	16	Air
TSUKADA	2006	50 Hz	1	25	1	6	Air
YAMADA	2006	50 Hz	1	25	1	8	Air
WINCHESKI	2010	185 Hz	0.13	14	1	9	Air
HAMIA	2010	325 Hz	0.5	50	2	8	Air
CACCIOLA	2010	60 Hz	2	2	4	4	Air
DIRAISON	2009	200 Hz - 4 kHz	0.5	2 - 10	2	7.7	Air

Table 2. 3: EC studies using different magnetic field sensors for subsurface crack detection – Part 2 (SILVA, 2018).

Author	Year	Frequency	Defect width (mm)	Defect length (mm)	Defect height (mm)	Depth (mm)	Type of core
ABSOLUTE PROBE							
ROSELL	2012	900 Hz	0.28	12.6	5	3.04	Air
LU	2012	100 Hz - 10 kHz	-	-	-	5	Air and ferrite
BOHACOVA	2013	450 Hz	-	-	-	4	Air
DIFFERENTIAL PROBE							
KIM	2012	300 kHz	0.15	2 - 8	-	3	Air
DIRAISON	2009	200 Hz - 4 kHz	0.5	2 - 10	2	7.7	Air

Some works will be better discussed in section 3.1, explaining better some important parameters and limitations for the probes and their applications.

2.1.2. Eddy current and computational simulation

Computational simulation has as one of its main purposes the execution of a mathematical model that reproduces in detail the real system in order to study its behavior (CAMERINI, 2018). Usually a simulation refers to a computational implementation of the model, which is run over time under different conditions to study the interactions between the constituent parts of a system. This means that from a simulated model that accurately represents reality, it is possible to make changes to the model in a simple and fast way, without the need to leave the virtual environment, thus reducing the need for long experiments (CAMERINI, 2012) (KARTHIK, MATHIALAKAN, *et al*., 2015).

The most common calculation method in EC simulators is the finite element method (FEM). The FEM is known as a mathematical model analysis method to represent physical problems. This modelling is done through differential equations with

their respective boundary conditions, solved from a division of the integration domain ("mesh" or "grid") in a finite number of small regions ("finite elements"). From the mesh, functions are searched that satisfy the conditions in each element, and not in the entire domain (SILVA, 2018).

The electromagnetic phenomena are described by Maxwell's equations that involves five vectors, dependent on position and time, being them: electric field ($\vec{E}$), magnetic field ($\vec{H}$), magnetic flux density ($\vec{B}$), electric flux density ($\vec{D}$) and current density ($\vec{J}$) (CAMERINI, 2012). The description Maxwell's laws containing these vector quantities are shown from Equation 2.3 to 2.6. being respectively Faraday's Law, Ampère's Law, Gauss's Law for the electric field and Gauss's Law for the magnetic field.

$$\vec{\nabla}.\vec{E} = -\frac{\partial \vec{B}}{\partial t}$$

Equation 2. 3

$$\vec{\nabla}.\vec{H} = \vec{J} - \frac{\partial \vec{D}}{\partial t}$$

Equation 2. 4

$$\vec{\nabla}.\vec{D} = \rho$$

Equation 2. 5

Being ρ the electrical charge density.

$$\vec{\nabla}.\vec{B} = 0$$

Equation 2. 6

For the simulation of ECs, the calculation of the magnetic potential vector is fundamental, because from its value it is possible to obtain other electromagnetic quantities such as: magnetic flux density, coil impedance and other parameters (SILVA, 2018). One of the most used applications to simulate this type of inspection is COMSOL Multiphysics, a cross-platform finite element analysis, solver and Multiphysics simulation software. As described by Camerini (2012), the EC simulations with COMSOL usually consists of working in models with axial symmetry, where the variable is the magnetic potential vector (A). In it, the main steps to perform the simulation consist of:

- Use the AC/DC module, choosing to work with induced currents in two dimensions with axial symmetry;

- Define the limit region, draw the coil and the core, which are the subdomains of the model;

- Specify the magnetic and electrical properties of each subdomain, as well as the external current density of the coil;

- Define the boundary conditions of the problem;

- Define the frequency to be used;

- Create the finite element mesh.

Therefore, software as COMSOL permits the simulation EC test to qualitatively analyze the main parameters that compose a probe (core and coil geometry, applied current density, metallurgical properties of the core, operating frequency and others). Finally, from this evaluation, it is possible, for example, to define optimal parameters for the probe construction (CAMERINI, 2012), reducing costs and time.

2.1.3. Solid state magnetic field sensors

Solid state sensors are characterized for having no mobile parts and must not be confused with transducers or actuators which react depending on the sensor response (GIACHINO, 1986). Among these, the magnetic field sensors, often called "magnetometers" (HEREMANS, 1993), have been fundamental for humanity in various applications since their invention. The hard drives that allowed the advance of computation, reliable noncontact switches that elevated the safety standards of airplanes, position determining sensors for various automobiles parts, and much other are just few examples of technologies only made possible by the existence of magnetometers, without even mentioning their substantial role in advanced medicine, factoring and research.

There are many techniques to sense magnetic fields, most of them based on the intimate connection between magnetic and electric phenomena. Therefore, comparing various magnetic sensors for one desired application, different parameters should be considered – sensitivity, linearity, range, frequency bandwidth, dimensions and, mainly, the range of measured magnetic field. In this range, the smallest value is especially important, since the upper limit of this kind of sensors can theoretically be very large

(TUMANSKI, 2013). In the Table 2.4 and 2.5. the characteristics of common magnetic sensors are resumed (TUMANSKI, 2013) (POPOVIC, FLANAGAN, *et al*., 1996) (JANDER, SMITH, *et al.*, 2005).

Table 2. 4: Characteristics of common magnetic sensors – Part 1.
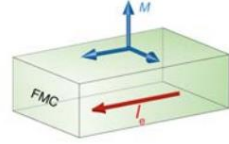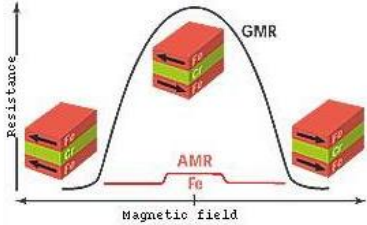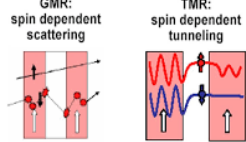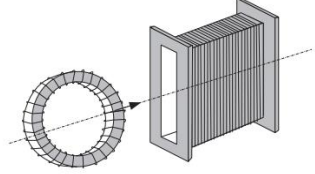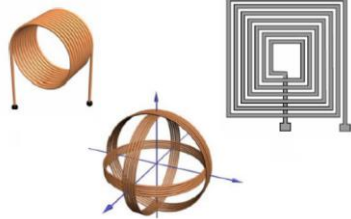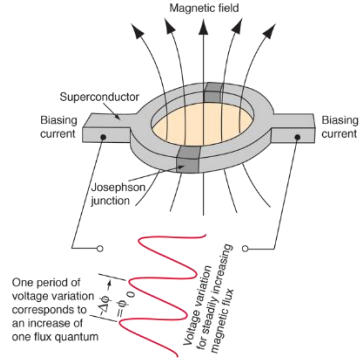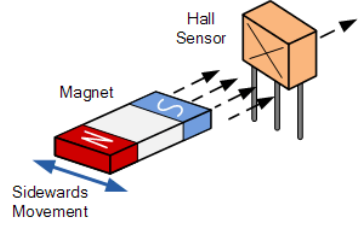
Sensor type		Physical principle	Illustrations
	AMR	Based on ferromagnetic metals or alloys that exhibit an anisotropic resistivity in a magnetic field.	
Magneto resistors	GMR	Is an alternation of conductive layers with set magnetization and layers with magnetization which can align themselves with an external magnetic field, acting as a spin filter.	
	TMR	Similar to GMR sensors with one difference – instead of only conducting layers it is used thin insulating spacers.	
Fluxgate sensors		Consists of a ferromagnetic core wrapped with two coils, whose induction changes in the presence of an external magnetic field.	
Induction sensors		Is usually in form of a coil (with or without ferromagnetic core) and according to the Faraday's law the generated voltage V is proportional to the rate of change of magnetic field.	

Table 2. 5: Characteristics of common magnetic sensors – Part 2.

Sensor type	Physical principle	Illustrations
SQUID	Consists of two superconductors separated by thin insulating layers to form two parallel Josephson junctions. Can be configured as a magnetometer to detect incredibly small magnetic fields - small enough to measure the magnetic fields in living organisms.	
Hall Effect sensor	The Hall effect is a property that manifests itself in a conductor when a magnetic field perpendicular to the current flow is applied on it. When this occurs, an electric potential difference in the conductor is generated, called Hall voltage. A Hall sensor is a semiconductor transducer based on this principle.	

Among these sensors, the Hall sensors will be discussed in more detail due to its interesting characteristics for inspections based on electromagnetic NDT.

A Hall Effect sensor is a semiconductor transducer that responds under a magnetic field with a change in its output voltage. The Hall sensor has its working principle based on the Hall effect, discovered in 1889 by Edwin Herbert Hall. However, its application was restricted to laboratory experiments until 1950. The Hall effect is a property that manifests itself in a conductor when a magnetic field perpendicular to the current flow is applied on it. When this occurs, an electric potential difference in the conductor is generated, called Hall voltage, as can be seen in Figure 2.7 (CORREA, 2017) (ALI, YANLING, *et al.*, 2017).
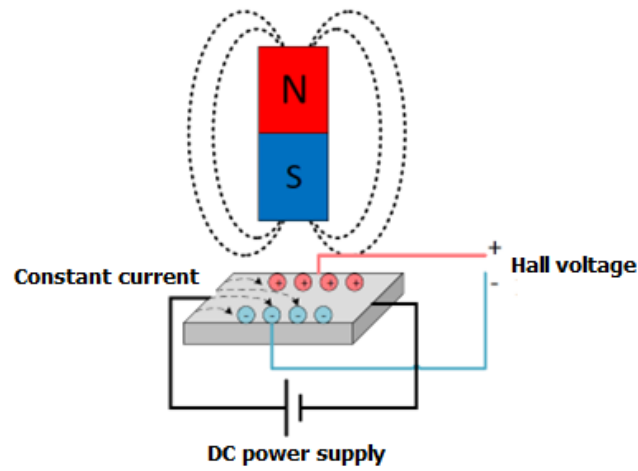
Figure 2. 7: Hall sensor functioning representation. Adapted from (CORREA, 2017).

This voltage has direction perpendicular to the magnetic field and current, besides that it is proportional to both the magnetic flux density and the current that travels the conductor. The applied magnetic field causes a gradient of concentration of charge carriers throughout the conductor, generating a potential differential expressed in a voltage value. The Hall effect sensor has a linear response and can operate from DC fields up to 100 kHz frequencies. It allows directional detection and its size is relatively small, with the possibility to be easily miniaturized for electrical circuits, for example. In addition, it can withstand large magnetic fields without saturation (CORREA, 2017).

The Hall probe consists of a thin semiconductor plate with two biasing contacts, through which the biasing current (I) flows, and other two contacts to measure the Hall voltage (V_H), the sense contacts (ALI, YANLING, *et al.*, 2017). This configuration is illustrated in Figure 2.8 and is described by the Equation 2.7.
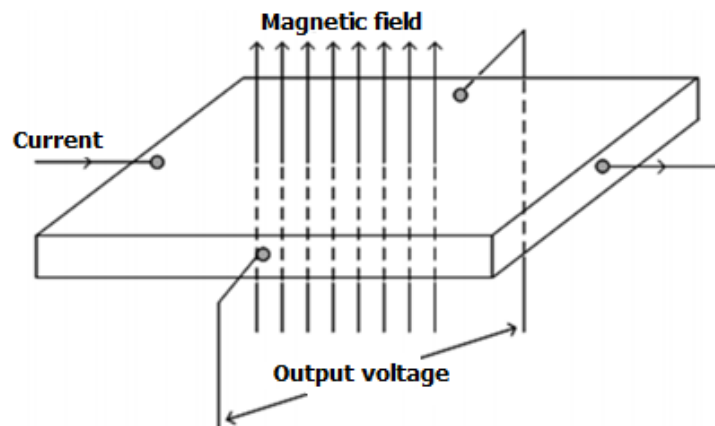
Figure 2. 8: Hall sensors contacts configuration (ALI, YANLING, *et al.*, 2017).

$$V_H = \frac{r_n}{qnt} GBI \qquad\qquad \text{Equation 2. 7}$$

Where I is the biasing current in amperes, q is the charge on an electron equal to 1.6×10^{-19} C, n is the carrier concentration, t is the plate thickness r_n is the scattering factor, G is the geometrical correction factor and B is applied magnetic field density.

The noise is one of the main limiting factors of this sensor efficiency. Noise determines the smallest detectable magnetic field. Various sources of noise are generated by the Hall device itself. They are due to thermal noise, generation-recombination noise and flicker noise, with the total noise described as the sum of these three types (ALI, YANLING, *et al.*, 2017). Other disadvantages are their limited sensitivity due to the silicon, and the relatively large offset (NOVKOVSKI, 2006), which is defined by a "measurement shift caused by the residual flux of the magnetic core in the transducer" (PORTAS, COLOMBEL, 2007). However, for some applications, other sensors types as SQUIDs and GMRs with very elevated sensitivities are unsuitable, turning the hall sensors the best options, beside their simplicity.

For applications where measurement of a weak magnetic field at low temperatures is required, Hall sensors made of materials with high mobility and a small energy band gap are used. This is because these materials have a high-frequency response. However, such materials possess low operating temperatures and frequency limit since it doesn't work above 5 kH. Other advantages of hall sensors in comparison to other magnetic sensors are: simple design and technology of manufacturing, thus, in general, are very cheap; possibility to design very small sensors, with dimensions of less than one µm and less invasive measurement of magnetic field due to the lack of ferromagnetic elements, although supplying current can generate small magnetic field (TUMANSKI, 2013).

Even though, magnetic field measurements are considered a usual application for Hall sensors (TUMANSKI, 2013) they can also be used for mechanical measurements (proximity sensors, sensors in brushless motors and others) (Patent No. US8270254/EP2269054. 2009).

The Hall sensors are solid-state magnetic field sensors with a worthy set of characteristics. They can be easily miniaturized for electrical circuits, can withstand large magnetic fields without saturation and have a high suitable sensitivity for a large set of applications. Among these, in the superficial and sub-superficial defect detection field, they can not only be used as sensors for the EC test response magnetic field measurement, but also independently, in mechanical profilometry, for example. This

application is very interesting since it can provide more information about the same superficial damage than EC test, but with a different physical principle and different characteristics. Therefore, systems that integrate the Hall sensors to EC test have been more and more explored and constantly developed by the research institutes and the industry.

1.2   Optical 3D techniques

The 3D reconstruction of short distance objects surfaces by optical techniques is one of the most explored current subjects in the fields of digital photometry, computer vision and object recognition. This fact is due to the massive improvement of computational resources, to the large number of already available commercial and potential applications in several areas. But only with most recent progress in sensor technology and processing power, they have become accurate, fast and versatile enough to be widely used. The Table 2.6 shows the evolution of the specifications of common commercial image processing systems since 1985 (BREUCKMANN, 2014).

Table 2. 6: Typical specifications of commercial image processing systems (BREUCKMANN, 2014).

Year	CPU / RAM	Image Memory	HD capacity	Resolution
1985	512 KB	2 MB	20 MB	256 KPixel
1990	2 MB	16 MB	100 MB	1 MPixel
2000	200 MB	100 MB	GB	4 MPixel
2010	4 GB	2 GB	TB	8 MPixel
2014	64 GB	32 GB	TB	16 MPixel

The 3D reconstruction has been widely used in medicine area for monitoring body parts to determine changes in the tissue or organs. In manufacturing processes, this technology is often required for the quality control of CNC (Computer Numeric Control) produced parts. More recent renowned applications can be found in reverse engineering, robotics, archaeology, cinema, forensics, cartography, and other fields (FERNANDES, 2012) (REISS, 2007).

A definition for "3D model" is a geometric object representation in three-dimensional space, which provides a virtual (analytical/mathematical/digital) description of the shape and dimensions of the object using mathematical means. This representation can be based in entities as points, lines, circles, rectangles, and others. This description holds a set of advantages in comparison to the manipulation of the real object, since it is usually simpler and more practical to run experiments, perform measurements, and transmit results with the model. Besides that, the 3D reconstruction can be used to preserve the original object's structure if its physical properties are compromised, what is especially interesting for engineering's applications (FERNANDES, 2012) (REISS, 2007).
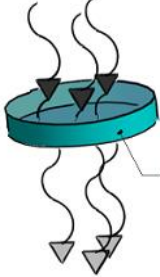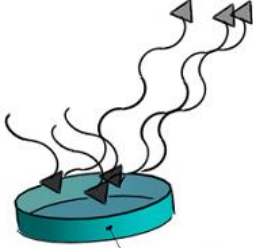
By contrast, surface imaging deals with measurement of the coordinates of points on an object's surface. Since these surfaces are generally nonplanar, it is described in a 3D space, and the imaging problem is, therefore, called 3D surface imaging. The result of the measurement may be regarded as a map of the depth as a function of the position of each point in the surface of the object in a Cartesian coordinate system (GENG, 2011). This set of dense surface data points that are presented along a 3D coordinate system is usually called point cloud. This cloud, after image processing treatments, is consolidated in the object's 3D model. This process is also referred to as 3D surface measurement, range finding, range sensing, depth mapping and surface digitalization.

When 3D information of a given surface is needed, it is necessary to choose between a passive and an active method. The term "active" refers to the methods that need of a secondary light projection source, while the "passive" ones utilize only ambient light (FERNANDES, 2012). Specifically, the active optical methods for dense measurements of object surfaces employ one or multiple light source and one or multiple cameras for shape acquisition.

Generally, the 3D scanners are equipment with the ability to generate 3D models of real objects. There are different scanning systems used for capturing different sized objects (i.e. from a small tool to a large building), with a wide range of scales (i.e. from few mm up to tens of hundreds of meters), and so can be divided into different scanning systems according to range.

The contactless scanners in two different groups, transmissive or reflective, described in Table 2.7 (CURLESS, 1997).

Table 2. 7: Contactless scanners groups (CURLESS, 1997).

Group	Principle	Main technologies
Transmissive	Emission and detection of ionizing radiation.	Computerized Tomography (CT-Scan)
Reflective	Optical (passive sensors)	Stereoscopy
	Optical (active sensors)	Time-of-flight Laser scanners Structured Light
	Non-Optical	Microwave radar Sonar

Only the topics related to active non-contact measurement techniques by reflection will be detailed discussed, due to their greater potential solution for automated surface inspection system.

1.2.1 3D laser scanners

The use of triangulation methods has started 5000 years with the Babylonian technology. After, Euklid have set the trigonometry in the occident about 2500 years ago, and, with the consolidations of the scientific methodology, the laws of optical triangulation have been enlightened by Snell van Rojen in the 17th century. However, 3D scanners based in this principle with practical applications and able to record 3D images with satisfactory resolution have been realized only about 30 years ago (BREUCKMANN, 2014).

There are several reasons to replace conventional contact measuring methods, such as CMMs, micrometers or stylus profilometers, by new approaches. Often contact methods are not applicable due to the fragile nature of the subject, the surface sensitivity to mechanical contact, the wear resistance of the equipment, very high or very low object surface temperature, very small object size, or the time limitation of measurement (GIESKO, 2007).

The automatic laser scanning has revolutionized 3D data acquisition. In contrast to the "classical" manual data acquisition techniques, like terrestrial surveying and analytical photogrammetry, which require a manual interpretation to derive a representation of the sensed objects, these new automatic recording methods allow an automated dense sampling of the object surface within a short time.

There are many different types of laser scanners on the market and they have different specifications for different applications. However, the specifications of different scanners are designed with different scanning principles. Almost all these scanners are designed according to three different scanning principles: 1) Pulse-based; 2) Phase based; and 3) Triangulation-based. The most accurate and robust close-range scanners are designed with triangulation-based techniques. These are the equipment applied to profilometry techniques, which are the application of interest in this work.

Machine vision systems based on 3D triangulation are employed in a range of industries from automotive and electronics manufacturing to lumber mills. While the basic concept of measurement using triangulation is simple, there are several important details that must be addressed when implementing such systems. These include how laser-based 3D triangulation systems are configured and how laser line (LL) parameters are specified (LATIMER, 2015).

In the last decade, 3D laser scanners have been widely used for quality inspection, surface profile measurement, and reverse engineering applications. These systems use a camera and a laser light to model 3D objects as the appearance of the laser spot changes according to the distance between the light source and the object surface (MARANI, ROSELLI, *et al*., 2013).

The active triangulation laser scanners are based on a light beam generation, where either a single point scanner or a line is projected on the surface. The highlighted surface with irregularities is captured with a camera, which is placed at a special distance and angle, such that it permits an optimal profile of the highlighted features (MONTILLA, ORJUELA, *et al.*, 2014). The Figure 2.9 shows graphically the laser triangulation configuration, and an example of a commercial scanner. This method of scanning is restricted in depth, because the quality of the intersection decreases with range. The basis, i.e. the distance from the emitter to the camera, cannot be made too big for practical reasons. Therefore, this type of scanners is restricted to ranges from millimetres to few meters (PFEIFER, BRIESE, 2007). Usually, the compact laser sensors are characterized by the resolution given in the micrometer scale and for short

ranges, laser triangulation sensors are capable to provide sub-micron resolution (GIESKO, 2007).
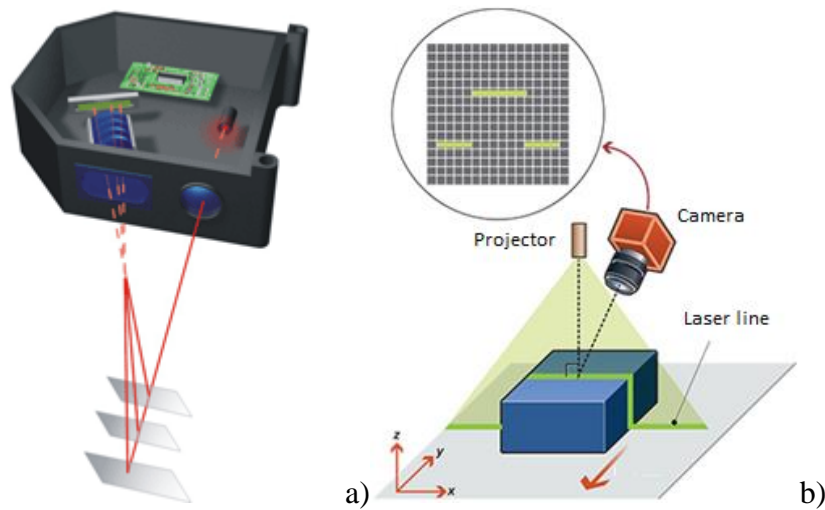
Figure 2. 9: Schematic representation of the laser triangulation Operation for a) single point and b) line beams. Adapted from (LATIMER, 2015).

Some of the main advantages of this equipment in comparison to other kind of optical scanners are the easy implementation, high 3D accuracy, repeatability rate and insensitivity to light environment (SANSONI, TREBESCHI *et al*., 2009).

However, there are also limitations to the method caused by the nature of vision sensing which can influence the measurement results. The particularly significant effects are surface reflection, a different contrasting surface texture in the microscale, a shadow effect, laser beam disturbances at the edges of the object, light diffusion and absorption (GIESKO, 2007). In addition, there are safety constraints associated with the use of laser sources. Furthermore, to scan an entire surface, the laser triangulation equipment requires that a motor translates or rotates a part of the scanner so that the laser plane is swept across the surface (TÖRNBLOM, 2010).

The laser triangulation principle is based on viewing angles measurement of a laser beam spot projected onto the object surface. The light quantity distribution of the reflected beam from the object is analyzed and the sensor detects the pixel with the laser light peak value. The position of the laser spot on the sensor is related to the position of laser beam on the object surface, as can be seen in Figure 2.10 (right). When object is

moved from position 1' towards 2', the laser beam displacement on the sensor is equal ds (GIESKO, 2007).

a)

b)
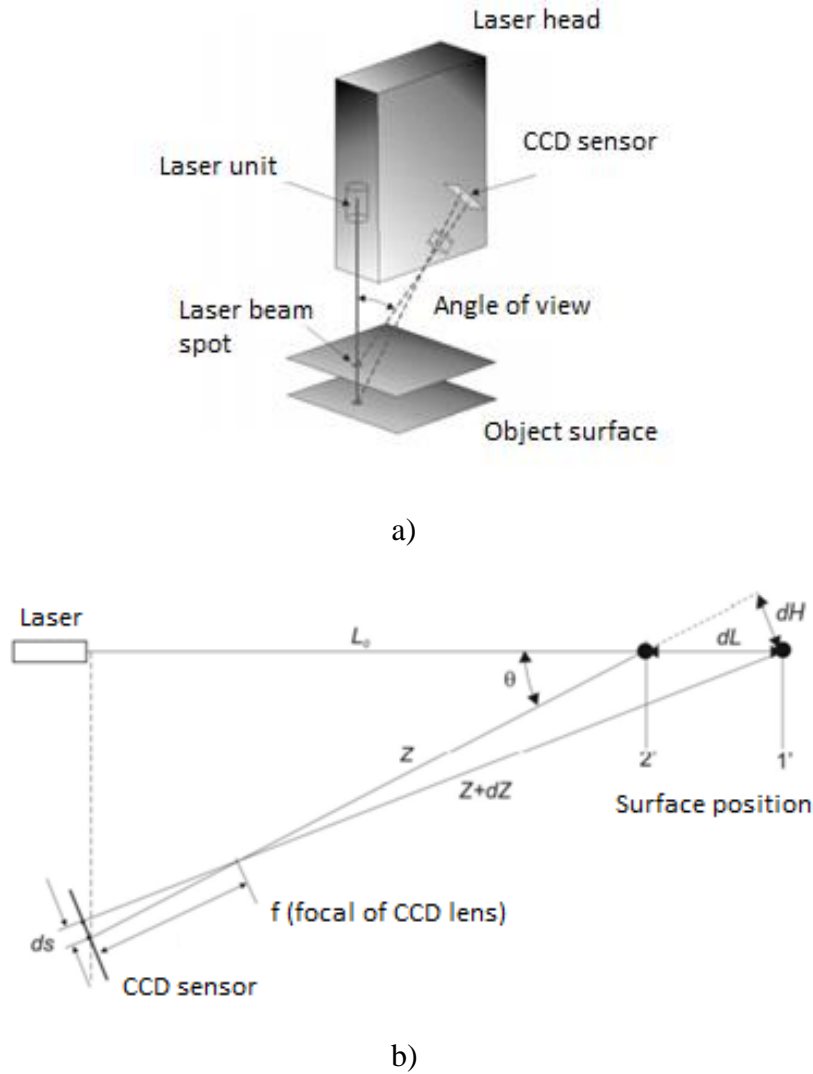
Figure 2. 10: Illustrations of the laser triangulation principle. a) the main parts of a profilometer head. b) schematic illustration of the triangulation process (GIESKO, 2007).

According to Giesko (2007) the measurement sensitivity is expressed as a function of the triangulation angle Θ, the base distance Z and the focal distance f according to Equation 2.8:

$$\frac{ds}{dZ} = \frac{f}{Z} sin\Theta$$

Equation 2. 8

For the 3D reconstruction of the inspected surface, two-dimensional matrix W is created from the recorded data as the digital point cloud of the scanned surface. The data set is expressed for Equation 2.9:

$$W = \sum_{i=1}^{n}\left(\sum_{j=1}^{m} L_{ij}\right)$$
Equation 2. 9

where: i, j are row and column number, respectively and L_{ij} is the signal value at (i, j) point of scanned area.

In general, the hardware required to implement this measurement technique includes (MALCOMB, 2014):

- The profilometer head (the scanner itself) which houses the laser and detector;
- A mechanism that moves the object or camera/laser system through the field of view of the imaging system, with a controlling system;
- A PC application to process the captured image and accurately translate pixel offsets to height differences.

Although very different systems are possible to be projected using these basic elements, more general and versatile equipment have been created in the last years. For example, Giesko and al. (2007) developed a very representative surface profilometer X-Y (with a vertical range of 10 mm, scanning area of 100 x 100 mm², resolution of 1 μm and scanning step of 0.6 μm / 5 μm) and a rotational profilometer R for small objects (with radial measurement range of 80 mm, vertical radial measurement range of 100 mm, resolution of 0.5 μm, vertical scanning step of 0.6 μm / 0.5 μm and angular scanning step of 0.003° / 0.027°), equipped with high accuracy laser heads, as can be seen in Figure 2.11. The adjustment of the working distance of the laser head is possible by using a manually operated micrometer head. In the rotary profilometer R, the rotary stage was applied for angle positioning the object towards the laser head.
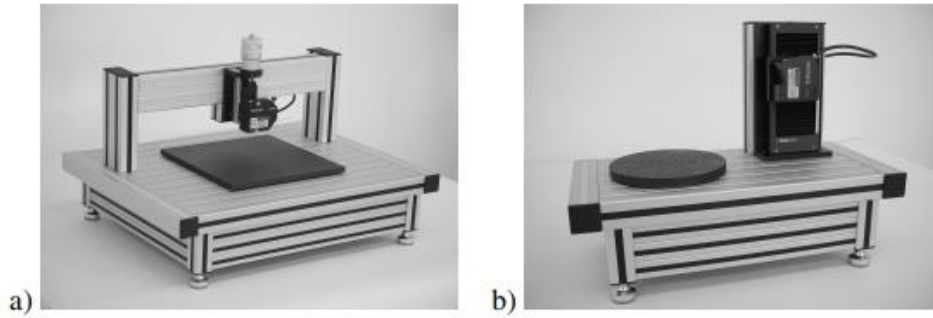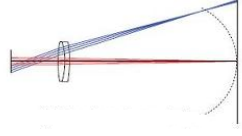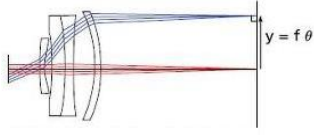
Figure 2. 11: Example of developed profilometry systems: a) profilometer X-Y; b) profilometer R; Adapted from (GIESKO, 2007).

The laser is driven across the entire countersink along a specific axis at a specified feed rate using the CNC. The position of the edge on another perpendicular axis is sampled at a specified frequency using a standalone laser controller. For each sample, the position is inferred from the feed rate and sampling frequency. Usually, to scan the straight direction of a laser beam and focus it to some plane or along a line for 1D scanning, rotating or galvanometer mirrors in conjunction with scanning lens are applied. The lens is responsible for focus the beam and modifies its propagation direction. For this application, the lens cannot have a simple spherical geometry, since its focus positions cannot be in the plane of interest. To solve this problem, new kinds of lenses or, in fact, multi-elements lens systems, have been developed to overcome this limitation, each one of them with specific characteristics, as can be seen in Table 2.8. Therefore, the choice of the lens is an essential factor in the scanning system project (RP PHOTONICS, 2019).

Table 2. 8: Scanning lenses types. Figures adapted from (ENVISION, 2015).

Type	Characteristics	Illustration
Simple achromatic lenses	Focus position lie on an approximately spherical surface, out of the plane of interest. They are not suitable for scanning processes.	
Flat-field scanning lenses	Provide an approximately constant spot size throughout the target plane.	$y = f \tan \theta$
F-theta scanning lenses	The spot position depends linearly (with only weak aberrations) on the beam angle θ, what reduces the image distortion.	$y = f\theta$
Telecentric lenses	Obtains normal incidence for all points of the target plane, obtaining a quite precisely constant spot size or the full area, avoiding beam ovality. Scan area is limited by the size of the lens.	$y = f\theta$

The laser profilometry hardware is composed of a system that integrates the profilometry scanner, a moving mechanism with its controlling equipment, and a PC application for the data processing. Besides that, the choose of the scanner lenses type is a fundamental parameter that affects directly the scanning capability.

1.2.2 Structure light scanners

Some of the most widely used active methods in the field of vision based non-contact 3D measurements are based on structured light scanning (SLS). The functioning of structured light scanners is based in a projector shining structured patterns onto the object whose geometry distorts the structured patterns and a camera captures the distorted structured images from another perspective. The correspondence is established by analyzing the distortion of captured structured images with known features (e.g., phase interpolation) projected by the projector (ZHANG, 2018). Once the system is

calibrated and the correspondence is known, (x, y, z) coordinates can be reconstructed, using a method similar to the method used by stereo vision techniques, but replacing one of the two cameras by an active light projector, as can be seen schematically in Figure 2.12. A few alternative definitions of SLS are also found in literature (GENG, 2011). Inspections through the SLS will be used as reference inspection to the developments performed in this work.
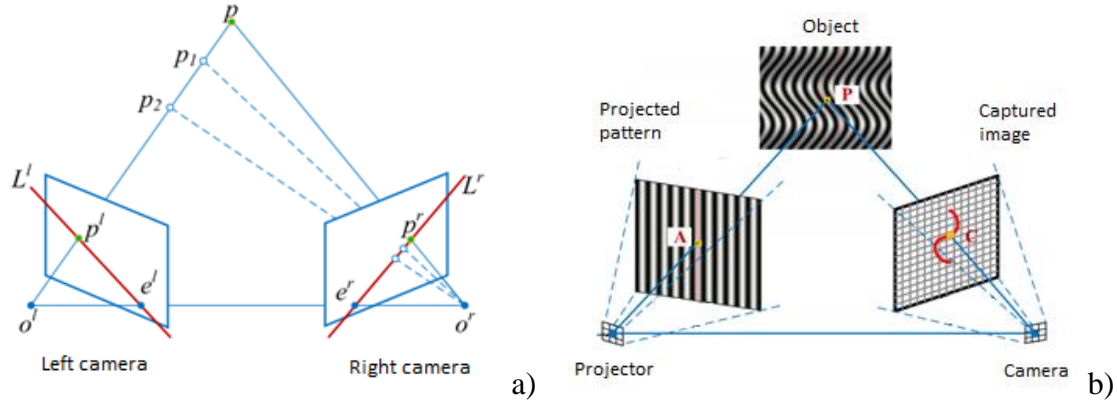
Figure 2. 12: a) Epipolar geometry for a standard stereo vision system; b) Schematic diagram of a typical structured light system. Adapted from (ZHANG, 2018).

The technique started to be used in early 1980's, whose invention can be attributed to Posdamer and Altschuler (ALTSCHULER, 1982). Some milestones related to the SLS development after this first consolidated system are: the invention of the Photon Mixer Device (PMD) for Time of Flight (TOF) imaging (SCHWARTE, 1997), the introduction of the Microsoft Kinect 1 single-shot structured light system, and, more recently, highly accuracy systems from manufacturers like GOM, Cognex, Hexagon Metrology, and Aicon 3D Systems (WILM, 2015). Figure 2.13 shows typical specifications of a modern high definition scanner and its specifications.

Specifications	smartSCAN^{3D} C5
Camera type	2 CCD colour cameras
Camera resolution	5 MPixel, each
FOV	30 to 1500 mm
Operating distance	250 to 1500 mm
Triangulation angle	(30°/20°/10°) within one
Acquisition time	ca. 1 sec (fast mode)
Sensor weight	ca. 4 kg
X/Y resolution	10 to 500 μm
Z resolution	1 to 50 μm

Figure 2. 13: Typical specifications of the high definition smartSCAN3D C5 scanner of Breuckmann GmbH, now Hexagon Metrology (table); the smartSCAN system of Breuckmann GmbH (image). Adapted from (BREUCKMANN, 2014).

In contrast to other active methods such as laser line scanning, structured light coding schemes have been developed which encode a scene with multiple thousands of scene points with as little as one static pattern. As an example, with binary coding the number of patterns and camera frames, N, is in the order of 10. In laser line scanning 2^N camera frames, which can be encoded, are needed for the same coverage (WILM, 2015). This also means that the scan time usually is usually longer with a laser scanner than with a SLS (TÖRNBLOM, 2010).

With this technique, a dense reconstruction of the surface can be obtained with as little as three projected patterns and camera images. This is, in contrast to laser line scanning, where each camera image yields only reconstruction of a single line of points on the object surface. However, as the triangulation principle is the same, a SLS scanner can be considered a parallelized laser scanner (WILM, 2015).

Due to the flexibility and versatility of structured light methods, 3D shape measurement using structured light methods has been a vibrant field with increased interest in development and employment. High-speed and high-accuracy 3D shape measurement techniques become more and more important with new applications found

regularly (ZHANG, 2018). The components comprising an SLS scanner are available as commodity hardware, therefore highly accurate systems can be constructed at comparatively low prices. In recent years, the general availability of highly accurate systems (down to single digit micron) has grown, from manufacturers like GOM, Cognex, Hexagon Metrology, and Aicon 3D Systems (WILM, 2015).

According to Reiss (REISS, 2007), the structured light systems are based on three main problems to be mastered: Pattern codification, system calibration and capture unit. These three problems will be explained and explored in the next subsection.

Pattern codification concerns to the correspondence ways between the structured light patterns projected over the image and its posterior decoding. In other words, to make possible to determine each structured light point between its neighbors and assign to them the geometrical parameters that would allow the point 3D reconstruction (REISS, 2007). This is a solution for one of the main problems experimented by 3D scanning: make a sparse reconstruction since density is directly related to the texture of the object. This complicates the process of finding correspondences in the presence of less texture surfaces. The projected pattern creates the illusion of texture onto an object, increasing the correspondences (SALVI, 2010).

The patterns can be coded spatially (in a single frame), temporally (in multiple frames), or in a hybrid combination of the two types of coding. Spatial coding consists of the projection of a single pattern for the acquisition of the object's structure, allowing its application in dynamic scenes. On the other hand, temporal coding consists of the projection of a sequence of patterns and benefits from redundancy, reducing reconstruction artifacts of the object's structure (FERNANDES, 2012).

Salvi et al. (2010) performed an exhaustively analysis of the different coding strategies used in active structured light, focusing on recent improvements. They classified the techniques considering firstly the discrete or continuous nature of the pattern, rather than the codification process. A posterior sub-classification is done regarding spatial, time and frequency multiplexing, and indicating some intrinsic attributes of each one. These attributes are specified in Table 2.9.

Table 2. 9: Coding attributes (SALVI, 2010).

Attribute	Description
Number of projected patterns (shots)	Whether the codifications can capture moving objects or not (1. 2 or >2).
Number of cameras	The method uses stereovision (two or more cameras) coupled to a non-calibrated pattern, or a unique camera coupled to a calibrated projector.
Axis codification	Number of coded axes (1 or 2).
Pixel depth	Color and luminance level of the projected pattern (B, G and C stands for binary, grayscale and color, respectively).
Sub-pixel accuracy	Presence of sub-pixel precision for the features, thus providing better reconstruction results (yes or no).
Color	Determines whether the technique can cope with colored objects (yes or no).

The sub-classification can be found in Tables 2.10 and 2.11. All the references presented in these tables can be found in the work performed for (SALVI, 2010).

Table 2. 10: Continuous coding strategies – Part 1. Adapted from (SALVI, 2010).
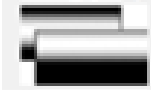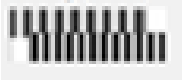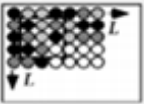
Techniques	Author	Year	Shots	Cameras	Axis	Pixel depth	Subpixel acc.	Color
Single phase shifting (SPS)	Srinivasan	1985	>2	1	1	G	Y	Y
	Ono	2004	>2	1	1	G	Y	Y
	Wust	1991	1	1	1	C	Y	N
	Guan	2004	1	1	1	G	Y	Y
Multiple phase shifting (MPS)	Gushov	1991	>2	1	1	G	Y	Y
	Pribanic	2009	>2	1	1	G	Y	Y
Frequency multiplexing single coding frequency	Takeda	1983	1	1	1	G	Y	Y
	Cobelli	2009	1	1	2	G	Y	Y
	Su	1990	2	1	2	G	Y	Y
	Hu	2009	2	2	2	C	Y	Y
	Chen	2007	1	1	2	C	Y	N
	Yue	2006	1	1	2	G	Y	Y
	Chen	2005	2	1	2	G	Y	Y
	Berryman	2008	1	1	2	G	Y	Y
	Gdeisat	2006	1	1	2	G	Y	Y
	Zhang	2008	1	1	1	G	Y	Y
	Lin	1995	2	1	1	G	Y	Y
	Huang	2005	>2	1	1	G	Y	Y
	Jia	2007	2	1	1	G	Y	Y
	Wu	2006	1	1	1	G	Y	Y
Spatial multiplexing grading	Carrihill	1985	1	1	1	G	Y	N
	Tajima	1990	1	1	1	C	Y	N

Table 2. 11: Discrete coding strategies – Part 2. Adapted from (SALVI, 2010).

Technique	Author	Year	Shots	Camera	Axis	Pixel depth	Subpixel acc.	Color
De Brujin	Boyer	1987	1	1	1	C	Y	N
	Salvi	1998	1	1	1	C	Y	Y
	Monks	1992	1	1	1	C	Y	N
	Pages	2004	1	1	1	C	Y	N
Non formal	Forster	2007	1	1	1	C	Y	N
	Fechteler	2008	1	1	1	C	Y	N
	Tehrani	2008	1	1	1	C	N	Y
	Maruyama	1993	1	1	2	B	N	Y
	Kawasy	2008	1	2	2	C	N	Y
	Ito	1995	1	1	2	G	N	Y
	Koninckx	2006	1	1	2	C	Y	Y
M-Array	Griffin	1992	1	1	2	C	Y	Y
	Morano	1998	1	1	2	C	Y	Y
	Pages	2006	1	1	2	C	Y	N
	Albitar	2007	1	1	2	B	N	Y
Binary codes	Posdamer	1982	>2	1	1	B	N	Y
	Ishii	2007	>2	1	1	B	N	N
	Sun	2006	>2	2	1	B	Y	Y
N-ary codes	Caspi	1998	>2	1	1	C	N	N
Shifting codes	Zhang	2002	>2	1	1	C	Y	N
	Sansoni	2000	>2	1	1	G	Y	Y
	Guhring	2001	>2	1	1	G	Y	Y

Therefore, it is observed that there is a large set of coding strategies in the commercial and academic sectors, with multiple possibilities of attibutes to be applied in different cenarios, depending on the characteristics of each utilization. For example, the chose of a specific coding pattern can make possible the reconstruction of dynamic surfaces, as in some scanners models of COGNEX company. Some strategies can also be highly efficient for measuring 3D objects with smooth surfaces, but not for ones with a great number of discontinuities, that is the case of MARUYAMA and WUST technique (SALVI, 2010). In conclusion, the choice of the coding strategy is a crucial point of the reconstruction process.

After the determination of the coding pattern to be applied in the reconstruction technique, the next fundamental topic in the SLS techniques is the calibration process.

In basic terms, the calibration seeks to determine the parameters of the indexed point projection geometry (REISS, 2007). The key to accurate reconstruction of the 3-D shape is the proper calibration of each element used in the structured light system. Several approaches to calibrating structured light systems can be found in the literature, such as techniques based on neural networks, bundle adjustment, or absolute phase, in which the calibration process depends on the available system parameter information and the system setup. It usually involves complicated and time-consuming procedures (ZHANG, HUANG, 2006).

To guarantee a maximum reconstruction accuracy that can be obtained with SLS systems is imperative to perform a precise and accurate calibration of three interconnected elements: the camera parameters, the projector parameters (that are called intrinsic parameters), and the parameters related to the spatial interrelationship between them both (that are called extrinsic parameters). Formally, both devices are often modelled by what are called linear projective pin-hole models, augmented with what is called non-linear lens distortion model. More information about these models can be found in the very representative investigation of, since their mathematical complexity escapes of the scope of this work (WILM, 2015).

This estimation of these parameters is made using coordinates in the scene space and its related coordinates in the image plane. To perform this, a test object calibration target is needed, with M number of known points target marks (LEGARDA-SAENZ; BOTHE *et al.*, 2004). Through the analysis of several views of this object, the estimation is carried out, positioned within the volume that is being imaged by the system. Therefore, the estimated parameters are expected to hold accurate only within the volume occupied by the test object.

A common target object is a plane with the test marks that are provided in an organized manner by the system manufacturer. This plane is positioned in several places of the 3-D volume, and for each one the calibration data are taken. The calibration data basically consists of an image of the test markers, and the absolute phase measurement of the target object. In the calibration process, first, the position of each target mark is estimated from the image taken. Once these positions are known, it is necessary to estimate the data used in the projector calibration. These data are estimated using the absolute phase measurement of the object, assigning each phase value to a unique

projector position. An example of measurement set can be seen in Figure 2.14 (LEGARDA-SAENZ, BOTHE *et al.*, 2004).

a)   b)   c)
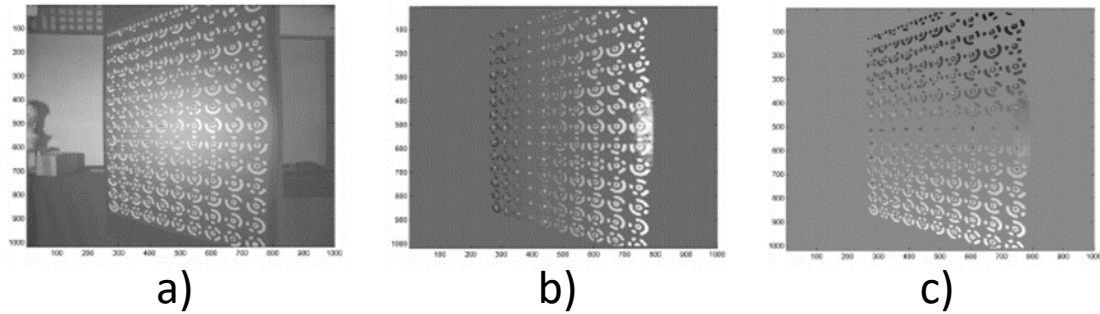
Figure 2. 14: Measurement set used in the calibration: a) simple image, and absolute phase measurements in the b) horizontal and c) vertical direction. Adapted from (LEGARDA-SAENZ, BOTHE *et al.*, 2004).

Once the input data are estimated, it is necessary to estimate the calibration parameters themselves. This can be made by minimizing the total square error between the measurements and the estimations of the coordinate's transformation (LEGARDA-SAENZ, BOTHE *et al.*, 2004).

After intrinsic parameters of the camera and the projector are calibrated, the next task is to calibrate the extrinsic parameters of the system. They are, for example, the image system orientation and the perspective center positioning (VILELA, 2008). These parameters determine the transformation that relates the position and orientation of the camera coordinate system to the position and orientation of the projector coordinate system and are intrinsically related to the relative position and orientation between camera and projector. Therefore, if the camera/projector positioning is altered after the calibration, it is necessary to calibrate the extrinsic parameters again before a new acquisition (FERNANDES, 2012). This estimation is accurate only inside the volume determined by the test object. With the 3D scanner set and calibrated, it is possible to proceed to the point acquisition using capture units.

The capture unit refers to the structured light projection and imaging physical tools. The structured light systems are capable of capture only one surface for each point of view, turning necessary to combine several points of view to create a complete 3D model of an object, if it is needed. Therefore, as presented before, in general the systems consist of a camera (or a set of cameras), a projector and, in some cases, a

support mechanism to move the object (FERNANDES, 2012). However, if the application of interest only requires the reconstruction of a specific surface of the scanned object, its movement is not necessary. In the Figure 2.15 is presented a complete SLS system to fully reconstruct small objects using a rotative platform.

The montage of the SLS capture unit also includes a software development component, creating a set of algorithms for the control and calibration of the system. Some common functions implemented in the control software are tridimensional point acquisition, background estimation, background reset, camera intrinsic calibration, projector intrinsic calibration, and system extrinsic calibration. In order to improve the accuracy of SLS inspection, it is also possible to perform a procedure called photogrammetry. This process consists of acquiring reference images of the sample surface to be inspected with randomly placed reference points on the surface. These points will be converted into a cloud of reference points that can be used for SLS inspection. (FERNANDES, 2012).
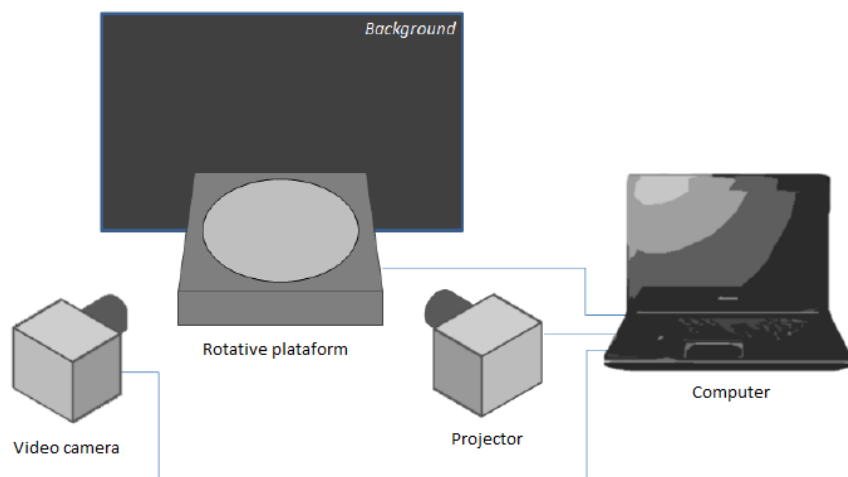
Figure 2. 15: Example structured light scanner. Adapted from (FERNANDES, 2012).

The capture of points is done by projecting and receiving a sequence of structured light patterns using a certain coded pattern and provides clouds of points to the output. The sequence of images captured by the camera is decoded to resolve matches between each pixel in the camera and each line or column of the projector. With the intrinsic and extrinsic parameters of the projector and camera, as well as the matches in hands, the 3D points are acquired by optical triangulation (FERNANDES, 2012).

Unlike laser systems whose light has some level of radiation, the SLS systems have no need for special safety precautions since it generally uses a white light source. In addition, some LCD systems have accuracies equivalent to those of the laser system. Another advantage of this system is the possibility of capturing all the projected targets and the image of the entire object at one time, turning unnecessary to keep the object static for a long period of time while the scanner swipes along the desired area of scanning. Although, in SLS it would be still necessary to take multiple positions to fully cover an object when the desired area is larger than the sensor coverage field (KOKUBUM, TOMMASELLI *et al.*, 2005). Another advantage in comparison to their counterpart laser-based systems are more attractive costs. Although, the laser devices are, in general, more easily miniaturized, offer a higher power illumination, and be equipped with optical filters to improve detection and image extraction. After the point clouds acquisition, the data must be processed and applied as an input for the surface reconstruction algorithms (FERNANDES, 2012).

The reconstruction of surfaces from the cloud of points obtained by a 3D scanner is complex issue. Although there are different methods to originate polygonal models from the point sets, there is a set of common steps to the various approaches, consisting of (FERNANDES, 2012):

- Alignment of the point clouds according to a common coordinate system: When the position and orientation of the object in front of the scanner are controlled, it is possible to determine a transformation that relates the different positions and orientations of the object. Hence, the point clouds will be related by the same transformation, which can be applied to relate the clouds. When this transformation is not determined, it is needed to use algorithms that estimate a transformation that align the different point clouds.

- Integration of point clouds into a single global cloud: Since each cloud of points contains a small area of the surface of the object, in order to produce a reconstruction of its surface, it is necessary to integrate the points of the different clouds. When the point clouds are related in pairs, a reference cloud is fixed. The point clouds are aligned with the reference, which takes its points at the end of each correlation.

- Construction of the surfaces polygonal geometric model: The reconstruction of a polygonal model that represents a surface is an explored subject. For that, there

is no standard method. The reconstruction can be done from sets of disarranged points, or from structured data (such as an image or a structured grid).

The main elements necessary to construct a SLS system explored in the last sections have multiple possibilities of customization and integration to best adapt the potentials of this technology. As observed, the reconstruction algorithms are based in a very basic set of steps but can be further improved and receive very different mathematical approaches to reduce errors associated to each scanning challenges.

1.3 Defect recognition and data processing

In the quality assurance field, inspection systems have been developed and are being more and more used in the manufacturing process for the defects detection. Several inspection techniques including optical, magnetic and acoustic non-destructive tests have been increasingly applied to this objective, using different physical principles and approaches to identify the presence of defects and to reconstruct then through computational routes. However, generate data carrying information about the presence or absence of defects in materials is not the end of the process. The recognition and classification of these defects are necessary because multiple kinds of sources can cause them with different features impacting the products quality. Indeed, without knowing the features of the defects, it is very difficult to even find their sources in a complex manufacturing process (KANG, LEE *et al*., 2009).

In this sense, automatic defect classification (ADC) is a remaining problem in manufacturing process due to limits of quantification of defect features conventionally relying on human judgment based on its own experience (KANG, LEE *et al.*, 2009). Defect classification system based on machine learning techniques are very common, since they are trained on defects to learn to distinguish defect types. After learning, it can then be used to automatically classify new defects into the corresponding type of defect folders (CHO, LEE, 2013).

In this chapter, the most representative methods for processing and classification of the data generated by the inspection of defects are explored. Firstly, a section for the processing of raw data is exposed, explaining common algorithms applied to inspection data as normalization, interpolation, between others. Then, in the following subsection,

the classification routes for the processed data are studied, showing different feature extraction methods and classification strategies often applied to defect recognition.

1.3.1 Data processing

In few words, data processing is the conversion of raw data to meaningful information through a wide range of manual or automated operations. Data is technically processed to produce results that lead to a solution of a problem or improvement of an existing situation. Similar to a production process, it follows a cycle where inputs (raw data) are fed to a process (computer systems, software, etc.) to produce output (value information and insights). This process is fundamental to guarantee that the classification strategies will generate reliable results based in the information carried by the data.

In this section, relevant algorithms applied to the data processing for automatic defect recognition are explored, the normalization, the interpolation, the color mapping and the contouring.

For locally limited defect recognition the practical use of color mapping requires suitable contouring methods. For example, in places with high gradient, the human eyes naturally follow the lines that form with the same color, separating similarly colored areas into distinct regions.

When contouring data, the algorithms effectively construct the boundary between these regions. These boundaries correspond to contour lines (2D) or surfaces (3D) of constant scalar value. They are called isolines or isocontours (PASCUCCI, 2019).

Most algorithms for computing contours are known as marching methods. These methods work by inspecting each cell independently of any others (it marches through the cells) and applying the intermediate value theorem on the edges of each cell, by looking at the values at the nodes.

A very common 2D contouring algorithm is called "marching squares". Given a two-dimensional data set, each vertex will have a certain weight "W". The method consists of drawing lines connecting the edges of the squares of that data set, using a reference value "N", also known as "iso-value".

The lines are drawn as shown in Figure 2.16 (SCHROEDER; MARTIN; LORENSEN, 2006), called the "Lookup Table", which shows all possible ways to represent the lines that will be part of the contour. Black dots represent larger values and white dots represent smaller values than N. This value is usually based on the data

statistical distribution. The Figure 2.17 shows an example of a contour performed by this algorithm.
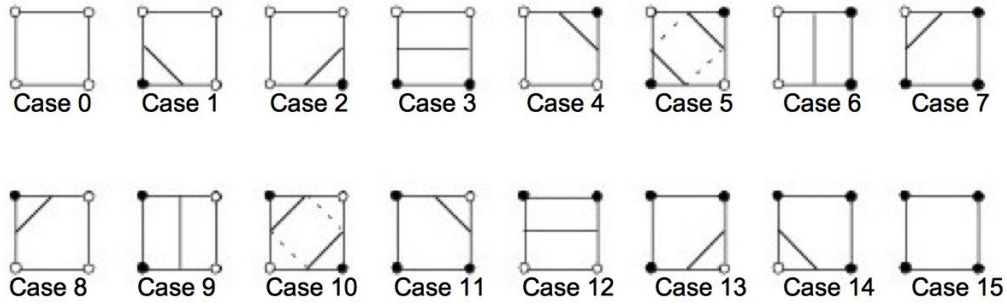
Figure 2. 16: Lookup table used in the Marching Squares algorithm (SCHROEDER, MARTIN *et al.*, 2006).
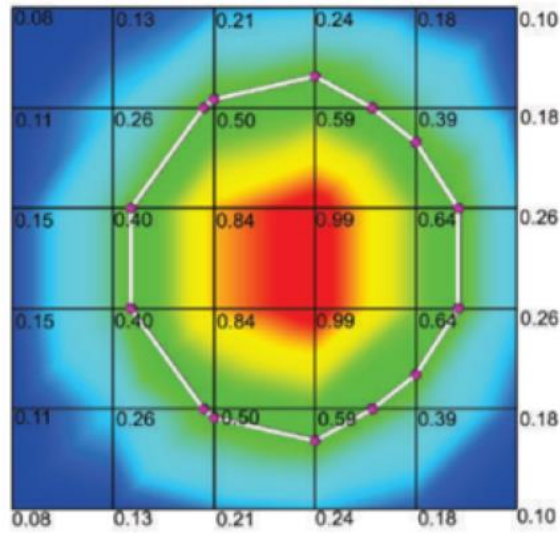
Figure 2. 17: Bidimensional values grid with N = 0.48 (SCHROEDER, MARTIN *et al*., 2006).

1.3.2 Defect recognition

This section will explore the classification methods of data after they pass through the processing stages shown in section 2.3.1.

All classification methods are divided in two parts. The first is called training, where a database of inspection results with already detected defects is utilized to determine specific parameters of a specific algorithm of classification. To make this possible, is necessary to reduce the information carried by each inspection result in a set

of features that can be interpreted by the classifier. The process of choose and determinate the features of each result is called feature extraction, which is crucial to the classification reliability. After the algorithm parameterization, that now receive the name "trained classifier", it become capable to be determined if a new inspection result has or has not a defect within. Some of these classifiers can also measure properties of the defect, what can be useful to analyze its severity. The Figure 2.18 (YIN, TIAN *et al*., 2008) resumes this classification route, using as an example inspection technique that generates image data.
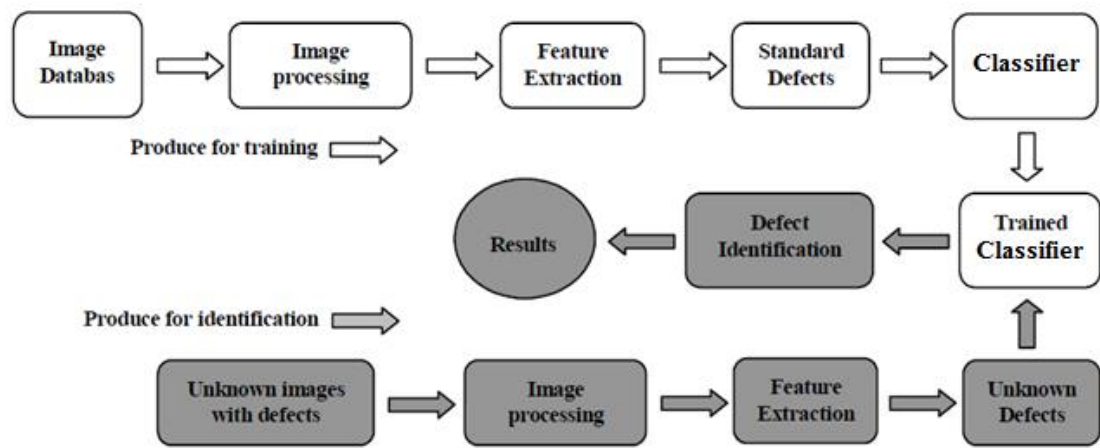
Figure 2. 18: Conventional automatic defect recognition route highlighting the classification stages. Adapted from (YIN, TIAN *et al*., 2008).

As exposed before, the feature extraction is a critical process to the whole defect recognition since, without it, the classifier will not be able to recognize from poorly selected features (KUMAR, BHATIA, 2014). Feature is synonymous of input attribute or variable, so, to find a satisfactory data representation is very domain specific and related to the available measurements of the case (GUYON, ELISSEEFF, 2006).

As stated by Lippman: "Features should contain information required to distinguish between classes, be insensitive to irrelevant variability in the input, and also be limited in number, to permit efficient computation of discriminant functions and to limit the amount of training data required". It is fundamental to focus on the feature extraction stage as it has a high impact on the efficiency of the recognition system.

Feature extraction quality of a feature extraction method is the single most important factor in achieving high recognition performance (KUMAR, BHATIA, 2014).

Although feature extraction main goal is to determine the most relevant and informative features, it can have other secondary objectives, including (GUYON, ELISSEEFF, 2006):

- **Reduce general data**, to limit the required storage and increase algorithm speed;
- **Reduce feature set** and save resources during utilization;
- **Accuracy performance** improvement;
- **Improve data understanding** and visualization;

Feature extraction is an important step in the construction of any pattern classification and aims at the extraction of the relevant information that characterizes each class. In this process relevant features are extracted from objects to form feature vectors. These feature vectors are then used by classifiers to recognize the input unit with target output unit. The features can be classified in (KUMAR, BHATIA, 2014) (PERNKOPF, 2004):

- **Statistical Features**: Derived from the statistical distribution of points;
- **Global Transformation and Series Expansion Features**: Derived to a series expansion of a continuous signal data. Examples are Discrete Cosine Transforms (DCT) and other wavelets transforms.
- **Singular value decomposition (SVD) features**: the first singular values directly derived from the range data of surface segments are used as features.
- **Geometrical and Topological Features**: These features may represent global and local properties of characters and have high tolerances to distortions and style variations. These are the main features to be considered in image data.

Human expertise is often required to convert "raw" data into a set of useful features, through the manual selection of the desired data to be used as features (KUMAR, BHATIA, 2014). This selection must, therefore, deeply consider the experimental methodology through which the data is generated.

In this subsection, strategies for automatic defect classification using NDT are explored, with examples of works that proposed recognition systems based on them. The common strategies are based on decision trees, neural networks, support vector machines, Bayesian networks and fuzzy logic.

Decision trees: Decision trees are considered to be one of the traditional and simple methods for representing classifiers, once they have a similar architecture as human decision-making (SONG; KIM *et al.*, 2018). A decision tree is a classifier expressed as a recursive partition of the instance space, composed of several nodes.

The algorithm begins with a 'root' node consisting of all the samples extracted feature vectors in the training dataset. After, they are recursively partitioned (or split) based on some splitting criterion into 'purer' subsets, also called branch nodes, till all the samples in the partition belong to the same class or a termination criterion is satisfied (SUMESH *et al.*, 2018). This classification is based on a specific value of the descriptor of each node. The nodes which cannot be further split are called leaf nodes (SONG, KIM *et al.*, 2018).

In a decision tree, the final node, where the input data arrive after passing every node, is called the terminal node, and the data are ultimately classified using the value of the terminal node (SUMESH, NAIR *et al.*, 2018). When applied to defect classification, each terminal node would hold a different defect type (CHO, LEE, 2013). The Figure 2.19 (BRID, 2019) illustrates a decision tree algorithm.
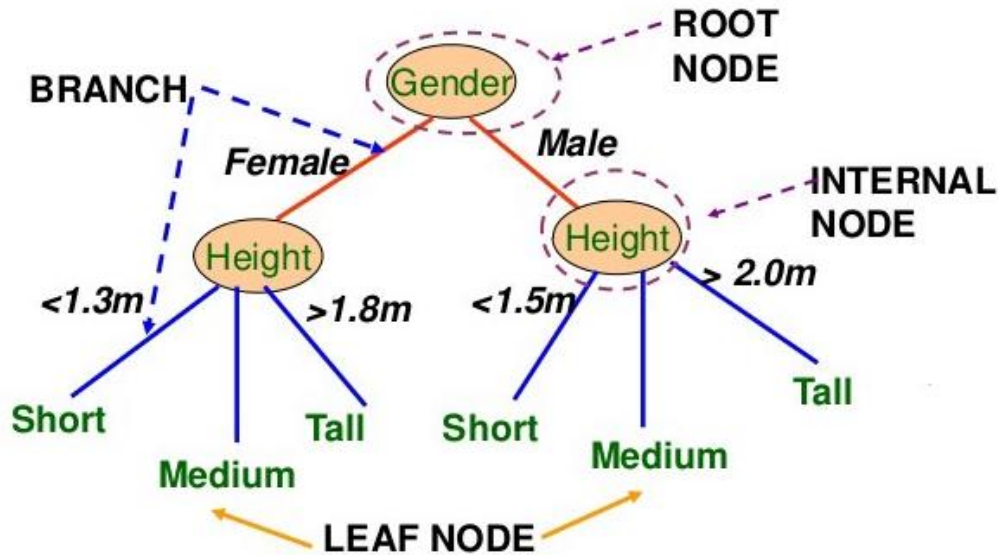
Figure 2. 19: Illustration of a decision tree algorithm. Adapted from (BRID, 2019).

Neural Networks: A neural network is a set of connected input/output units in which each connection has a weight associated with it. The network needs long training time in general and requires several empirical parameters. Between these, one of the most important is the network topology, which determines how the network connects the predictors to the targets through the hidden layers (CHO, LEE, 2013).

Between the different neural network methods, the multi-layer perceptron (MLP) shows several advantages. It is characterized by one or more hidden layers between the conventional input and output layers. This classification algorithm overcomes the limit of a single-layer perceptron, which enables only linear classification through a hidden layer, and allows more complex relationships at the reasonable cost of the training and scoring time, as can be seen in Figure 2.20 (SONG, KIM *et al*, 2018) (CHO, LEE, 2013).
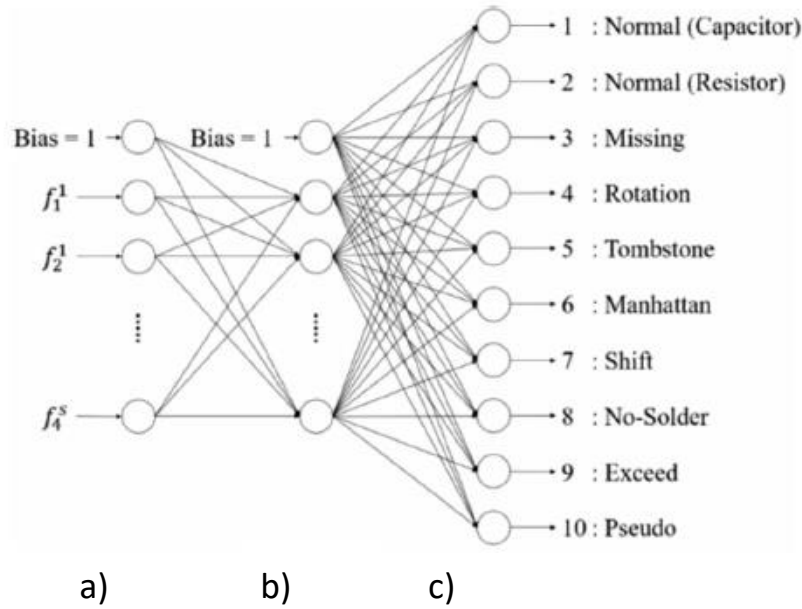
Figure 2. 20: Multi-layer perceptron algorithm structure, where a) is the input layer; b) is the hidden layer and c) is the output layer. Adapted from (SONG, KIM *et al*., 2018).

Support Vector Machine (SVM): SVM is a machine learning algorithm originally applied for binary classification problems and has risen as one of the most popular classifiers in various fields. The base of this method is the selection of a kernel function that maps the non-linear finite dimensional space including the input feature vectors in a much higher dimensional space. This is necessary because, in general, the dataset is linearly inseparable in its own dimension to be classified. Therefore, into a higher dimensional space, a linear classification is possible (SONG, KIM *et al*, 2018), as can be seen in Figure 2.21.
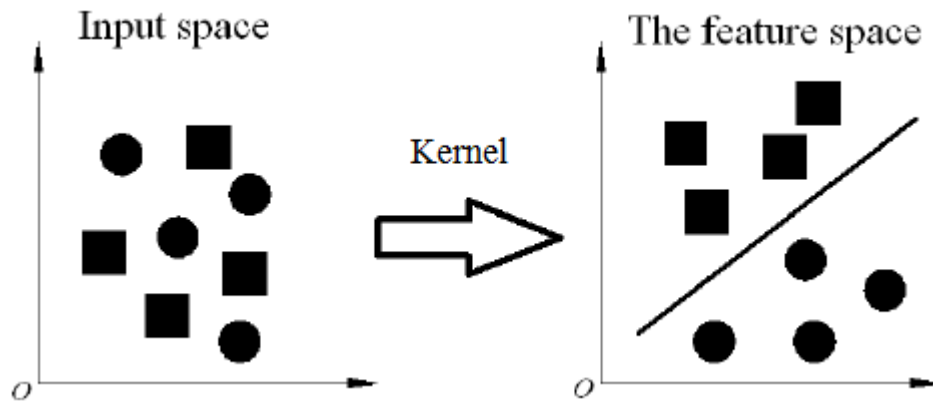
Figure 2. 21: Transformation of the input space in feature space through the application of the kernel function. Adapted from (WANG, GUO, 2014).

Then, a hyperplane is parameterized and moved between both classes until leaves the maximum possible margin, as can be seen in Figure 2.22 (WANG, GUO, 2014). Thus, the principle of this algorithm is to determine a hyperplane through a set of training samples (AMID, AGHDAM *et al*., 2012). In other words, it predicts which of possible classes forms the output from a set of input data, making it a non-probabilistic binary linear classifier. Furthermore, the SVM is recognized as a robust classifier that maximizes the predictive accuracy while minimizing over-fitting (CHO, LEE, 2013).
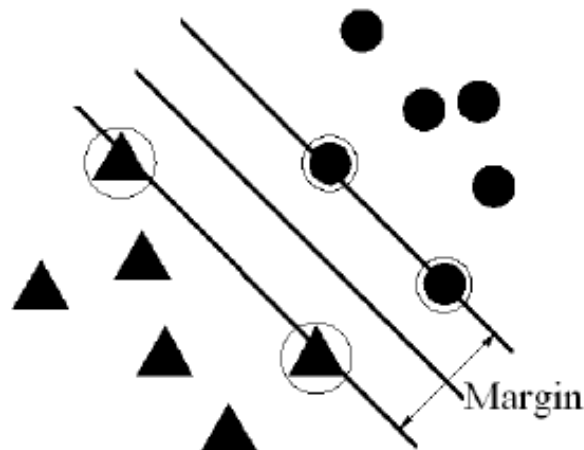
Figure 2. 22: Illustration of the optimal separating hyperplane of the "balls" and "triangles" classes. Adapted from (WANG, GUO, 2014).

Bayesian Networks: A Bayesian network is a statistical framework based on Bayes theorem (CHO, LEE, 2013). It is usually applied when is desired to achieve an improvement of the classification accuracy modeling statistical dependencies between attributes (PERNKOPF, 2004).

As exposed by Pernkopf (2004), a Bayesian network is a directed acyclic graph G, which defines probabilistic relationships among a set of random variables U, where each element in U has specific values denoted by $\{x_1. ..., x_n, x\}$. The symbol n expresses the number of attributes of the classifier. Each node of the graph expresses a random variable, while the edges denote the dependencies between these variables. The network models the conditional independence relationships so that each node is independent of its non-descendants, given its parents. These conditional relationships minimize the number of parameters necessary to express the probability distribution, as can be seen in Figure 2.23.
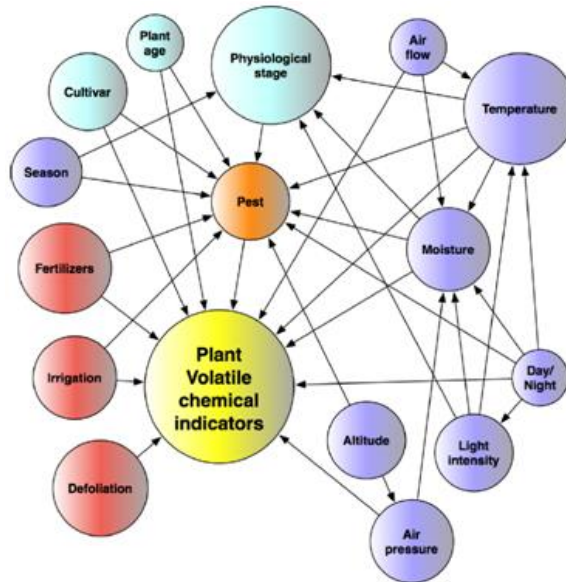
Figure 2. 23: Example of a Bayesian network. Adapted from (MIRESMAILLI, BADULESCU *et al*., 2007).

Therefore, the Bayesian networks are used for building classifiers based in this framework. The most common is known as Naïve Bayes Network (NBN). It is the simplest Bayesian network in terms of structure and learning. The NBN graph is restricted to a tree where the root can be expressed as a class variable C and the edges lead from the root to the remaining attributes. Therefore, the class node is the parent of

all attribute nodes in NBN, as can be shown in Figure 2.24 (GOUMEIDANE, BOUZAIENI *et al.*, 2015).
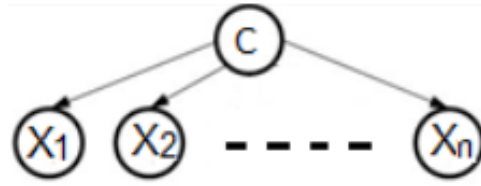
Figure 2. 24: Example of a Naïve-Bayes network. Adapted from (GOUMEIDANE, BOUZAIENI *et al.*, 2015).

The NBN is known to be a robust method that shows good performance in terms of classification accuracy, despite its simplicity. This includes the cases in which the independence hypothesis is violated (GOUMEIDANE, BOUZAIENI *et al.*, 2015).

Goumeidane et al. (2015), in a very representative work, applied Bayesian Networks to discriminate weld defects in radiographic images. They performed test on a database of few hundred elements, with very promising results, since they were capable of outperform powerful SVM conventional classifiers.

Fuzzy logic: Fuzzy logic (FL) is a simple and convenient approach for mapping a universe of discourse (another name for a input space) to an output space. In other words, mapping inputs to their corresponding outputs, such as in a general classification system where the inputs can be the feature vectors and outputs are the classification classes (AMZA, CICIC, 2015).

Theoretically, FL refers to all the theories and technologies that employ fuzzy sets, which are defined as classes with unsharp boundaries (ZAHRAN, AL-NUAIMY, 2004). The fuzzy set is the fundamental concept of FL. A fuzzy set is a set without a clearly defined boundary. In opposition to a classical set that wholly contains or wholly excludes any given element, a fuzzy set can contain elements partially, with a determined degree of membership. This degree of membership is also known as the membership function (MF), which defines how each point in the universe of discourse is mapped to a membership value (between 0 and 1) (AMZA, GHEORGHE *et al*., 2008), as can be seen in Figure 2.25 (AMZA, CICIC, 2015).
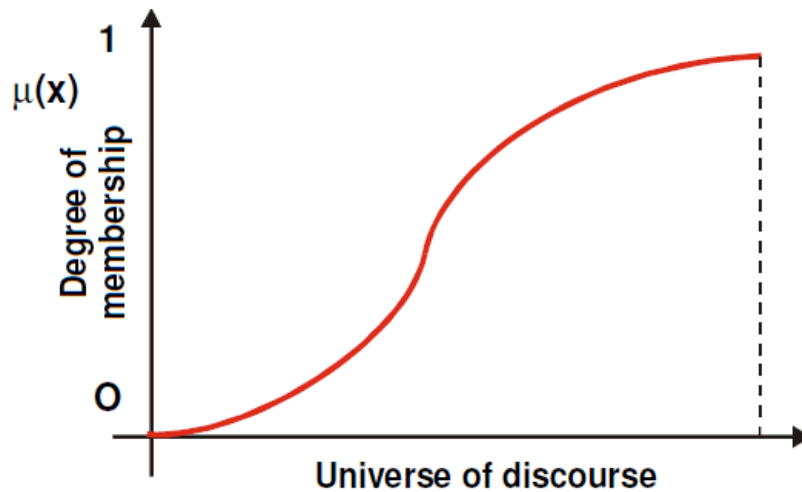
Figure 2. 25: Representation of a fuzzy set over a universe of discourse. Adapted from (AMZA, GHEORGHE *et al,* 2008).

Fuzzy logic can deal with situations in which is necessary to make a sharp distinction between the unsharp boundaries of applications. Therefore, it is largely applied for decision making and pattern recognition problems (ZAHRAN, AL-NUAIMY, 2004). Other advantages of FL are (AMZA, CICIC, 2015):

- high flexibility;
- high tolerance of imprecise data;
- can use experience of human experts as a scaffolding;
- It is based on natural language, which has evolved over the centuries to be convenient, easy and efficient. Consequently, it is possible to assume that FL can be easier to use than other methods such as NNs.

Despite the most diverse and sophisticated strategies for defect classification, the decisive point of the process occurs in the extraction of defect features. The feature extraction is a critical process to the whole defect recognition since, without it, the classifier will not be able to recognize from poorly selected features. It is fundamental to focus on the feature extraction stage as it has a high impact on the efficiency of the recognition system. In addition, as optimized as classification algorithms may be, they still require high computational power, which can be a problem for high-speed analysis.

The current work proposes to develop an algorithm that performs separately the extraction of defect characteristics with quality and reliability to be inserted in a secondary algorithm with the purpose of efficiently classifying the types of defects having good benefit in relation to the computational power required and the response speed of the analysis.

3. Bibliographic review

3.1. Electromagnetic techniques

The increasingly importance of non-destructive evaluation endorses basic and advanced research developments, driving a technological progress in this area of knowledge. In the last decades, some significant progress has been achieved not only in the technological development of more efficient sensors and probes, but also on the testing of new inspection techniques based on different physical principles.

Among these, a main technique has been placed in focus due to its technical relevance: EC test, where induced ECs are produced in the specimen under test and the resulting magnetic field is measured. Through the analysis of this measurement, the presence of defects and microstructural heterogeneities in the surface and subsurface of the specimen can be detected and reconstructed (GARCÍA, GIL *et al*., 2011). The relevance of EC test is, in part, related precisely to its high reliability and velocity in the detection of superficial and sub-superficial defects.

The EC test also allows the application of secondary solid-state sensors to measure its resulting magnetic field. This type of probe hybridization can provide a set of advantages to the inspection process and to the results. Not only that, but some of these sensors can be used apart of the EC test, with other inspection designs and principles, providing different information about the integrity of the tested specimen. One of the most used solid-state magnetic field sensors, often applied along with EC test, is the Hall Effect based sensors, usually called "Hall sensors" (CORREA, 2017). An overview of relevant publications about systems those integrate both EC and Hall sensors for pipe inspections are exposed and analyzed, showing how they can be associated in multiple and efficient ways.

Recently, the development of studies focusing on the optimization of EC test, mainly in the probes design, has been increasingly growing. Both the industry and the academy are making great efforts to not only increase the EC test efficiency and sensibility in its current applications, but also diversify its potentials. Several optimization techniques have been applied to improve the EC test probes performance. In this line of works, the publication of Chen and Miya (1998) proposed a new approach for optimal design of EC test probes based on simplified detectability analysis method and a ring current model. The optimal probe designs were developed comparing the

detectability of excitation and pickup coils combinations through the simplified analysis method. The high performance of the new probe designs is assured by the work results. Similarly, Karthik et al. (2015), studied the optimized coil positioning for a defect reconstruction in steel plates through a genetic algorithm. A finite element technique was applied to simulate the inspection for a moving and fixed coil, and experimental tests were performed to validate the simulations. In Figure 3.1, the numerical model and the optimum shape of the reconstructed defect can be seen.
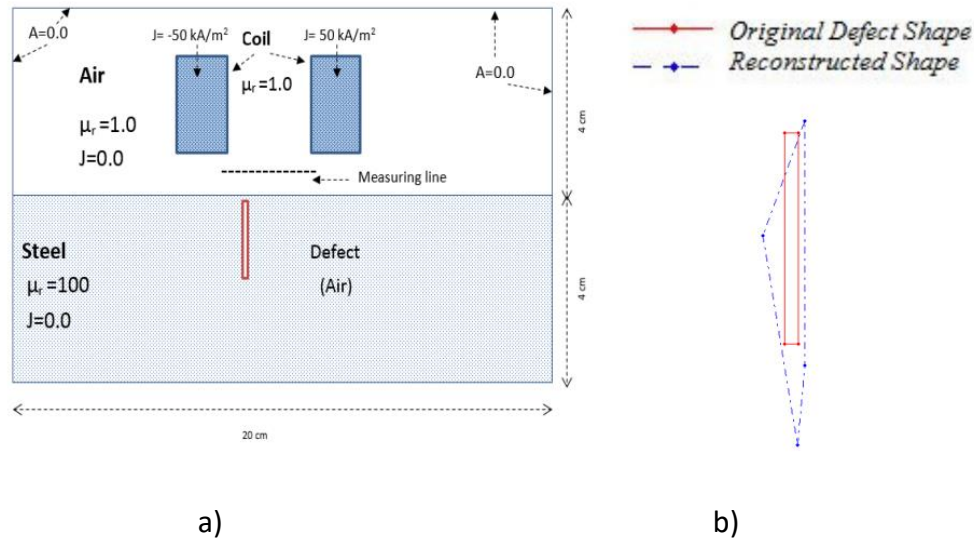
Figure 3. 1: a) numerical model; b) optimum shape of the reconstructed defect. Adapted from (KARTHIK MATHIALAKAN *et al.*, 2015).

In other important direction, applications with high relative movement between the probe and the test specimen have been a challenge that required new probes and systems designs. Between relevant publications focused in this goal, it is important to quote that Rocha et al. (ROCHA, RAMOS *et al.*, 2015) proposed an EC test probe design based on velocity-induced ECs to detect surface defects. Their results obtained through motion involved experimental tests confirmed that the proposed probe design was capable to detect the defects of interest. The design and optimization of the probe were performed using computational simulation. In the same goal, Pohl et al. (2004) have proposed the use of EC test for surface testing of railroad tracks at train speeds of 70 km/h. The results obtained in the high velocity tests were very promising, as can be seen in Figure 3.2.
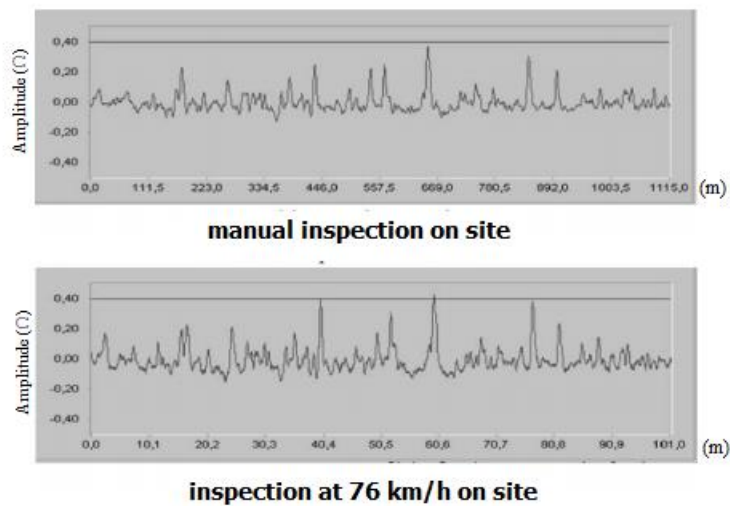
Figure 3. 2: Measured data of different scanning speeds where the vertical axis is amplitude and the horizontal axis is measured sampling. Adapted from (POHL, ERHARD *et al.*, 2004).

Also, an important field inside the EC test research that has been gaining high attention in the last years is the improvement of differential probes. The differential probes, in general, have superior sensitivity in comparison to absolute probes, what explains their popularity for many applications. For example, Chady et al. (1999) proposed a new EC differential sensor and a system for multi-frequency testing of conducting plates. The crack imaging was achieved using spectrograms obtained from an eddy-current probe multi-frequency response and application of a neural network. It is important to highlight from this work how the author solved the destructive interactions of frequencies. In order to solve the interference of the excitation signals, the sum of the harmonics was performed, obtaining an interference controlled by amplitude and phase in order to avoid the destructive interactions. Results of experiments showed very good sensitivity and spatial resolution. Some defects reconstructions can be seen in Figure 3.3.
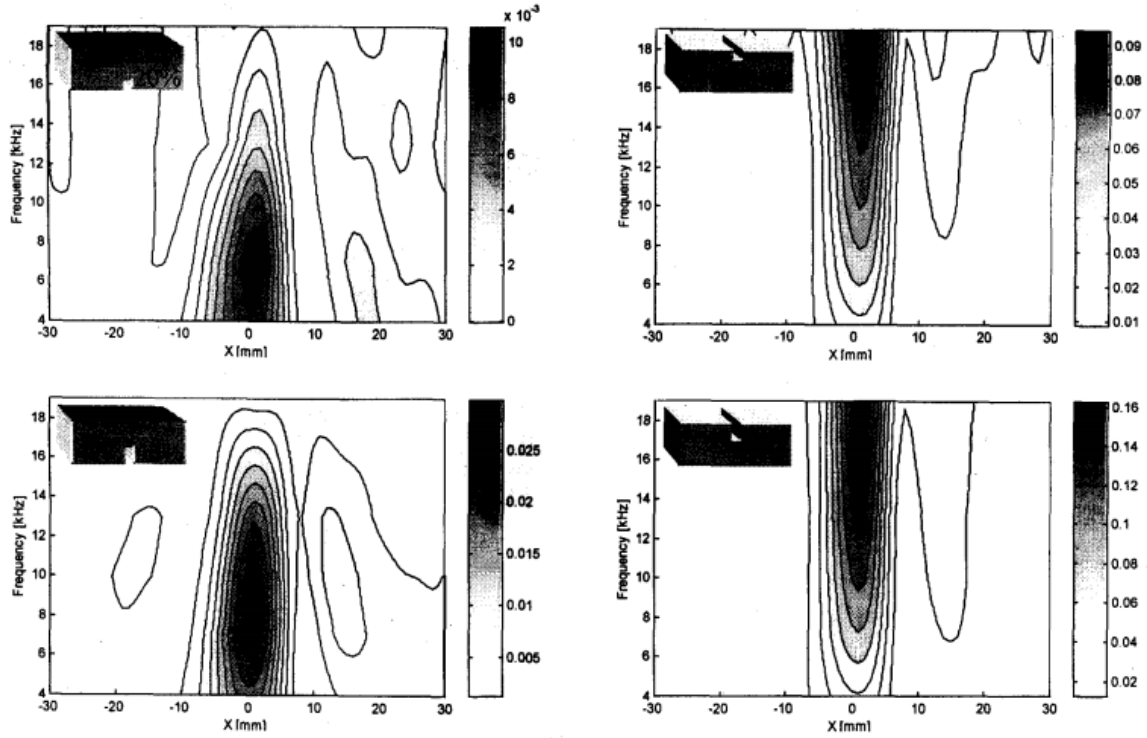
Figure 3. 3: Spectrograms showing the reconstruction of associated defects. Adapted from (CHADY, ENOKIZONO *et al.*, 1999).

In other work, Benhadda et al. (2014) performed a study of the influence of conductive defect characteristics on EC differential probe signal. The studied geometrical and physical parameters are the defect depth, width and electric conductivity, through a finite element simulation technique. This study brings into evidence the necessity to take into account the defect electrical conductivity so as to ensure a full and accurate defect characterization. Similarly, Slobodnk (2017) analyzed the detection capability of a differential probe using pulsed EC test over an artificial subsurface defect in an electrically conductive steel plate. The investigated EC consisted of one excitation and two sensing coils with a ferrite magnetic circuit. The numerical solution was carried out in the COMSOL Multiphysics using Magnetic field and Electrical circuit modules. The results were verified by performing laboratory experiment.

Several recent researches have been giving attention to the effects of the EC coils in the response signal and defects detectability. Pereira (2014) evaluated the best EC coil design for Ni superalloys inspection and determined that the sensitivity of a coil for inspection of a certain defect is directly linked to the shape of the EC field generated in

the part, being affected mainly by geometric factors, which can compete with itself. For example, compact fields are required for detection of small cracks, since they maximize the distortion caused by the discontinuity. On the other hand, satisfactory penetration requires the field to be large enough to permit enough penetration depth. Generally, it can be said that the depth reached by a simple coil is limited by a value equal to its diameter, while a satisfactory sensitivity requires that the diameter does not exceed the size of the defect to be detected.

Yang et al. (2018) used the ANSYS Maxwell software to construct a finite element simulation in order to demonstrate the influence of the EC sensor measuring coil geometry on the magnetic induction intensity of the coil, and on the linearity and sensitivity of the sensor. Finite element modeling (FEM) is a powerful tool for improving sensor design, that have been more and more applied in the development of electromagnetic sensors since the 1980s (YANG, FENG *et al.,* 2018), as will be further exposed in the next subsection. Some conclusions of Yang et al. (2018) shows that larger inner and outer diameter of the coil increases the sensor linearity and measurement range, but in the other hand decreases the magnetic induction strength of the coil, the magnetic induction intensity in the axial direction and the sensor sensitivity. Besides that, smaller coil thickness, increases the magnetic induction strength of the coil, magnetic induction intensity in the axial direction and sensor sensitivity, but in the other hand decreases sensor linearity and the measurement range.

In other study also applying simulation, Zhou et al. (2015) modeled different probes such as cylindrical differential probe, single orthogonal rectangular probe and biorthogonal rectangular probe using COMSOL Multiphysics software, as can be seen in Figure 3.4.

a)   b)   c)
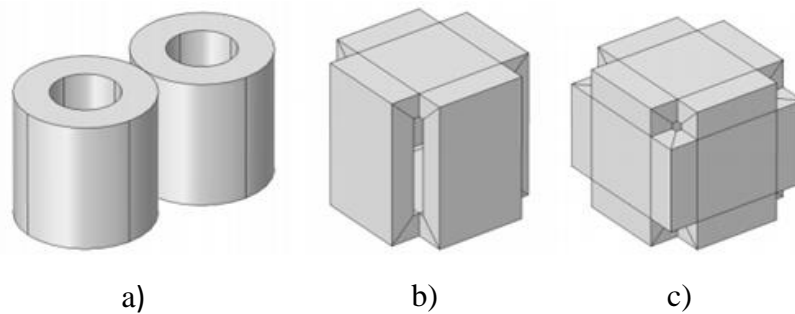
Figure 3. 4: a) Cylindrical differential probe; b) single orthogonal rectangular probe; c) biorthogonal rectangular probe. Adapted from (ZHOU, HOU *et al.*, 2015).

It is possible to say that the main conclusion of Zhou et al. (2015) shows cylindrical differential probe as having a good detection sensitivity, single orthogonal rectangular probe as having a high inhibition effect and a better detection sensitivity of depth variation than length and width variation and the biorthogonal rectangular probe as having high inhibition effect, better detection sensitivity of depth variation than length and width variation and more significant change of output signal and improved detection sensitivity. Therefore, the biorthogonal rectangular geometry showed the better overall performance for their application. That occurs because the results reveal that the orthogonal rectangular probe has a smaller magnetic line of force distribution range and a less magnetic energy loss compared with cylindrical difference probe. Compared with single orthogonal rectangular probe, biorthogonal rectangular probe has a more concentrated distribution of magnetic line of force, a larger change of magnetic energy, higher detection sensitivity and wider linearity range. Hence, the FE simulation results reveal that the biorthogonal rectangular probe is a new type of probe with higher testing performance.

In that sense, the different probe types and its geometries makes a legitim influence in the optimization of the results expected for a specific applications and environment.

Electromagnetic sensors prove to be an efficient solution for the inspection of defects in materials, in view of the results presented of its applications and latest developments. However, it is still necessary to develop EC sensors for a specific defect range and morphology and multiplexed scale in order not only to cover larger surfaces, but also to be able to have a sufficient data acquisition rate to meet the industrial conditions. In addition, this data must be processed automatically, enabling not only the development of an in-line inspection methodology, but also being able to use it on-line. In the following chapters this work demonstrates the work done to overcome these needs using separately EC sensors and hall effect sensors, generating data to be processed in the algorithm also developed in this work.

3.2. Optical 3D techniques

For pipeline scanning processes, the tubular geometry of the object of interest and the access to the desired surfaces are the main challenges. Some of the milestones of the laser profilometry application for pipelines inspection are listed below.

Zhuang et al (1998) developed a simple pipe inspection system using a CCD camera and circular laser projector. The imaging sensor captures the periphery of the whole circle and finds the defect by processing the shape. They also applied an artificial neural network to classify the defect. Ames and LaMorte (2012) developed an automated laser scanning tool for pipeline corrosion to measure the extent of corrosion and provide an accurate contour map of the external corrosion of the pipe. The software for the automated laser scanning tool distinguishes between normal pipe surface features, such as seam and girth welds, and determines the depth and severity of the corrosion. Summan et al (2017) developed a probe system consisting of a compact laser profiler, fisheye lens camera and inertial measurement unit. Using bespoke hardware and an image feature-based Structure from Motion algorithm, the system could generate a photorealistic, geometrically accurate 3D surface model of the pipe. The probe has 250 mm in length with a diameter of 45 mm and was designed to operate in pipes with diameter of 2 to 6 inches.

In general, surface inspections of tubular laser products have been developed over the years. However, there are still certain limitations regarding resolution and detection due to the surface finish of the inspected materials, such as problems due to reflection. In addition, the large volume of data generated by inspections is a challenge for the analysis and identification of defects during the production process.

The interior visual inspection of pipework is a critical inspection activity required to ensure the continued safe, reliable operation of the operation and thus avoid costly outages. Typically, for visual inspection systems, the video output from a manually deployed probe is viewed by an operator with the task of identifying and estimating the location of surface defects such as cracks, corrosion and pitting. However, it is very difficult to estimate the nature and spatial extent of defects from the often disorientating small field of view video of a relatively large structure. For that reason, more and more specific research in the development of solutions for these challenges are been made in the last decades.

Kuntze and Haffner (1998) developed of one of the first commercial multi-sensory pipe inspection systems that use the structured light as the lighting component. The KARO system consists of a mobile robot and surveillance station that integrates visual, ultrasonic and microwave back-scattering sensing subsystems. Pikas (2007) made an overview of how 3D structured light technology works (process time, error, analysis, impact on corrosion analysis) and how it is now being used as a new method

for gathering pipeline feature or corrosion defect measurements. Thielemann et al (2009) used structured light technology for 3D data acquisition based on gray codes and phase shifting to verify other sensing techniques, such as ultrasound, that are used for pipe inspection. Ng (2013) developed a 3D videoprobe measurement system based on structured light phase shifting coding to be used as a metrological tool for welding inspection, generating full 3D maps or point clouds of the inspected weld surface. Buranský and Eva compared between three methods (CenterMax CMM, ATOS TripleScan II SLS and Metrotom 1500 computerized tomography) for data acquisition to the output characteristics of steel drawing tubes. Outer and internal diameters, eccentricity and ovality were measured. They conclude that GOM TripleScan represents one of the most advanced SLS equipment in the current market.

Despite the various researches carried out and various products developed using optical techniques to detect cracks and corrosion, for example, on surfaces, it still takes time to process the data. Therefore, there is not yet a product on the market that inspects the surface, processes the data and has the result automatically, in-line and in realtime.

3.3. Defect recognition and data processing

Inspection systems have been developed and are being more and more used in the manufacturing process for the detection of defects. However, generate data carrying information about the presence or not of defects in materials is not the end of the process. The recognition and classification of these defects are necessary because of multiple kinds of sources can cause them with different features impacting in the products quality. Automatic defect classification is a remaining problem in manufacturing process due to limits of quantification of defect features conventionally relying on human judgment based on its own experience (KANG, LEE *et al*. 2009). Defect classification system based on machine learning techniques are very common, since they are trained on defects to learn to distinguish defect types. After learning, it can then be used to automatically classify new defects into the corresponding type of defect folders (CHO, LEE, 2013).

D'Angelo et al. (2015) utilized a shape geometric descriptor (SGD) method to measure a set of geometric features from the image generated by the impedance plane of EC. The features would after being used to train a defect classifier. Between the extracted geometric features, the selected features to compose the feature vector are:

59

Length (L), width (W) and orientation angle (α) of the shape defined by the inertia axis in the impedance plane, as can be seen in Figure 3.5.
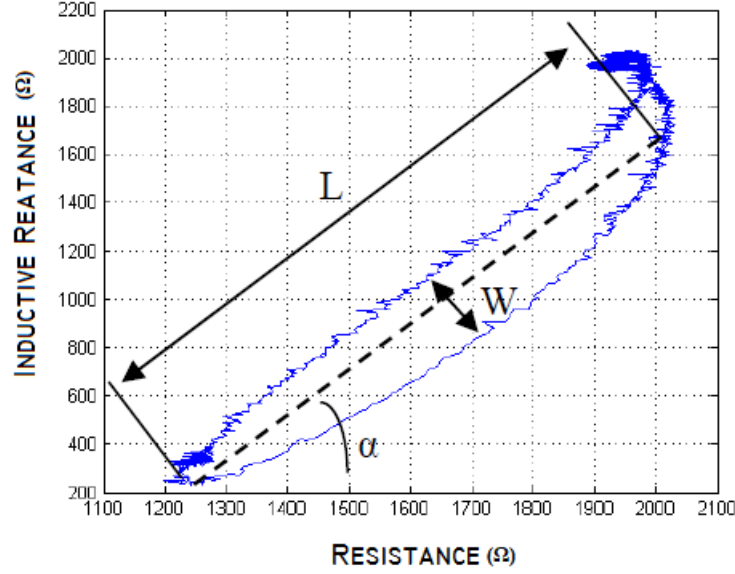
Figure 3. 5: Geometric features selected by D'Angelo et al. Adapted from (D'ANGELO, 2015).

In a similar work, Yin et al. (2019) proposed a clustering-based method in order to extract geometric features as length, width and inclination angle, taking advantage of the impedance data directly without using image recognition technique. The fundamental idea is to exploit clustering algorithms to find some centers of the data, as the K-means algorithm. They showed that considering a typical Lissajous curve (LC), after applying K-means clustering algorithm, three centers can be found, and the data are grouped into three clusters accordingly

Therefore, the length (d), width (w) and inclination angle (α) of each 'petal' of the impedance plane can be defined as shown in Figure 3.6 (YIN, YE *et al.*, 2019), and they are easy to compute. Additionally, symmetric indicator features $\frac{d_1}{d_2}$, $\frac{w_1}{w_2}$, and $\frac{\alpha_1}{\alpha_2}$ can also be calculated.
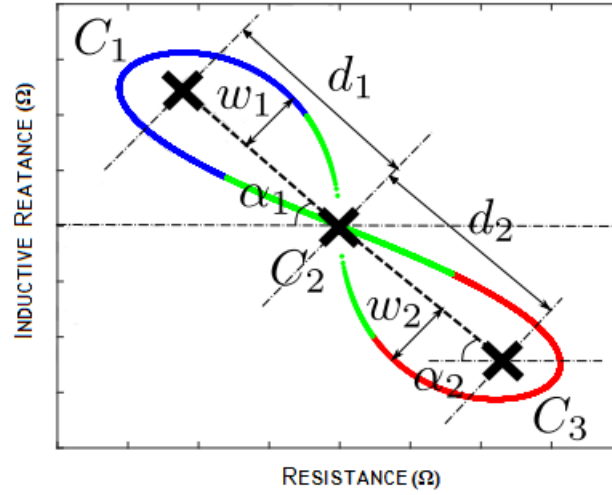
Figure 3. 6: Geometric features selected by Yin et al. Adapted from (YIN, YE *et al.*, 2019).

In other similar work, Cho et al. (2013) use five shape-based features: defect size, lengthiness, compactness, SDF(x), and SDF(y), where SDF(x) and SDF(y) are the standard deviations of coefficients in Fourier Transform domain with respect to x- and y- axis, respectively. The defect size is defined as the pixel count of a defect, and lengthiness is defined as the ratio of short line segment to long one in a compact rectangular region-of-interest (crROI). This region is defined as the bounding rectangle that tightly encloses an object and is obtained by rotating the coordinates such that the major axis parallels to the line that connects a pair of points at a longest distance on the contour of the object, as can be seen in Figure 3.7. Another feature, compactness, is defined as the ratio of the area of defect to that of a bounding circle (BC) that encloses the object.

Figure 3. 7: Defects with different geometries and their corresponding crROIs. Adapted from (CHO, LEE, 2013).

Furthermore, Yin et al. (2008) exposed many other geometrical features applied to defects classification of radiographic images. These features are useful to analyze the characteristics and severity of a defect once they are already detected. Some important of these features are resumed in Table 3.1.

Table 3. 1: Analyzed features by Yin et al. (2008).

Feature	Symbol	Description
Area	A	Actual number of pixels in the region.
ConvexArea	CA	The number of pixels in convex image of defect area.
Eccentricity	ECC	The eccentricity of the ellipse that has the same second-moments as the defect region.
EquivDiameter	ED	The diameter of a circle with the same area as the defect region.
MajorAxisLength	MajorAL	The length (in pixels) of the major axis of the ellipse that has the same normalized second central moments as the defect region.
MinorAxisLength	MinorAL	The length (in pixels) of the minor axis of the ellipse that has the same normalized second central moments as the defect region.
Orientation	Angle	The angle (in degrees) between the x-axis and the major axis of the ellipse that has the same second-moments as the defect region.
Perimeter	P	The perimeter of the defect area.
Solidity	SO	The proportion of the pixels in the convex hull that are also in the defect region.
Anisometry	Ani	Ani = MajorAL/MinorAL

However, the human expertise can be complemented by modeled feature extraction methods, that don't require a manual selection of the optimal features of data.

In some approaches, this modeled feature extraction is integrated with automatic feature construction methods. These techniques are capable to modify the original

vector with all the features to be shifted in a transformed vector that can facilitate the selection. Some of these methods are exposed by Guyon et al. (2006) as:

- Standardization;
- Normalization;
- Signal enhancement;
- Linear and non-linear space embedding methods;
- Non-linear expansions;
- Feature discretization.

Some of the most applied feature construction methods are dimensionality reduction algorithms as principal components analysis (PCA) or linear discriminant analysis (LOA). This is due to the fact that, generally, higher feature dimensionality has a more positive effect on classification performance, whereas it also has some negative effects such as an increased probability of exposure to noise. To avoid this, these methods are used to reduce the number of features to be inputted in the classification algorithms, choosing to be maintained the most relevant ones (KANG, LEE *et al*., 2009).

After the optional feature construction, several feature selection models can be utilized to determine the most satisfactory set of features. These automatic methods are usually best fitted for a specific classification algorithm. Guyon et al. (2006) resumed the most frequently used feature selection methods in Table 3.2.

Table 3. 2: Most frequently used feature selection. Adapted from (GUYON, ELISSEEFF, 2006).

Feature selection	Matching classifier	Comments
Pearson	Naïve-Bayes	Feature ranking filter. Linear univariate. Makes independence assumptions between features.
Relief	Nearest Neighbors	Feature ranking filter. Non-linear multivariate.
Gram-Schmidt	Linear RLSQ (regularized least squared)	Forward selection stopped at f features. Linear multivariate.
RFE-SVM (Recursive Feature Elimination)	SVM (Support Vector Machine)	Backward elimination. Multivariate, linear or non-linear.
OBD/ARD (Optimum Brain Damage / Automatic Relevance Determination)	Neural Networks	Backward elimination. Non-linear multivariate.
RF (Random Forest)	RF	Ensemble of t tree classifiers, each preforming forward selection. Non-linear multivariate.

After this extraction, the set of feature vectors of each sample (that, in this case, are images), acts as input for classification strategies. These strategies will be responsible to detect and, sometimes, characterize images with defects within. The most relevant classification algorithms related to the scope of this work will be further explored in the next subsection, along with its characteristics.

The work of Song et al. (2018) applied MLP neural nets to classify defects generated by surface-mount technology (SMT), which is used to mount components onto a PCB. The defect types to be classified can be seen in Figure 3.8. They applied a feature extraction region-based method to raise the capability of modeling-base methods to analyze the details of the defects and reduce the inspection time. The inspection procedure for the solder joint defect type classification consists of an offline stage, which sets the optimal feature extraction region, and an online stage which classifies a defect type.
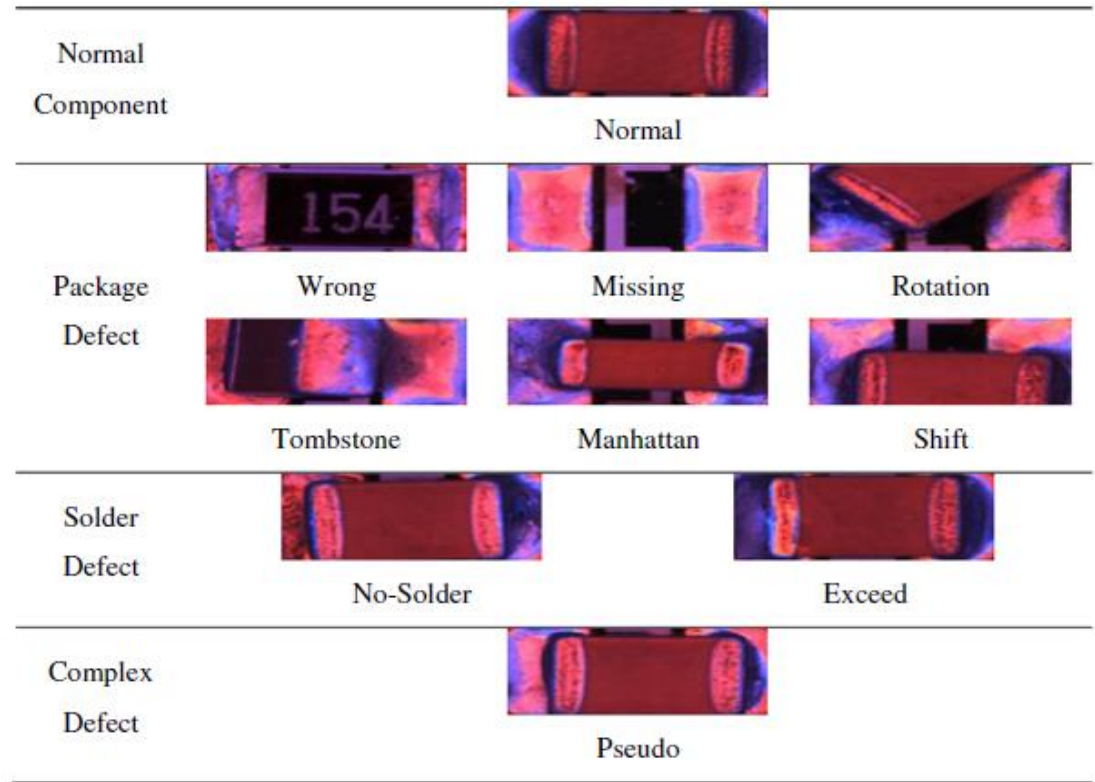
Figure 3. 8: Component image according to defect type. Adapted from (SONG, KIM *et al.*, 2018).

Between the possible kernels to be applied in the classification process, Amid et al. (2012) exposed some of the most relevant ones, for a feature vector x, as can be seen in Table 3.3.

Table 3. 3: Some of the most relevant SVM kernels (AMID *et al.*, 2012).

Name	Equation	Description
Linear kernel function	$\kappa_l(x, z) = x \cdot z$	Used for linearly separable feature space. It does not require any mapping over the dataset.
Quadratic kernel function	$\kappa_q(x, z) = x \cdot z(1 + x \cdot z)$	A simple and efficient kernel that became very popular in different applications.
Polynomial kernel function	$\kappa_q(x, z) = (\langle x, z \rangle + R)^d$	R and d are kernel parameters. It is intuitive to expect that the relative weighting of the higher order polynomial increases by decreasing R.
Radial Basis Function (RBF) or Gaussian kernel	$\kappa_q(x, z) = e^{\left(-\frac{\|x-z\|^2}{2\sigma^2}\right)}$	The parameter σ controls the flexibility of the kernel. Therefore, in other words, small σ increases the risk of overfitting while large σ transforms the kernel in a constant function which is not usable to learn any relevant classifiers.

When more than two classes are needed, it is necessary to apply a multi-class method, since the basic algorithm of SVM is binary, i.e., only accepts two possible classes in the output. This is necessary, for example, when the objective of the method is to classify more than two kinds of defects, as presented by Wang et al. (2014) in the classification of six typed of weld defects using X-ray images. In their work, they exposed the main multi-class methods that are: One against rest (OAR), One against one (OAO), Direct multi-class support vector machine (DMSVM) and Binary-tree method of multi-class support vector machine.

As presented above there is a recent trend in trying to recognize and classify automatically defects from the NDT data. However, there is not yet reported in the

literature a reliable and automatic way to recognize, characterize and classify defects from different NDT data, thus obtaining the same evaluation methodology. The present work has developed an algorithm in order to contribute to the development of such methodology.

3.4. Bibliographical review considerations

As discussed, both electromagnetic and optical techniques can be used to detect surface defects, each of which has its advantages and disadvantages, such as electromagnetic techniques can detect defects that are covered by grease, which would not be possible by optical techniques. Meanwhile, optical techniques have a higher resolution for identification generating more reliable data for automatic classification of defects. Nevertheless, as seen in both techniques, it is necessary to post-process the data in order to obtain a reliable response from the pure identification or not of the defects.

The hybridization of these techniques can be a powerful tool to industrially automate the inspection of surfaces, once their data can be processed in a reliable way and based on the same processing methodology. It is not covered in literature and there is no commercially available equipment or technique that can integrate and automate the in-line and on-line surface inspection process.

Furthermore, feature extraction is a critical process to the whole defect recognition since, without it, the classifier will not be able to work properly from poorly selected features. It is fundamental to focus on the feature extraction stage as it has a high impact on the efficiency of the recognition system but as optimized as classification algorithms may be, they still require high computational power, which can be a problem for high-speed analysis. In this way one of the focuses of the present work in the literary contribution of the development of methodologies for defect classification was developed an algorithm capable of dealing with hybrid NDT data set aiming the automation recognition, characterization and classification of defects.

The present work developed laboratory inspection methodologies based on EC, Hall sensors, structured light and laser line in order to detect surface defects under consideration of the boundary conditions of a pipe mill. To this end, it was also necessary to develop a unique form of data processing that can reliably deal with the different sources of data collected from the different techniques mentioned above, aiming not only in the detection of imperfections, but also in their dimensioning and

possible classification. Based on that, an algorithm was developed to evaluate simultaneously the raw data from these techniques in order to automatically recognize and classify eventual defects.

4. Materials and Methods

4.1. Samples

Defects in the internal and external surfaces of seamless pipes arise from different causes during the production process of this product. Both external and internal defects can occur due to defects in the surface of the tools used in the production process, as well as due to the mechanical-metallurgical processes that occur during hot rolling. Defects in the external surface of the pipe can occur due to defects in the surface of the rollers of the rolling blocks, being formed negative impressions to the defects present in the surface of the rollers in the surface of the pipe, due to the tension applied between the rollers and the pipe during the hot process. Figure 4.1 a) shows the rolling blocks and Figure 4.1 b) shows the conical shape of the rollers that constitute these blocks.

a)   b)
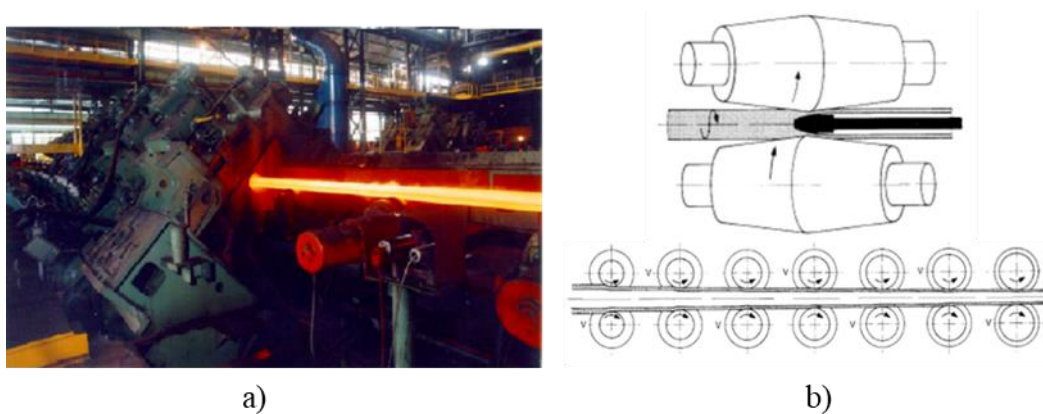
Figure 4. 1: a) Rolling blocks; b) the conical shape of the rollers.

The same phenomena happen for defects in the inner surface of the pipes, but due to the internal finishing mandrel used during hot rolling. The finishing mandrel is about 22 meters in length and is used inside the pipe, ensuring the final external diameter of the product. Figure 4.2 a) shows an example of finishing mandrel and Figure 4.2 b) shows a schematic drawing of the finishing mandrel.

a)

b)
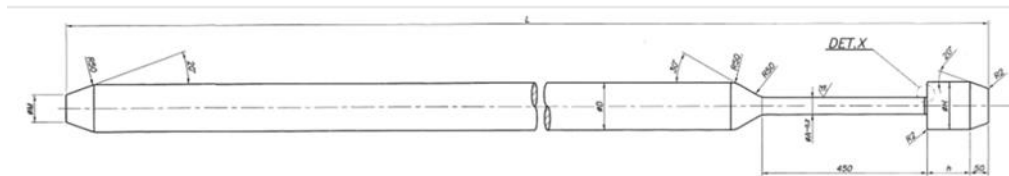
Figure 4. 2: a) Finishing mandrel in the storage area; b) Geometric details of the mandrel.

Examples of defects caused by surface defects in chucks or rollers are scratches, material pull-outs, and shallow defects of varying geometry. The metallurgical process involved during hot rolling can also generate some internal or external defects in the material. The formation of segregations in the material together with mechanical forming can create material segments that enter along the thickness of the pipe, thus generating bending and bag-type defects. These defects are difficult to detect because they are superficially similar to cracks, but subsurface have voluminous geometry. In Figure 4.3 a) is presented an example of defect coming from defects in the surface of tools and in Figure 4.3 b) is presented an example of defect coming from the mechanical-metallurgical processes of the production of seamless pipes.

Figure 4. 3: a) Defect from tool surface defects; b) rolling fold type defect.

Both the end products and the tools are ferromagnetic materials and have a response signal in the magnetic component of the impedance plane. For the present study, pipe segments of AISI 4130 steel with 232 mm of external diameter containing machined surface defects manufactured by electro-erosion, grinding and gouging will be used. AISI/SAE 4130 grade is a ferromagnetic low-alloy steel containing chromium and molybdenum as strengthening agents. The steel has good strength and toughness, weldability and machinability. AISI/SAE 4130 grade is a versatile alloy with good atmospheric corrosion resistance and reasonable strength. which are representative of the reality of the materials used both in the inspection tools and in the manufactured products. Table 4.1 to 4.4 shows the samples used in this study.

Table 4. 1: Preliminary pipe (PP) – Sample with preliminary machined defects.
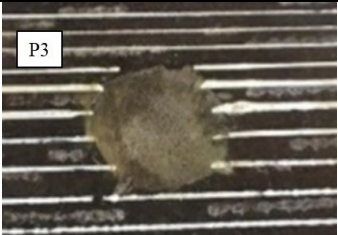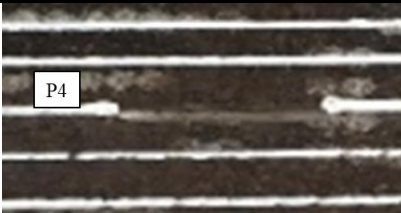
Defect	Picture
P1	
P2	
P3	
P4	
P5	

Table 4. 2: Pipe 1 with machined defects.

Defect	Pipe	Picture
Defect 1		
Defect 2	Pipe 1	
Defect 3		
Defect 4	Pipe 1	
Defect 5		
Defect 6		
Defect 7	Pipe 1	
Defect 8		
Defect 9		
Defect 10		
Defect 11	Pipe 1	
Defect 12		
Defect 13		
Defect 14		
Defect 15	Pipe 1	
Defect 16		
Defect 17		

Table 4. 3: Pipe 2 with machined defects.
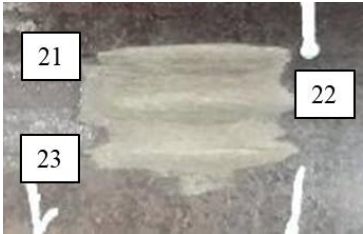
Defect	Pipe	Picture
Defect 18 Defect 19	Pipe 2	
Defect 20	Pipe 2	
Defect 21 Defect 22 Defect 23	Pipe 2	
Defect 24	Pipe 2	

Table 4. 4: Pipe 3 and 4 with machined defects.

Defect	Pipe	Picture
Defect 25	Pipe 3	
Defect 26	Pipe 3	
Defect 27	Pipe 3	
Defect 28	Pipe 4	
Defect 29 Defect 30 Defect 31	Pipe 4	
Defect 32	Pipe 4	
Defect 33	Pipe 4	

4.2. Structured light system: Digital twin – reference and control data

This work used Atos Triple Scan system, in Figure 4.4 a), by GOM company to reconstruct the surface of the samples with defects generating the digital twin, in Figure 4.4 b), of the samples to control data, i.e., this data was the reference measures for the validation of the tests carried out with the electromagnetic and the optical system. Atos sensors are used in many industries for the inspection of static parts such as sheet metals, tools and dies, turbine blades, prototypes, injection-molded and pressure die-cast parts. The functioning of structured light scanners is based in a projector shining structured patterns onto the object whose geometry distorts the structured patterns, as can be seen in Figure 4.4. Then, a camera captures the distorted structured images from another perspective. In such a system, the correspondence is established by analyzing the distortion of captured structured images with known features (e.g., phase line) projected by the projector, as described in chapter 2.2.2.

a)   b)
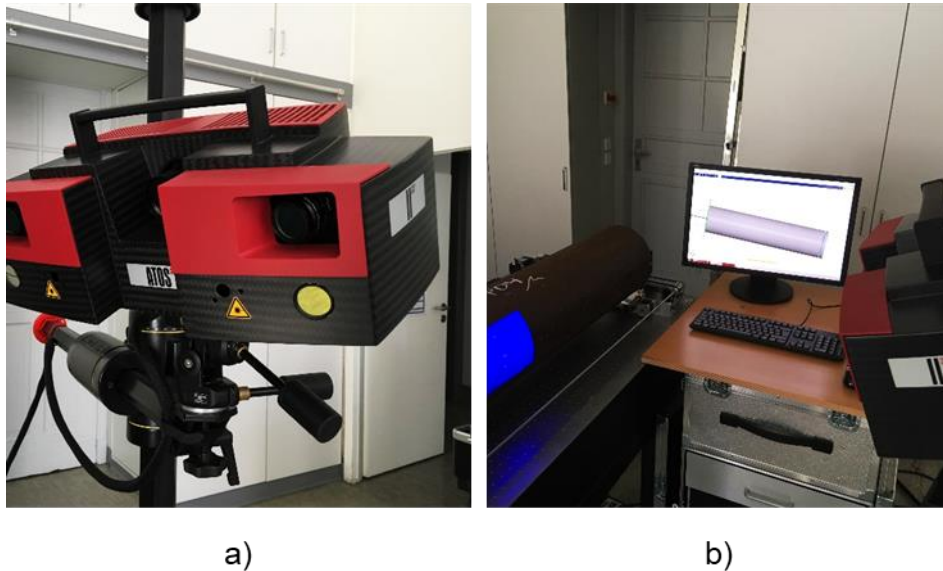
Figure 4. 4: a) Atos structured light inspection system; b) Example of surface reconstructed by the Atos system.

The diagram on Figure 4.5 shows the procedures to be followed with the light system structured to generate the samples digital twins to be used as reference throughout the project.
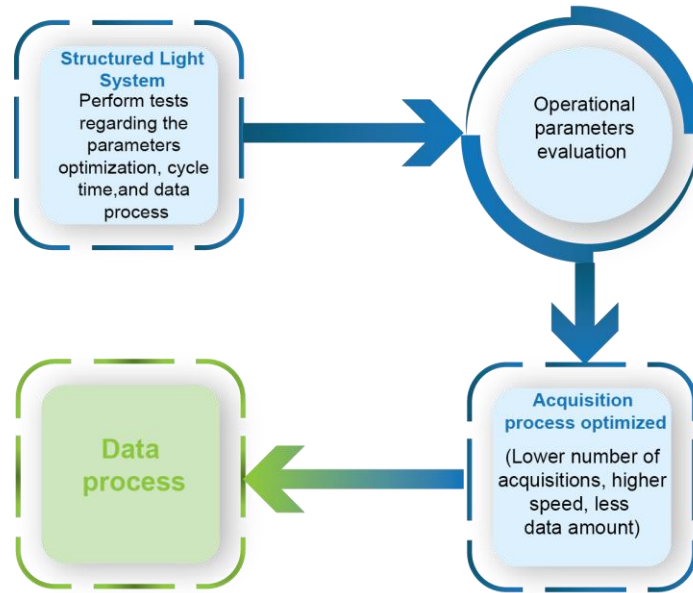
Figure 4. 5: Digital twin generation steps of the samples to be studied.

4.3. Electromagnetic inspection system

Different EC probes were developed and studied based on both absolute and differential operating modes. These sensors should have enough resolution to detect the representative defects of the manufacturing process of seamless tubes detailed in item 4.1. Computational simulations were performed to assist, optimize and validate the development of EC probes to be studied in this work. To this end, it was used the electromagnetism module of the COMSOL Multiphysics 5.4 finite element computational simulation software. In addition, hall effect sensors were instrumented on rods being used as a complementary measure to the EC, acting as a geometric sensor detecting dimensional variations in the studied samples, as well as enabled the detection of wide and shallow defects. Finally, it was built a functional prototype of this system that performed tests in the production environment, according to the scheme presented in Figure 4.6. where the sample to be inspected approaches the inspection system that adjusts itself to the cylindrical geometry of the sample, which in turn goes through the inspection system performing the measurements based on ECs and hall sensors. The raw data of the measurements will be sent directly to a computer where the developed algorithm perform the analysis for recognition of defects.
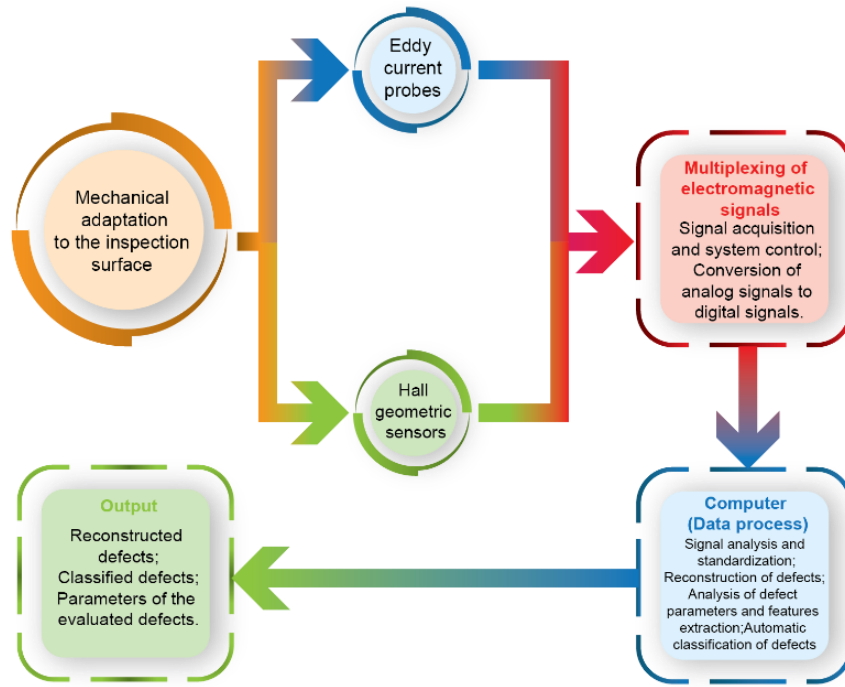
Figure 4. 6: Operational diagram of the electromagnetic inspection system.

In general, it is intended to obtain a hybrid electromagnetic inspection system for automatic inspection of the surface quality of tubular and solid products or tools with nominally constant cross section geometry throughout each inspected segment, such as tubes, spindles, axles, profiles of various geometries, plates, among others. Therefore, the objectives of the proposed system are achieved by means of an inspection system, comprehending a plurality of geometrical surface profile sensors and EC probes distributed around the cross section of the segment of the part to be inspected and an electronic circuit for multiplexing electromagnetic signals, which processes the data captured by the plurality of sensors of the system. Each geometric surface profile sensor consists of an articulated rod with a contact end that runs through the surface of the part to be inspected.

4.4. Optical 3D surface inspection system

One optical sensor based on laser line technology and triangulation principle was studied. The 3D laser scanner DSMAX from Cognex was used, it is one of the fastest and highest definition laser line 3D displacement sensor on the market for acquiring images and inspecting products in 3D having both high scan rates, up to 18 kHz, at full measurement range and maximum resolution images, 2000 profile points.

The accurate, single shot high dynamic range (HDR) image was ideal for measure and inspect very small parts, such as electronic components or steel surfaces, which can contain highly reflective or dark features. Besides that, it includes telecentric optics for optimal image formation and shadow reduction, making possible to abrupt dimensional variation without distorting the results.

To perform the tests with Cognex sensor, a prototype of an automated inspection table was built to be tested in the laboratory. This table consisted of two stepper motors, where the first have the function to rotate the pipe and the second have the function to perform the linear movement of the sensors. Figure 4.7 a) shows the DSMAX sensor an its work dimensions of circa 11 mm in high and 32 mm in width, the design of the table that was built for the external surface inspection of samples, in Figure 4.7 b) and c) in a configuration for internal surface inspection.
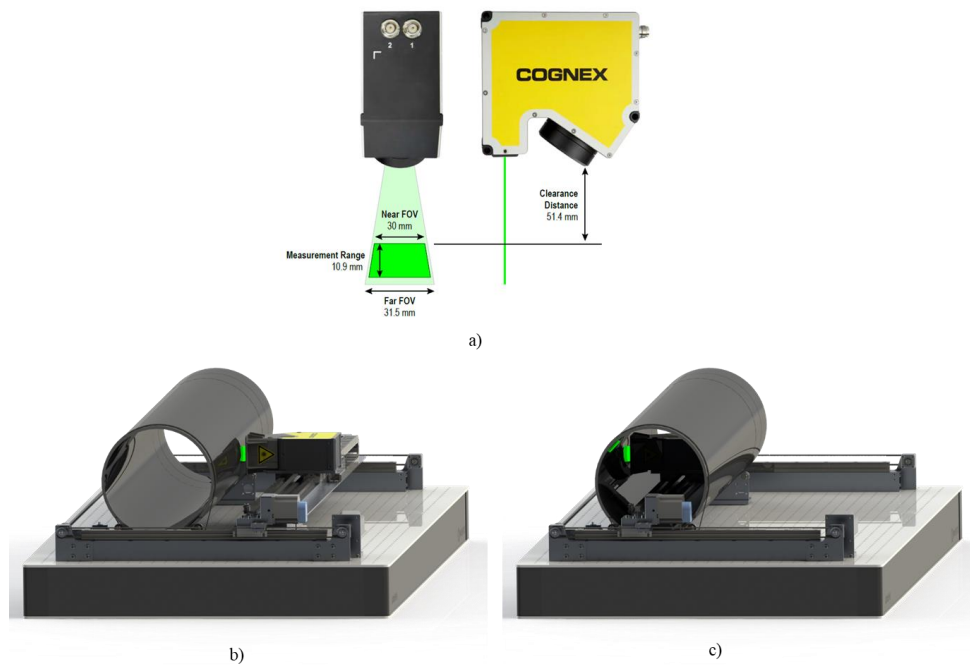
Figure 4. 7: a) DSMAX sensor; b) automatic table for external inspection: c) automatic table for external inspection.

The diagram on Figure 4.8. shows the main stages of tests that was performed for the sensor, in order to generate the data to be evaluated by the developed algorithm.
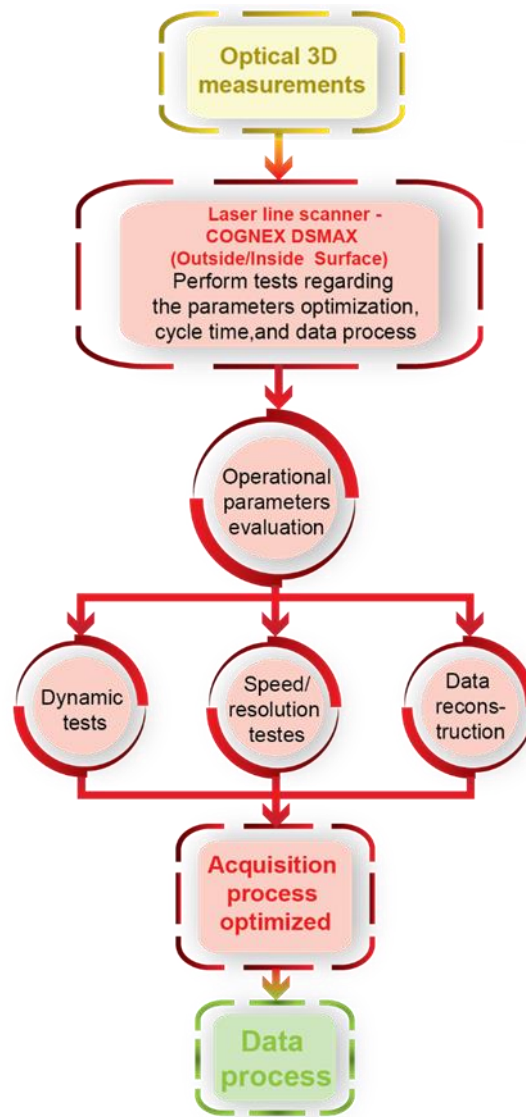
Figure 4. 8: Test steps for 3D optical techniques.

4.5. Development of the algorithm

4.5.1. Sample orientation

A key factor for the success of the proposed work is the reliable acquisition and treatment of the data, representing spatially the surface of the inspected object. To this end, a coordinate system was defined to represent the three-dimensional samples and their respective representation in the plan of the response map of the results to be presented in subsequent chapters. In general, after the measurements by any of the technologies proposed in this work, the data are converted to a two-dimensional matrix.

To map the surface points of a pipe in three-dimensional space lR³, was considered that this surface consists of points belonging to a straight cylinder of radius R contained in the space between two planes. A longitudinal and transversal axis was defined as can be seen in Figure 4.9. These points can be expressed in cylindrical coordinates according to Equation 4.1 (where r is the radius of the cylinder, ϕ is the angle formed in the xy plane and z is the height of the point) and their illustration in Cartesian coordinates are shown in Figure 4.10:
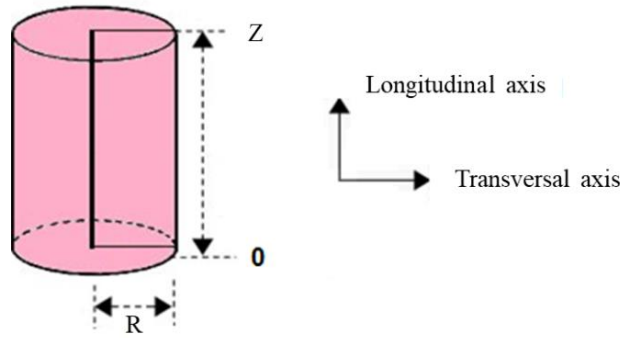
Figure 4. 9: Illustrative figure of the axle reference system for tubular samples.

$$P = (r, \phi, z); \quad for \, r > 0, \phi \in [0, 2\pi], z > 0 \qquad \text{Equation 4. 1}$$
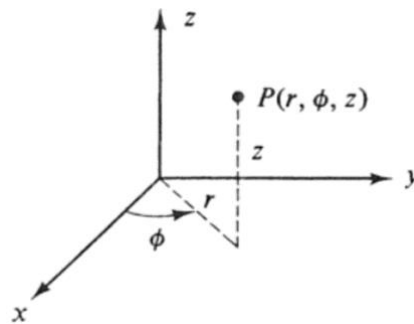
Figure 4. 10: Point relative to cylindrical coordinates in Cartesian coordinates.

Figure 4.11 shows the coordinate constraints used when a section of a specific pipe is inspected between distances Z1 and Z2 of the longitudinal axis.
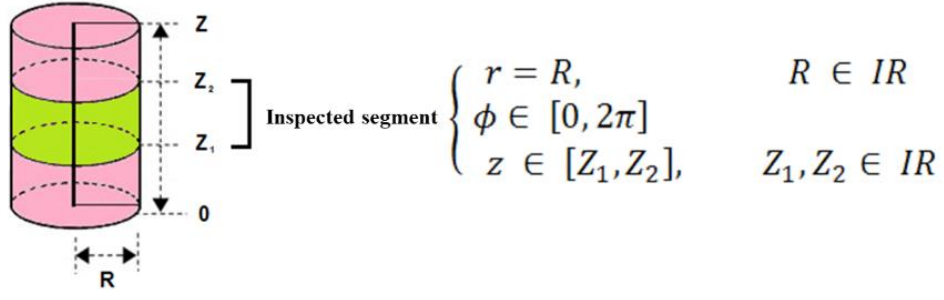
Figure 4. 11: Cylindrical coordinate restrictions for the inspection of a pipe segment with a specified length.

To transform the cylindrical coordinate system into the Cartesian planar coordinate system of the results calculated by the computational algorithm, the surface of the cylinder was planned according to Equation 4.2 and its illustration in Figure 4.12. Still in Figure 4.12 it is observed in b) and c) the performance of geometric equivalence governed by Equation 4.2 where it is necessary only a linear scale change between the parameters Φ, z and the parameters x, y of results map coordinate system. To simplify the formulation, it is considered that the image coordinate system is normalized, without loss of generality.

$$P_{(r,\Phi,z)} = (r,\Phi,z) \rightarrow P_{(x,y)} = \left(\frac{\Phi}{2\pi}, \frac{z-Z1}{Z2-Z1}\right) \qquad \text{Equation 4. 2}$$
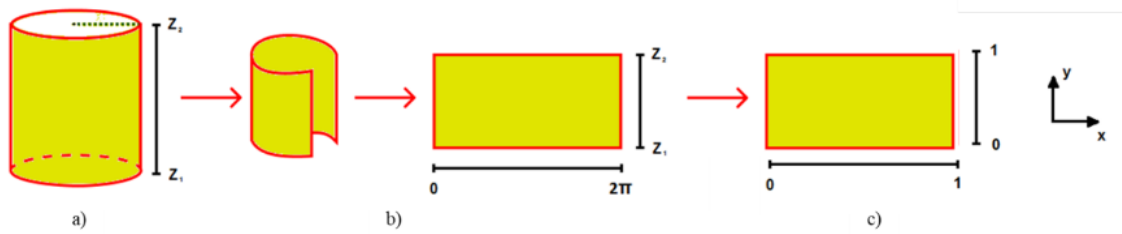
Figure 4. 12: In a) the inspected segment between Z1 and Z2 is shown, b) the cylindrical surface planning process is illustrated and in c) the illustration of the equivalence of the results in the Cartesian xy plane is shown.

82

4.5.2. Defect analysis and recognition algorithm

This work proposes to develop algorithms for the analysis of inspections performed by the reference technique, structured light, as well as for electromagnetic tests and laser scans. This algorithm was developed in python 3.7 programming language and operated by the ANACONDA 3 console. It is intended to use the libraries Plotly, Skimage, Mahotas and Shapely for plotting and data analysis, recognition of defects, features extraction and develop a defect classification proposal based on specific conditions to be further defined, in a similar way to the procedure used by the decision trees methodology. The Diagram on Figure 4.13 shows the data analysis flow:
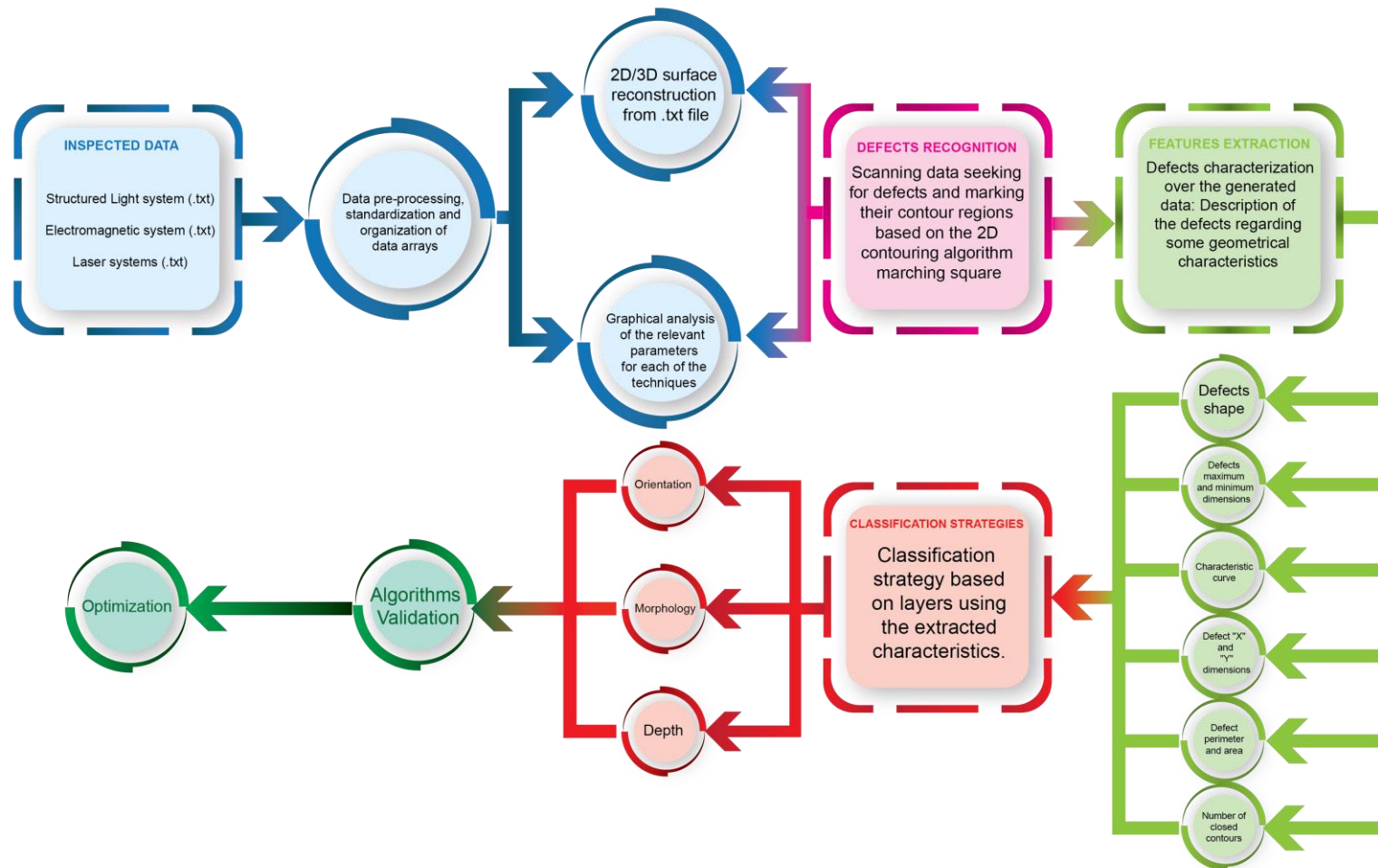
Figure 4. 13: Diagram with developed algorithm process for defect analysis and recognitions.

The classification system is based on the features extracted from the defects, passing through three classification stages, based on their orientation (longitudinal, transversal, circular, oblique, irregular and complex), morphology (crack, scratch, dent and large scratches) and indication of depth. Examples of the types of defects and their orientation can be seen in Figure 4.14.

Longitudinal

Circular

Irregular

Transversal

Oblique

Complex
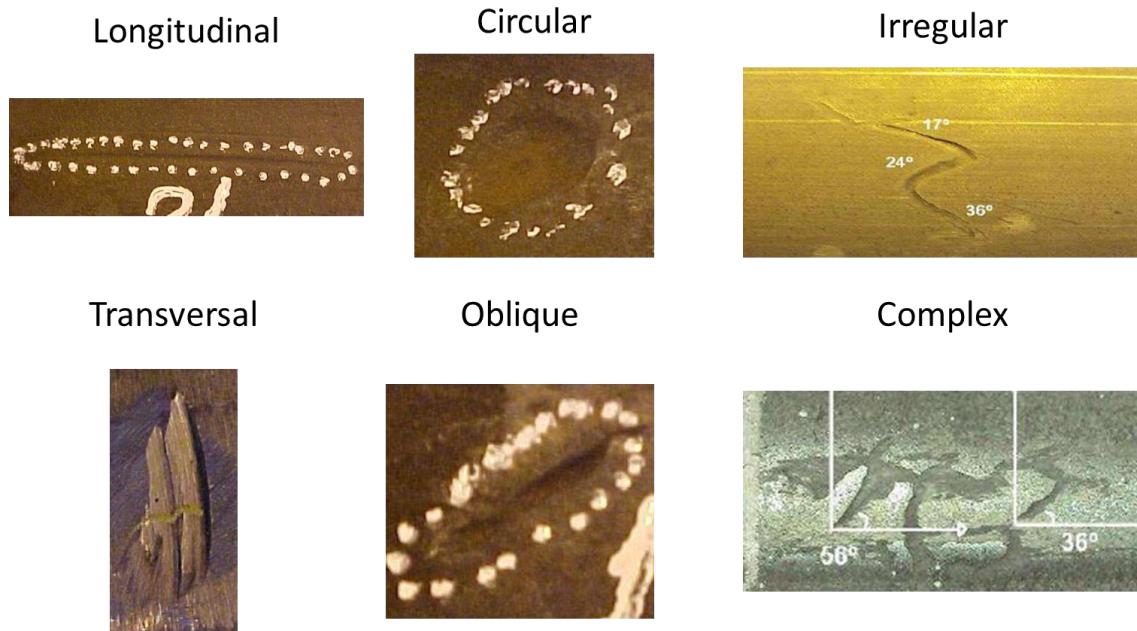
Figure 4. 14: Different defect types and orientations.

4.6. Data acquisition rate

As discussed in the introduction to this work, the automation of an inspection methodology capable of meeting inspection speeds is of great relevance, since in addition to improving the reliability of visual inspections, it also improves the industrial competitiveness. The high speed of the production line and the embedded electronics for data processing are some examples of such restrictions. A key characteristic for the development of an in-line surface defect inspection system is the inspection speed.

A high inspection speed is a boundary condition so that production cycle time is not affected. However, a high-speed inspection system can make it impossible to detect certain defects, given the probe's moment of inertia when rapidly passing over a defect, and can cause a decoupling of the probe/object interface and thus generate an unwanted lift-off signal. In addition, it requires electronics with a high data rate to achieve a

sufficiently high longitudinal resolution to meet the boundary conditions of the production line. The operating speed of an inspection system that meets the boundary conditions of the manufacturing environment can vary between 0.5 - 2 m/s depending on the product to be manufactured. To meet the longitudinal resolution requirements, the system must be able to perform at least one measurement every 0.5 mm during a 2 m/s inspection. The developments made in this work took into consideration the need for electronics that have the capacity to perform inspections up to 2 m/s, being this a great challenge.

5. Results and discussion

5.1. Structured light system – reference and control data

The first step to perform the structured light measurements is to acquire images of the sample after reference points are distributed over its surface, this procedure is called photogrammetry, as described in chapter 2.2.2. This step provides a cloud of reference points that is used during the measurement with the structured light itself. Figure 5.1 a) shows a sample already prepared for the photogrammetry process, while in Figure 5.1 b) shows the cloud of reference points obtained after this process. This process is not a necessary condition for performing the measurements with structured light, however it not only improves the quality of the test, but also reduces the time for performing the measurements.

a)   b)
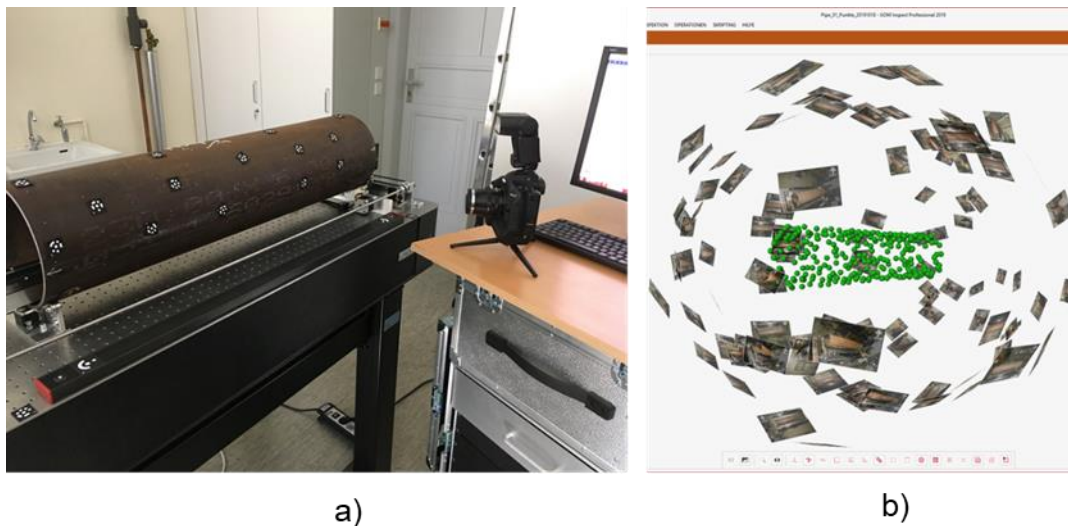
Figure 5. 1: a) Sample prepared to perform photogrammetry; b) cloud of reference points acquired after performing photogrammetry.

After the reference points have been acquired, the measurements are performed with structured light, which projects different light patterns on the surface to be inspected that distort these projections according to their morphology. This distortion of light patterns is captured by the cameras of the system and are compared with their calibration and correlated not only with the reference points that are still on the surface

of the sample, but also with the cloud of reference points acquired by photogrammetry. After that, we obtain a network with thousands of three-dimensional coordinates that go through an interpolation process, called polygonization, creating the surface of the digital twin of the samples to be used in this work. Figure 5.2 shows the test in progress, where in Figure 5.2 a) can see the beam of blue light patterns on the sample surface when performing the measurements and in Figure 5.2 b) can see the digital twin of the sample.
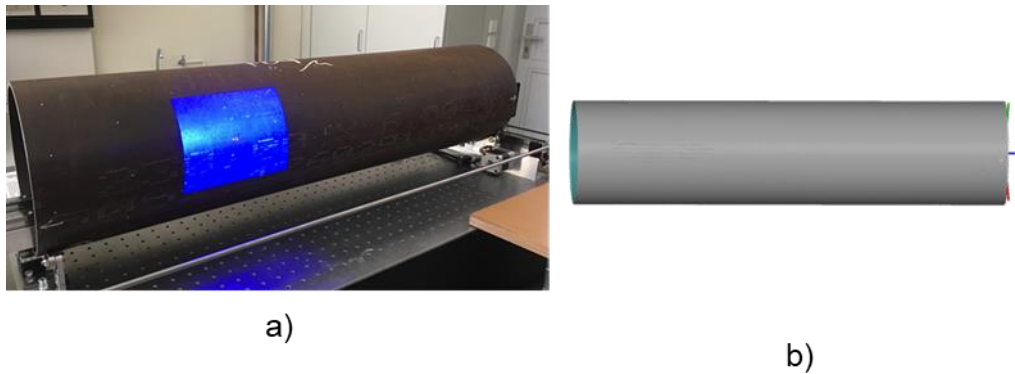
Figure 5. 2: Structured light test: a) blue area being acquired and converted into a surface; b) digital twin of this sample.

Before performing the measurements for the development of this work, a series of experiments were performed to optimize data acquisition while maintaining a high resolution combined with low data volume. In this process, parameters such as lighting intensity, exposure time, working distance, incidence angle and captured area volume were tested. Table 5.1 shows the optimal parameters found as a result of these tests and which were used afterwards.

Table 5. 1: Optimized parameters for SLS on pipe geometries.

SLS optimized parameters	
Lighting	400 to 500 nm
Shutter	3 µs
Working distance	500 mm
Acquisition rate	2 KHz
Incidence angle	27º
Captured volume	170 x 130 x 130 mm

The digital twin for all samples described in item 4.1 were performed by structured light. As a representative example of the results obtained the sample "Pipe 01" can be seen in Figure 5.3 a) as well as detailed regions of defects, which can be seen in Figure 5.3 b) to f).
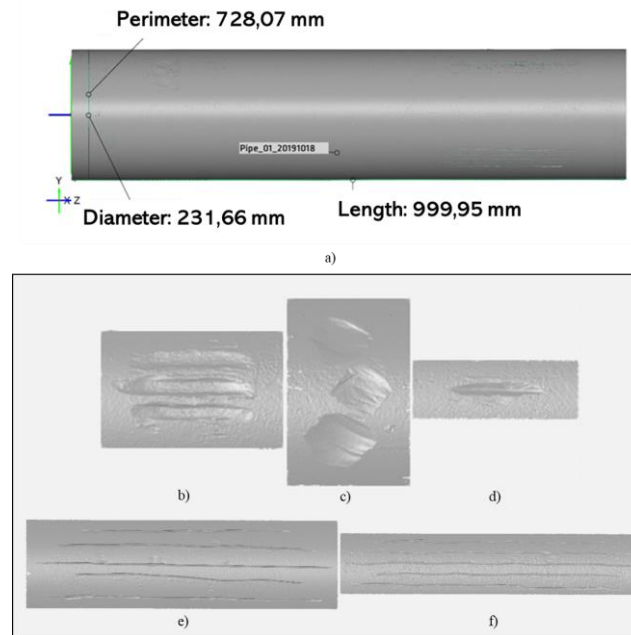
Figure 5. 3: In a) digital twin of Pipe 01. From b) to f) are the defects in details of Pipe 01.

Once the digital twin was done it is possible, through the software of the equipment itself, to make manual measurements regarding the dimensions of the defects. Table 5.2 and 5.3 show the measurements done for each one of the 33 defects presented on section 4.1 being its length, width, depth, perimeter and area. These measurements together with the digital coordinates acquired in the test are used to validate the results of other techniques performance on the developed algorithm for defects analysis and recognition.

Table 5. 2: Defects dimensions measured for the 33 defects presented on section 4.1 by SLS commercial software – Part 1.

Measurements performed manually through the digital twin in the SLS commercial software					
Defect	Length (x)	Width (y)	Depth (z)	Perimeter (mm)	Area (mm^2)
Defect 1	26.04	19.81	0.76	77.33	344.68
Defect 2	23.43	19.96	0.51	64.50	274.35
Defect 3	28.89	21.55	0.69	80.52	422.21
Defect 4	36.79	5.88	0.64	77.56	138.63
Defect 5	186.30	4.86	1.34	390.56	313.28
Defect 6	228.55	5.02	0.98	457.23	287.71
Defect 7	253.29	3.98	1.46	510.87	340.29
Defect 8	201.83	8.54	0.87	409.12	284.78
Defect 9	228.41	4.89	0.99	464.11	307.48
Defect 10	44.56	6.85	0.36	98.94	225.63
Defect 11	50.23	7.88	0.59	102.94	313.84
Defect 12	42.97	6.71	0.52	98.39	212.62
Defect 13	200.75	3.87	0.85	421.39	288.65
Defect 14	232.28	4.52	0.36	478.59	292.87
Defect 15	254.56	3.56	0.37	514.89	319.29
Defect 16	217.78	5.34	0.32	432.54	261.34
Defect 17	216.23	4.58	0.41	439.14	260.48
Defect 18	210.53	42.32	1.56	585.92	421.21
Defect 19	189.53	5.04	0.63	383.73	246.98
Defect 20	199.83	32.02	0.61	765.82	4857.89
Defect 21	47.93	5.95	0.73	100.01	195.56
Defect 22	46.21	5.56	0.67	103.06	182.97
Defect 23	47.45	4.07	0.33	92.56	145.36
Defect 24	196.04	32.06	1.52	530.38	4659.87
Defect 25	68.54	10.25	2.13	157.34	493.07
Defect 26	64.76	9.43	2.97	144.37	317.42

Table 5. 3: Defects dimensions measured for the 33 defects presented on section 4.1 by SLS commercial software – Part 2 continuation.

Defect	Length (x)	Width (y)	Depth (z)	Perimeter (mm)	Area (mm^2)
Measurements performed manually through the digital twin in the SLS commercial software					
Defect 27	45.89	11.08	1.99	110.34	397.83
Defect 28	30.01	2.10	1.72	70.06	74.89
Defect 29	99.96	0.50	0.85	204.39	83.97
Defect 30	79.83	0.50	0.93	169.34	64.34
Defect 31	40.02	0.50	0.81	100.39	30.00
Defect 32	29.28	10.70	1.10	70.03	180.36
Defect 33	25.01	2.10	1.74	76.57	78.94

5.2. Optical 3D measurements – Laser line (LL) DSMAX

No preparation of the sample to be inspected is required for the laser line testing. Once the sample is positioned on the automatic inspection table, the test is ready to start. The table has three encoder motors that have the functions to rotate the tubular sample, translate the laser sensor and adjust the distance between the laser sensor and the sample. Figure 5.4 a) shows one sample positioned on the automatic inspection table waiting for the test to be performed and in Figure 5.4 b) shows the moment during inspection of the area close to defects 10, 11 and 12.

a)   b)
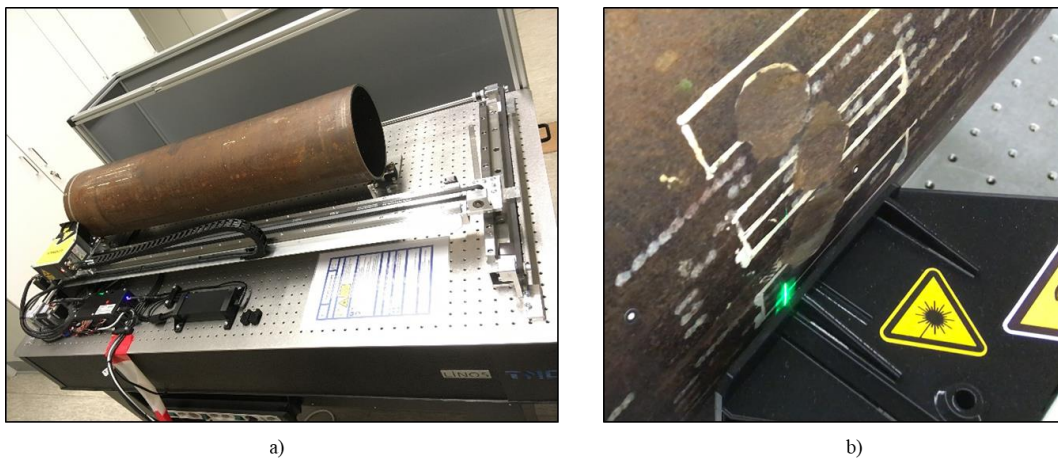
Figure 5. 4: In a) a sample is shown ready to start the tests; b) scan of a region close to defects 10, 11 and 12 is shown.

As in the structured light test, at the end of the inspection a network with thousands of three-dimensional coordinates is obtained that go through an interpolation process creating the digital surface of the inspected area. The main difference between laser line scanning and structured light scanning is that in the case of laser line no sample preparation or calibration is required, and the test is dynamic, i.e. there is the relative movement between the sensor and the sample to be inspected. Figure 5.5 shows a representative result of the laser line inspection of defect 4.
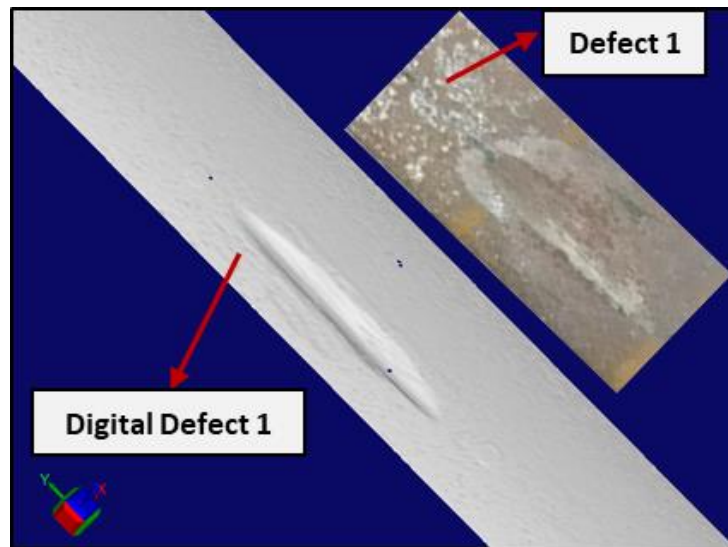
Figure 5. 5: Result of laser line scanner of defect 4.

In order to achieve optimized results in relation to the spatial resolution of the inspected areas, volume of data and quality of the inspection, it was essential to perform tests to define the inspection parameters. Thus, Table 5.4 shows the main parameters that satisfy the conditions listed for the inspection of a complete sample. The digital coordinates acquired in the test are used to compare the results of other techniques and for the development of the algorithm for analysis and recognition of defects.

Table 5. 4: Optimized parameters used for the laser line inspection.

Optimized parameters	
Shutter	2 µs
Acquisition frequency	4 kHz
Working distance	9.0 mm
Inspection speed	900 mm/s
Laser tilt	90º

Once the parameter optimization study had been performed, all samples were inspected in order to generate the data for each defect. These data were exported to the SLS commercial software in order to maintain the same measurement methodology of the defect characteristics for the optical techniques and to be able to compare the assertiveness of the inspections made by the laser line technique. Table 5.5 and 5.6 shows the results of the measurements obtained by the laser line with the optimized parameters in order to reduce the volume of data while maintaining a high resolution.

Table 5. 5: Defects dimensions measured of the 33 defects inspected by laser line Part 1.

Measurements performed manually through the Laser Line results in the SLS commercial software					
Defect	Length (x)	Width (y)	Depth (z)	Perimeter (mm)	Area (mm^2)
Defect 1	25.84	20.01	0.77	68.40	362.75
Defect 2	23.53	19.79	0.50	66.95	284.94
Defect 3	28.83	21.46	0.67	76.49	423.21
Defect 4	37.05	6.04	0.73	82.58	125.20
Defect 5	186.54	4.97	1.36	394.62	331.36
Defect 6	228.53	5.09	0.88	455.76	284.70
Defect 7	253.38	3.92	1.51	507.40	344.88
Defect 8	201.98	8.59	0.93	412.16	291.89
Defect 9	228.63	4.90	0.93	459.13	311.24

Table 5. 6: Defects dimensions measured of the 33 defects inspected by laser line – Part 2 continuation.

	Measurements performed manually through the Laser Line results in the SLS commercial software				
Defect	Length (x)	Width (y)	Depth (z)	Perimeter (mm)	Area (mm^2)
Defect 10	44.94	7.07	0.33	108.93	234.52
Defect 11	50.23	7.72	0.63	108.29	321.79
Defect 12	43.13	6.82	0.45	100.41	194.03
Defect 13	200.76	3.99	0.76	410.32	313.64
Defect 14	232.42	4.38	0.40	471.81	304.26
Defect 15	254.41	3.81	0.35	522.14	318.95
Defect 16	218.03	5.27	0.39	424.40	246.39
Defect 17	216.38	4.57	0.37	440.89	278.23
Defect 18	210.49	42.24	1.55	591.94	433.31
Defect 19	189.60	5.26	0.63	379.84	251.42
Defect 20	200.09	31.99	0.56	759.98	4882.04
Defect 21	47.97	5.79	0.73	107.10	195.07
Defect 22	46.47	5.84	0.72	106.87	194.08
Defect 23	47.53	4.10	0.25	93.82	165.14
Defect 24	196.47	32.20	1.60	524.61	4675.54
Defect 25	68.64	10.33	2.20	150.52	501.04
Defect 26	64.98	9.52	3.09	141.51	330.17
Defect 27	45.84	11.08	1.91	105.52	412.17
Defect 28	30.20	2.29	1.80	76.01	74.53
Defect 29	100.25	0.78	0.80	195.63	77.79
Defect 30	80.21	0.61	0.94	168.00	67.52
Defect 31	40.12	0.57	0.73	99.44	34.21
Defect 32	29.20	10.88	1.13	69.26	181.19
Defect 33	25.17	2.17	1.74	74.61	72.34

The results of SLS inspection and those of LL inspection are very close to each other, as expected and as can be seen in representatively by length in Figure 5.6. with standard deviation of 0.15 mm for the length, 0.13 mm for the width, 0.06 mm for the depth, 5.57 mm for the perimeter and 10.69 mm^2 for the area. Despite the small differences, in reality they are even smaller, because there is the human error associated with measurements made manually by the SLS commercial software. Figure 5.7 a) shows the result of defect 32 for the SLS data, b) for the LL data and c) shows the

automatic comparison by the commercial SLS software for this defect. This defect is interesting and representative of the others, because it has a drop shape that starts at the material surface and grows in all directions. Still in figure 5.7 c) it is possible to notice that the maximal difference in dimensions between the SLS and the LL is approximately 0.2 mm.
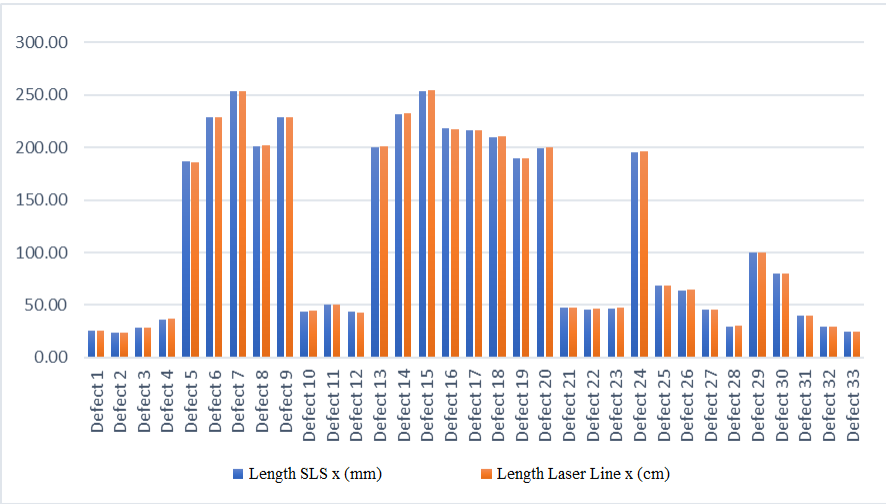
Figure 5. 6: Comparison of measurements obtained for length for SLS and LL inspections.
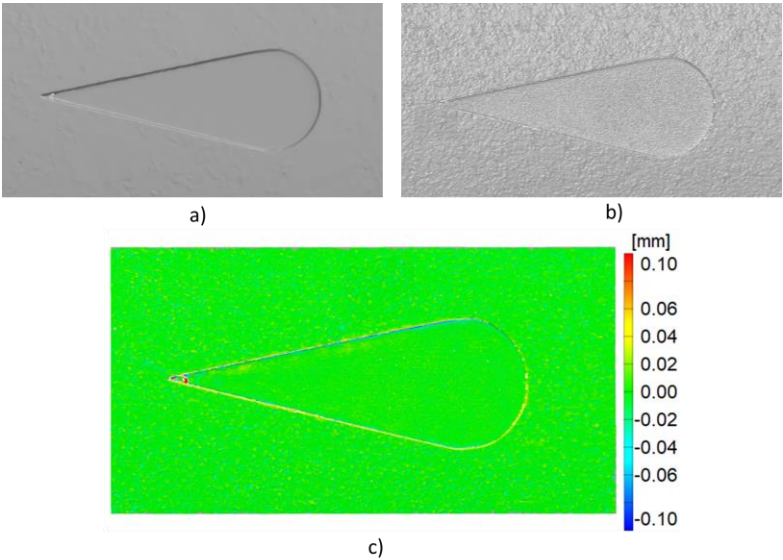
Figure 5. 7: Comparison of SLS and LL results by SLS commercial software.

A second discussion that can still be made is about the volume of data generated between the two techniques. Figure 5.8 shows a comparison of the meshes of the same

region inspected by SLS in a), and by LL in b). It is evident the great difference in the mesh of points generated, which means that the volume of data obtained by the LL is proportionally larger. However, while still observing Figure 5.8 c), which represents the dimensional comparison between a) and b), it is noticeable that there is not an expressive quality gain for the final resolution of the data. Thus, it is possible to optimize the inspection parameters by LL, as described in Table 5.4 to generate a result of the same quality and with a lower volume of data, but with the advantages associated with the LL.
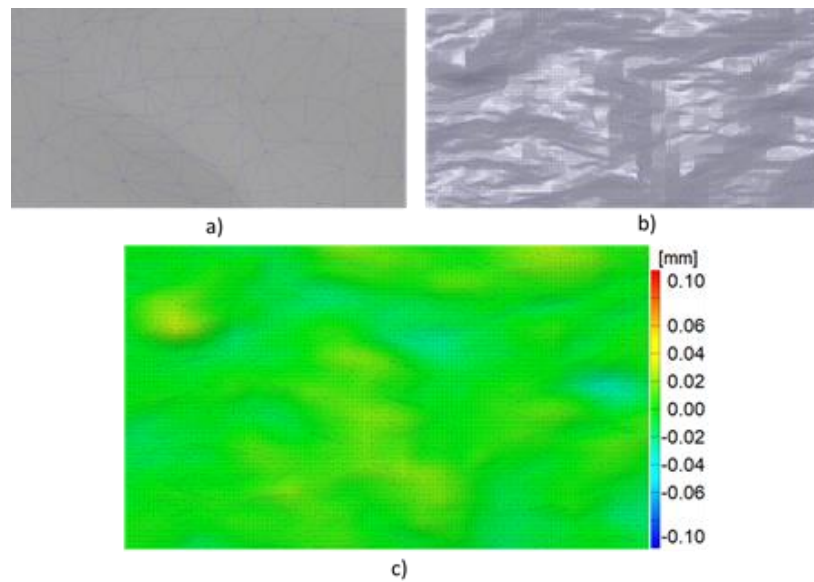
Figure 5. 8: Comparison of the point mesh generated in the same region between SLS in a) increase contrast; b) LL; c) dimensional difference.

Based on the presented results, it is possible to state that the inspection methodology developed for LL has results in resolution equivalent to the commercial SLS system. However, unlike the SLS, LL inspection is dynamic, has a low cycle time, and is easy to multiplex due to its association with encoders, making it an excellent candidate for automated surface inspection. It is also important to emphasize the importance of automating the analysis of the data generated by inspection, since the commercially available software must be operated manually, leading to a great deal of data processing time and errors related to human machine interaction.

5.3.   Electromagnetic system

In this session the development of the electromagnetic inspection methodology that hybridizes the EC technique with hall effect-based profiling will be presented. In addition, the main results acquired both in the laboratory and in the field will also be presented.

5.3.1. Proof of concept of the proposed solution

Before the actual development of the automatic surface inspection system by electromagnetic techniques, a proof of the proposed concept was performed. The concept consists in a rod, where on the top there is a hall sensor between two magnets having the function to be a profilometer based on the magnetic flux variation acquired by the hall sensor when the lowest magnet moves. Besides that, on the rod's bottom there is a small EC probe that detect small defects. Generally, the magnetic profilometer was responsible to monitor geometric variations on the surface of the material and it could also indicate large and shallow defects as a "molly whopper". ECs was also responsible for the detection of smaller defects such as cracks and scratches. Figure 5.9 shows the rod's concept.
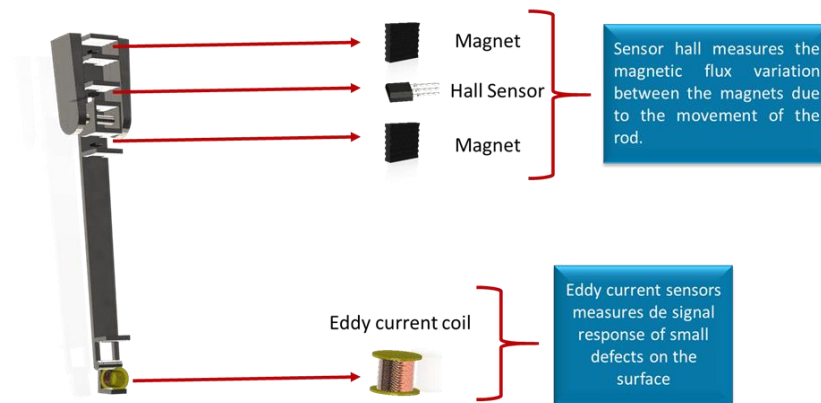
Figure 5. 9: Concept of proposed solution.

Although this solution can be applied to both external and internal pipe surfaces, this work focus on the development of the solution for inspection of external surfaces as for example pipes and mandrel bar. Since the external inspection geometry of products (pipes) and tools (mandrel) has a cylindrical shape, the proposed concept for an external device is a ring with several rods, as can be exemplary seen in Figure 5.10.
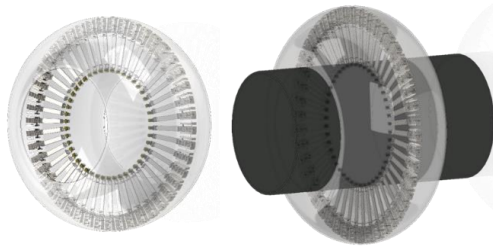
Figure 5. 10: Ring concept of the inspection system.

Figure 5.11 shows the results of this preliminary test, where it is possible to see the potential of the methodology for defect detection. The results presented in Figure 5.11 show the detection of the defect both by EC and by the profilometer based on Hall sensor. As the use of the profilometer was a measure focused on the variation of the geometric profile of the sample throughout the inspection, this work focuses on the development of EC sensors enabling them as a solution for in-line and on-line inspection in the pipe mill processes.
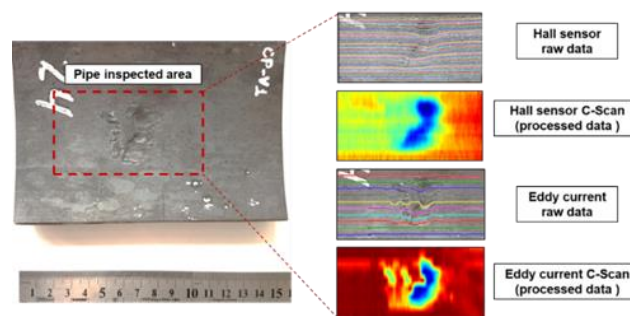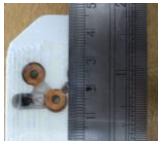
Figure 5. 11: Inspection result for both EC and Hall sensor.

In subsequent sessions the development and optimization of both EC sensors and Hall sensor-based profiling as well as their representative experimental results will be shown in detail. It was decided to segregate the EC probes from the bottom of the rod aiming the optimization of the mechanical robustness.

5.3.2. Eddy current probe development

In order to analyze the best coil configuration for defect detection in tubular surface, several EC probes with different geometries and operational mode were studied. The PP sample was used for this study. Table 5.7 presents the main configurations of the evaluated probes and a brief evaluation of their results.

Table 5. 7: Several EC probes evaluation.

Evaluated probes

Coil	Operation mode	Coil diameter (mm)	Picture	Evaluation
Coil 1	Absolute	27.5 x 16		It showed good detection of defects, except for longitudinal ones. This is due to the fact that the oval coil has different sensitivities according to the defect orientation.
Coil 2	Absolute	18.5		Detected all defects, but with low signal-to-noise ratio. Smaller defects had their detection affected, which may be associated with high noise and coil diameter.
Coil 3	Absolute	9.5		Detected all defects with good signal-to-noise ratio. In relation to Coil 2. the frequency used was lower and the diameter corresponds to approximately half, factors that facilitated the detection of small discontinuities.
Coil 4	Differential	13.6		It was possible to detect all defects, but the signal-to-noise ratio was unsatisfactory.
Coil 5	Differential	7		It detected all defects with a higher signal-to-noise ratio. Compared to the previous coil versions, this one had its diameter reduced and a ferrite core was added.

Both probes 5 and 3 showed good defect detection capacity on tubes surface. Hence, it was defined that the best coil for the development of this project would be coil 5 because it showed good results for the detection of defects and it was built with two coils connected in a differential mode, which reduces the influence of lift-off and microstructure variations throughout the inspection. The main construction parameters of coil 5 are summarized in Table 5.8.

Table 5. 8: Main construction parameters of coil 5.

Parameter	Value
Diameter (Ø)	8.0 mm
Number of turns (N)	800
Height (H)	3.5 mm
Ø core	3.5 mm
Core type	Ferrite
Wire	AWG 38

Operating frequency optimization of Eddy current probes via COMSOL Multiphysics® 5.4:

Since coil 5 was defined as the best coil to be applied for inspection of defects in tubular surfaces, the optimization process of the coils operating frequency was initiated. Frequency is the main parameter for the detection of defects, since it will control the penetration depth of the ECs and, consequently, the current density in the material.

To optimize coil 5 operating frequency, a computational model was performed where coil 5 scans the defects along the PP sample, ranging the operating frequency of the coil from 1 to 10 kHz. The proposed system was modeled using finite element

analysis (COMSOL Multiphysics 5.4). The model was set up using AC/DC module and magnetic interface of COMSOL (Multiphysics, 2018). The probe is a small array sensor with a group of 4 helicoidal coils in the transmit-receive mode. While large sensor arrays are generally required for inspecting through thick materials, coatings or insulations; small sensor arrays can be used to create high spatial resolution property images (ZILBERSTEIN, SHAZ *et al.*, 2013) (Multiphysics, 2018). Initially, the PP sample with it is defects, coil 5 and mesh environment were modeled to be applied in the simulation. Figure 5.12 a) and b) shows the model of sample PP, with 2000 points along its length a 10 point along its diameter, used in the simulation and in Figure 5.12 c) shows the sample PP used in this optimization process. Besides that, 5000 points were used for each defect region. Figure 5.13 a) shows the model of coil 5 used in the simulation and in Figure 5.13 b) shows the used mesh for the coil 5 model. The mesh used for this simulation has a growth rate of 1.3. being a maximum size per element of 15 mm for non-complex regions and a minimum size of 0.3 mm for more complex regions, being close to the regions of the defects. Electromagnetic properties of carbon and low-alloy steel were used as input parameters of the model (σ = 10.60% IACS and μ = 1.01 H/m). The control user meshed function of COMSOL was used with a specified minimum element size of 0.03 mm. Figure 5.14 shows the mesh surrounding PP sample simulation.
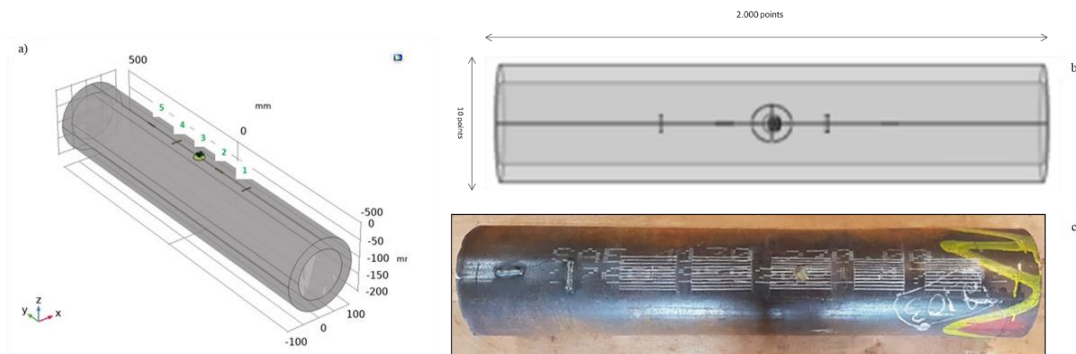
Figure 5. 12: In a) and b) are shown the different views model of sample PP used in the simulation; c) shows the sample PP used in this optimization process.
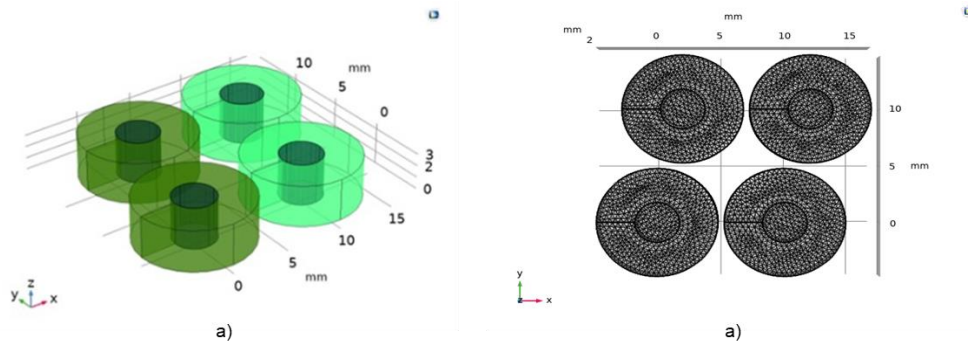
Figure 5. 13: In a) is shown the model of EC probe used in the simulation; b) shows the used mesh.
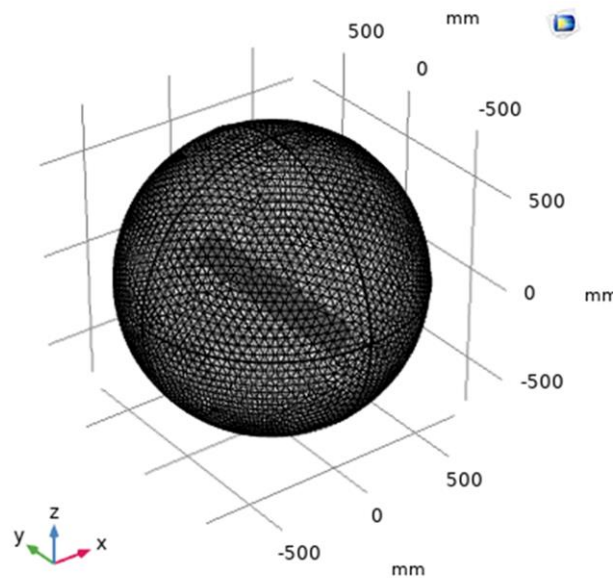
Figure 5. 14: Mesh used in the simulation to optimize the frequency.

The parametric study was solved for four different excitation frequencies: 1 kHz, 3 kHz, 5 kHz and 10 kHz. These frequencies are related to the penetration depth. The penetration depth is limited by the skin depth at high frequencies and by the sensor geometry at low frequencies (GOLDFINE, SHEIRETOV, 2008). Since EC techniques use an AC current to excite the coil with one frequency, the skin depth is limited to one depth of penetration which relates to the depth at which the field amplitude has decreased to 1/e in comparison to its value at the surface (GEDNEY, 1994). The simulation results for the frequency variation can be seen in Figure 5.15. It is noticed that there is not a very significant variation for the absolute impedance, but the frequency of 5 kHz showed to be the more stable frequency to absorb any fluctuation,

with a better continuous response in relation to the amplitude signal, and generating slightly a better signal for the detection of defects.
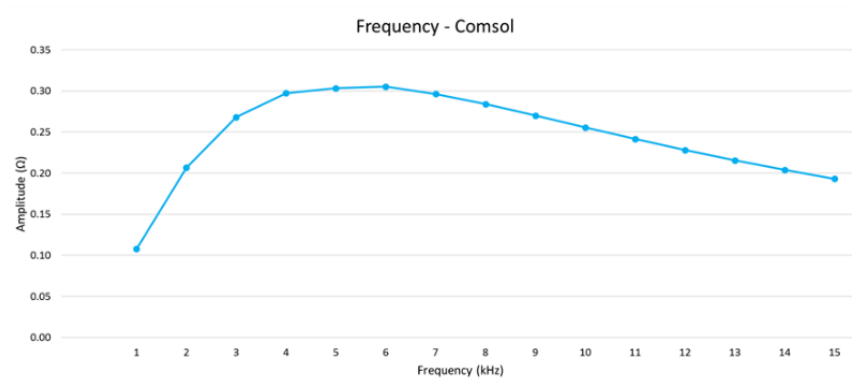
Figure 5. 15: Frequency optimization *scan result.*

Figure 5.16 shows the result in impedance of the simulation using the frequency of 5 kHz for the inspection along the sample PP. It is possible to clearly see the detection of all defects present in the sample PP.
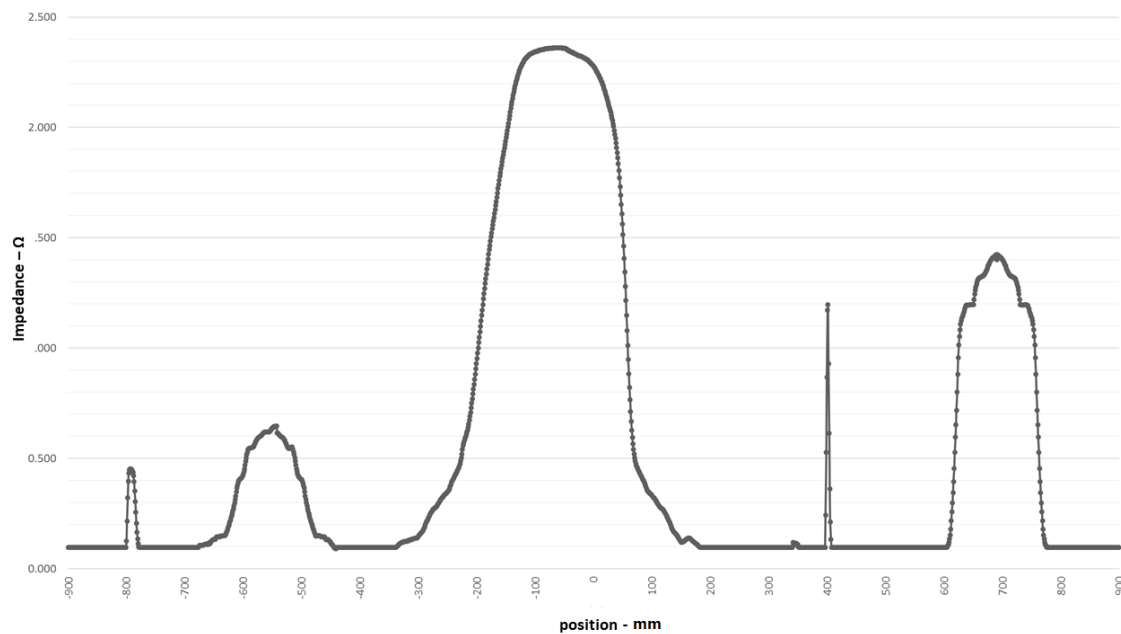
Figure 5. 16: Detection of the 5 defects of the PP sample in impedance along the inspection.

Validation of the computational model with physical tests:

In order to validate the results found in the simulation, real scans with frequencies of 1, 3, 5 and 10 kHz applied to coil 5 were performed. The smallest defect of PP sample, defect 4. is shown as an example of the results of the real tests in Figure 5.17 and Figure 5.18. where the frequency variation of 1, 3, 5 and 10 kHz are respectively represented from a) to d) in both figures. It is possible to observe through these results that although it is possible to detect this defect in all frequencies, the frequency of 1 kHz presents the worst noise signal ratio, while the frequency of 5 kHz presents the highest intensity of the response signal in impedance. This difference in results between the optimized frequency of 5 kHz and the nonideal frequency can be explained for a penetration depth variation of the current flow induced by the probe into the material, since this depth is inversely proportional to the frequency, as shown in Equation 2.1.
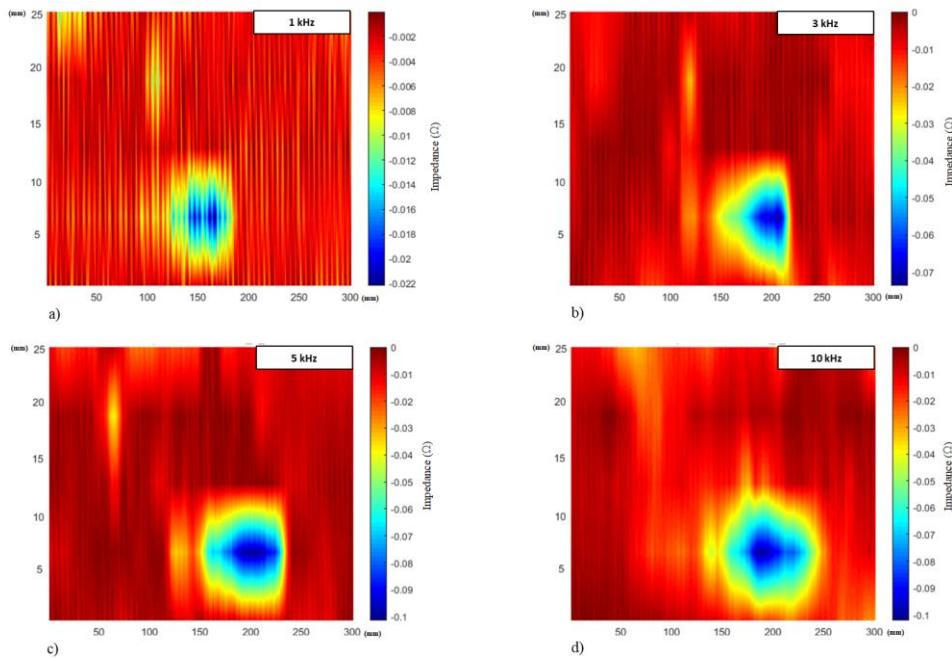
Figure 5. 17: 2D Inspection impedance map of sample PP with coil 5 for different frequencies.
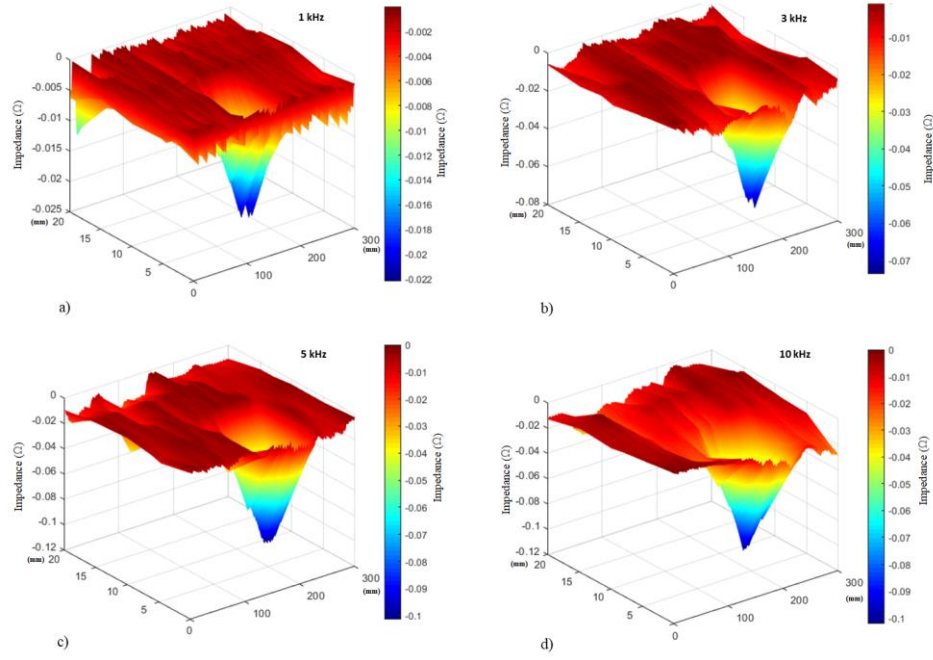
Figure 5. 18: 3D Inspection impedance map of sample PP with coil 5 for different frequencies

For frequency values below the optimized one, the penetration depth increases, reducing the current density on the surface of the sample and consequently reducing the amplitude response of the defect in relation to the base signal of the tube, since defect 4 is shallow. On the other hand, for values above this frequency, the penetration depth drops, preventing the current flow from interacting with the full depth of the defect, reducing its response signal. Figures 5.19 and 5.20 show the detection of defects 1, 2, 3 and 5 of sample PP by the inspection of coil 5 with the optimized frequency of 5 kHz.
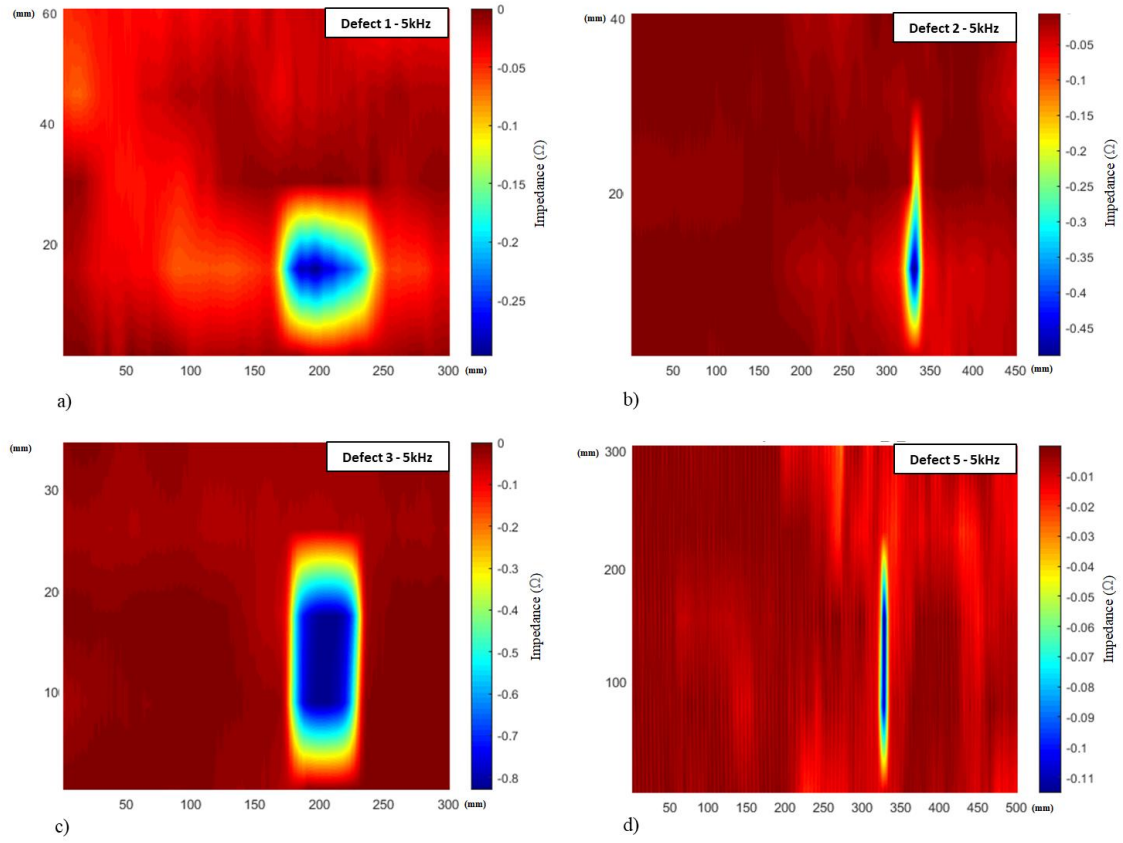
Figure 5. 19: 2D impedance inspection map of sample PP with coil 5 with the optimized frequency of 5 kHz. Detection of defects 1, 2, 3 and 5.
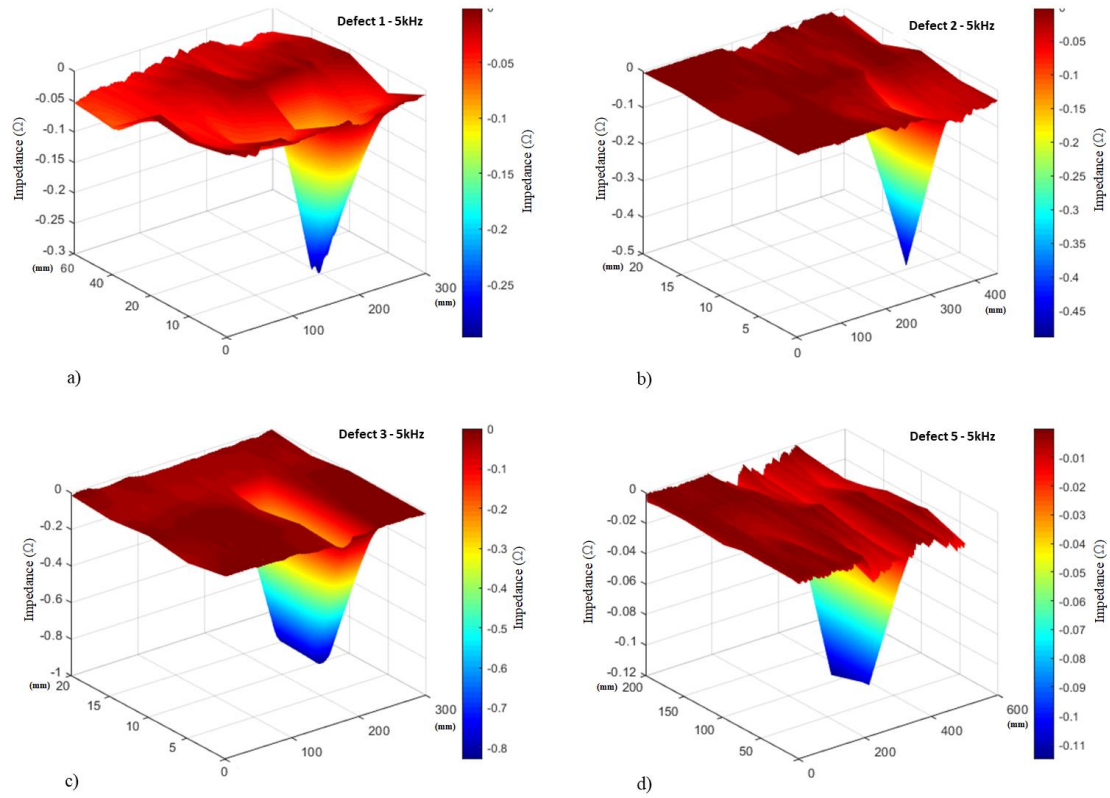
Figure 5. 20: 2D impedance inspection map of sample PP with coil 5 with the optimized frequency of 5 kHz. Detection of defects 1, 2, 3 and 5.

Figure 5.21 shows the impedance result of the real test using the frequency of 5 kHz for the inspection along the sample PP, described on Table 4.1, and Figure 5.22 is the overlap of actual and simulation results, validating the simulation and the experiments.
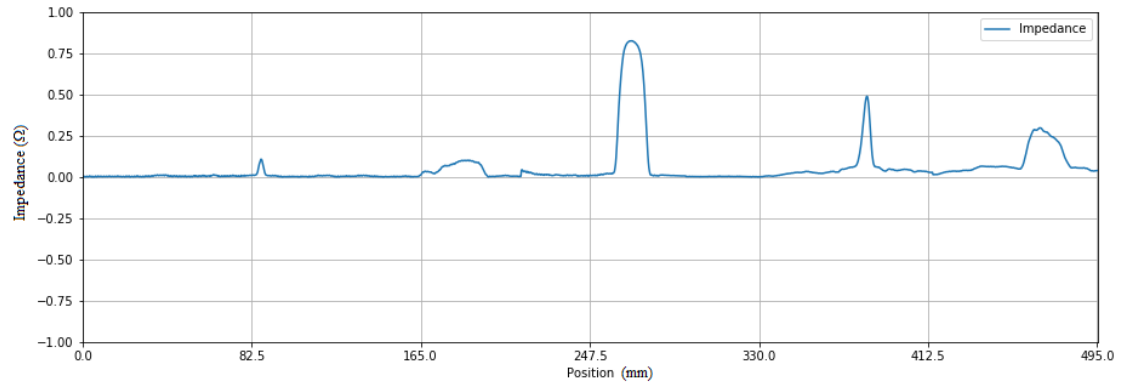
Figure 5. 21: Detection of the 5 defects of the PP sample in impedance along the real inspection.
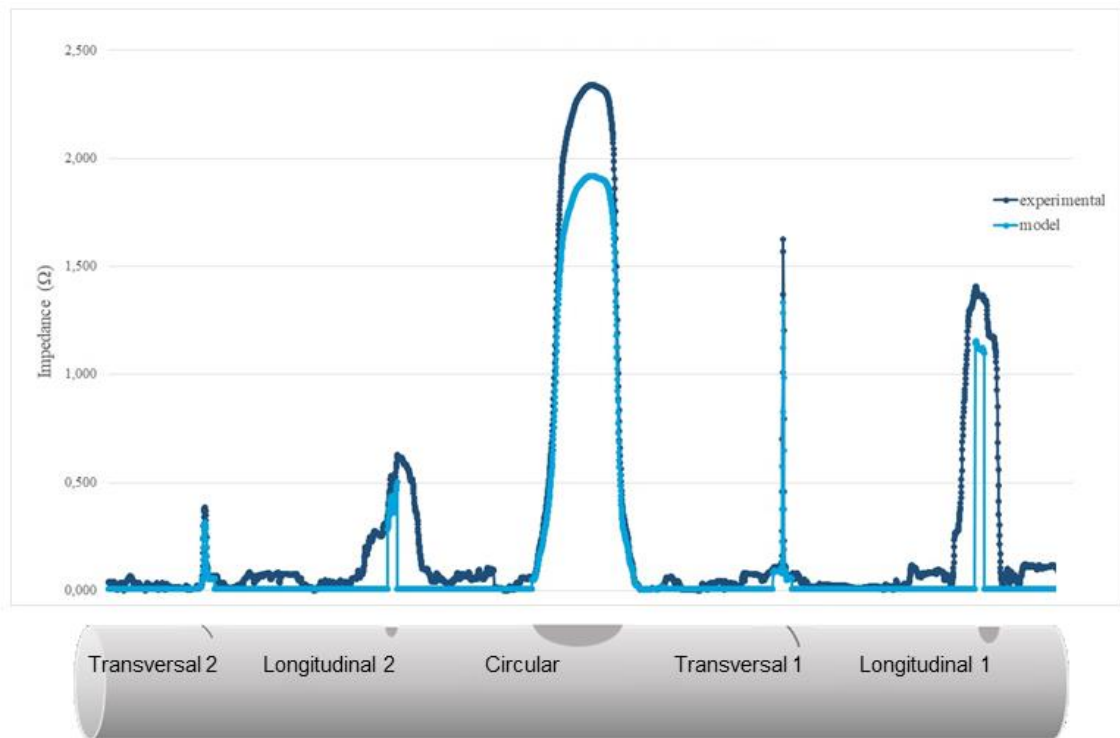
Figure 5. 22: Matching the results of the simulation and of the actual tests for the PP sample inspection with the coil 5 and optimized frequency of 5 kHz, showing the validation of the simulation with the experiment.

Therefore, through the COMSOL simulation and the tests performed in the PP sample, it was shown that coil 5 is not only capable of detecting defects with good
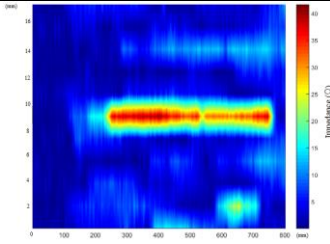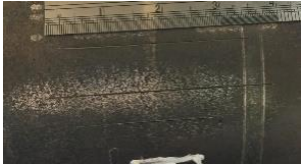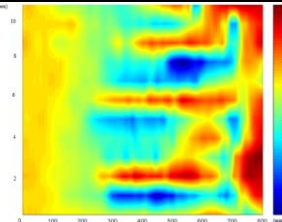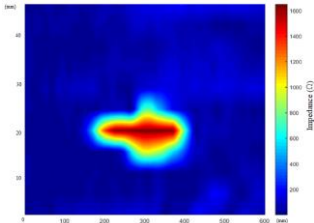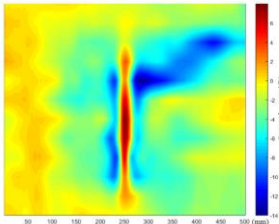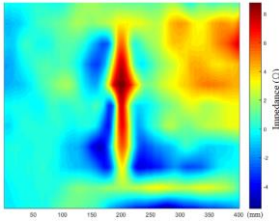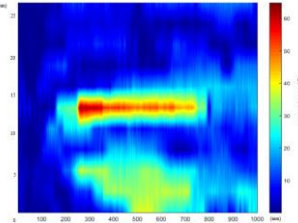
signal-to-noise ratio, but also that its optimal operation frequency for detecting surface defects in tubular surfaces is 5 kHz.

EC probe sensitivity tests:

After optimization of the construction parameters and operating frequency of the EC probe, tests to evaluate the sensitivity of the developed probe were performed. For this purpose, inspections were performed manually along the axial axis of the sample body and each inspection was circularly spaced of 16 mm, i.e., there was no blind spot between inspections. The applied operational parameters of the inspection were: Frequency = 5 kHz; Supply voltage = 4 V; Gain = 32 dB; Rotation = 242° and Vertical Gain = 10 dB. Table 5.9 summarizes the results representative of the smallest defects described on Table 4.2 – 4.1.

Usually the impedance vector amplitude value is used for defect detection. However, in a more complete analysis the four variables related to the EC test (impedance vector amplitude, impedance vector phase, resistance and inductive reactance) are evaluated. The first two are related to the last two through vector transformations. Analyzing the inspection data, it was observed that the phase variable does not contribute to the detection, as expected. Moreover, because of the small geometry of some defects, they are better detected by the components of the impedance vector (resistance and inductive reactance) rather than by their own amplitude. Thus, it is shown that the smallest defect detected, in laboratory conditions, has dimensions of 30 mm x 0.5 mm x 0.8 mm (length X width X depth).

Table 5. 9: Representative results of the sensitivity tests.

Defect	Eddy currents response

Probe construction and robustness testing:

After the development of the EC probe and the respective sensitivity tests, the construction of the probes to be used in the prototype inspection system began. Figure 5.23 shows in a) the probe design and in b) the probe already built. As can be seen in Figure 5.24 the probes have a special design with a curvature to perform a better coupling on the cylindrical surface of the mandrel/tube and have a rubberized region to receive the impact and ensure that the probe is straight and parallel to the inspected surface throughout the inspection. Figure 5.24 illustrates the behavior of the probe and geometric sensors throughout the inspection of cylindrical geometry.
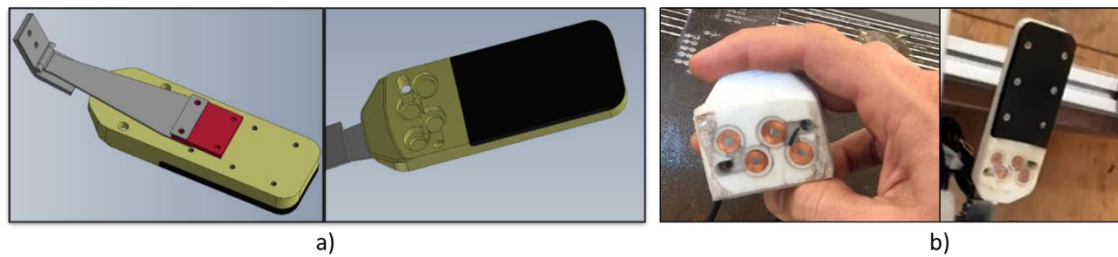
Figure 5. 23: In a) design of the EC probe to be used in the prototype and in b) probe assembled to be used in the prototype.
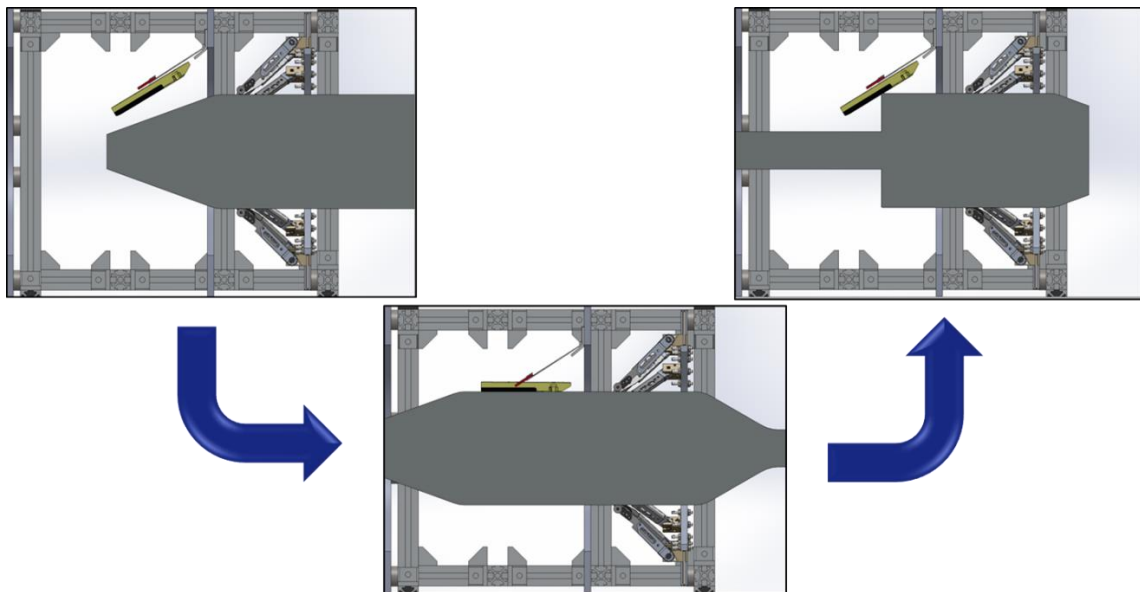
Figure 5. 24: Working inspection system illustration, where the dynamics of the EC probes and geometric sensors can be observed.

As one of the objectives of this work is the construction of the prototype for production line tests, robustness tests were also performed on developed components. For this, a curved bulkhead was used, with a rough surface, fixed on a rotating disk. The probe was suspended on a fixed bar, so that the rotation of the disk would cause an impact of the bulkhead with the probe. Figure 5.25 shows the experimental apparatus used. In this test, a rotation of 150 rpm was used on the disc, lasting 96 h, making a total of 864.000 impacts between the bulkhead and the probe. After the end of the test, the probe showed no appreciable wear that could compromise its coupling in the tube or its positioning.
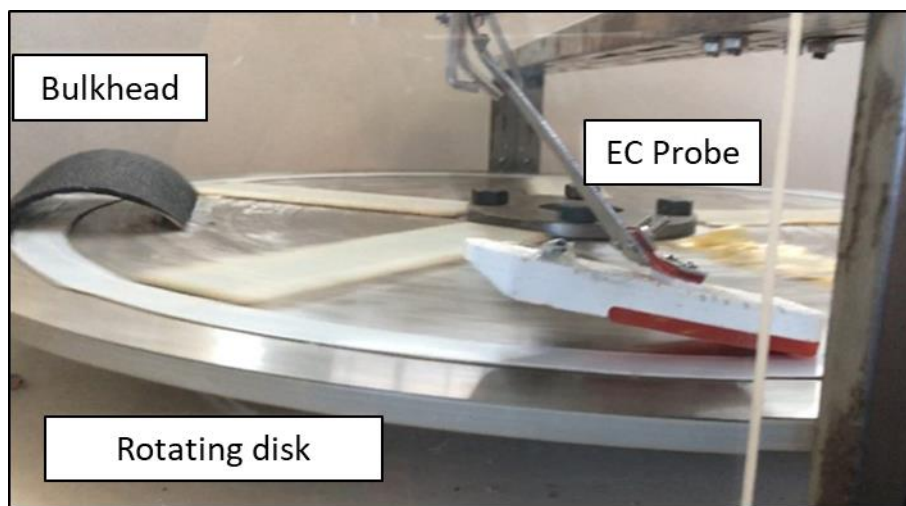
Figure 5. 25: Probe robustness test setup.

5.3.3.   Construction of geometric sensors – Hall:

The second essential component of the developed electromagnetic prototype in this work are the geometric sensors based on the Hall effect. Basically, the angular variation of the rod implies a variation of the magnetic flux that passes through the Hall effect sensor, exciting it and thus generating voltage measurements. Through these measurements it is possible to compose the profile of the inspected region with resolutions smaller than 1.0 mm in the longitudinal direction. Figure 5.26 a) shows the rod design of the geometric sensor and in b) shows the geometric sensor already built. As with EC probes, these components were also submitted to the same robustness tests having similar results.
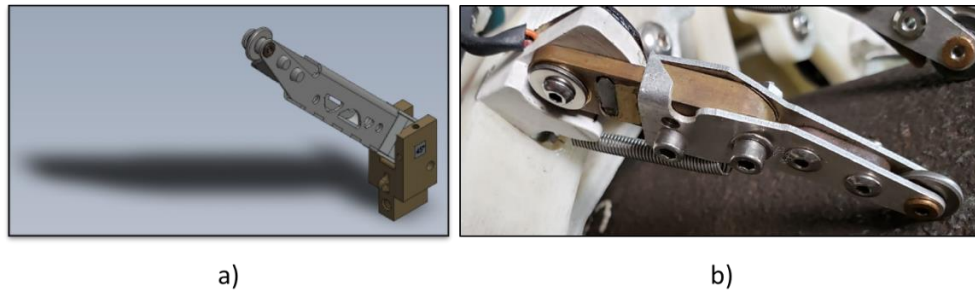
Figure 5. 26: In a) design of the geometric sensor to be used in the prototype and in b) geometric sensor mounted to be used in the prototype.

The geometric sensor is made with a pair of magnets that rotate around a Hall sensor fixed on its axis, thus, who turns is a magnet and the electronic component is fixed. If the magnets rotated 360 degrees the pair of magnets around the axis, a senoid would be obtained. However, the angle at which the geometric sensor will work is defined, i.e. what the thickness range and accuracy will measure. The Hall sensor used in this work originally generates a senoid of +5 V to -5 V, however for the application in the geometric sensor the range from +1 V to 4 V are used. This is done so that the used range approaches a straight line, avoiding the maximum points and also the passage through the zero. Between 4 V and 5 V the senoid curve is disadvantageous, because a small variation in the position of the sensor in relation to the magnet means a huge variation in the measurement. In the range between +1 V and +4 V, there is a more uniform behavior according to Weid et al., (2008).

It is important to note that each sensor has a different response, depending on: 1) natural variations of the Hall sensor; 2) natural variations of the magnet; 3) variations in the mechanical assembly of the sensor. For this, all sensors were previously calibrated, in a distance scale, as can be seen in Figure 5.27. The distance scale represents all the thicknesses that must be measured by the sensor, representing the measuring range.
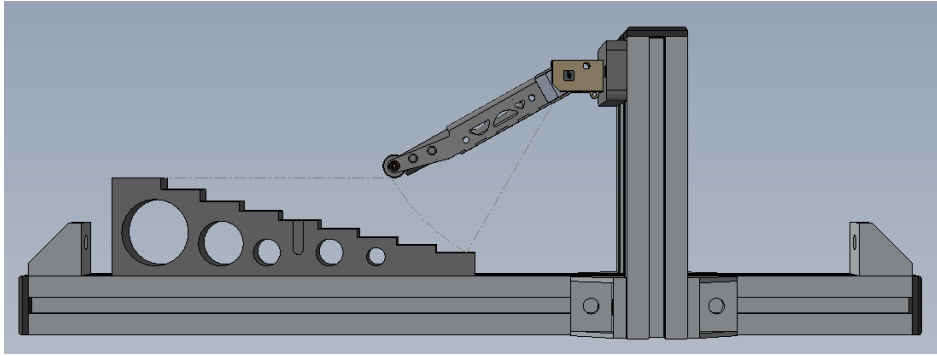
Figure 5. 27: Distance scale for calibration of geometric sensors.

To perform the tests on some of the defects described in section 4.1, a trolley associated with a geometric sensor was built and can be seen in Figure 5.28. With the help of this cart, a measurement matrix was performed, and the results can be seen in table 5.11. It is possible to observe in the results presented in Table 5.10 the good signal noise ratio in the detection of defects in the longitudinal direction, however the lateral resolution depends on the distance of steps, or between sensors, being directly proportional to this clearance.
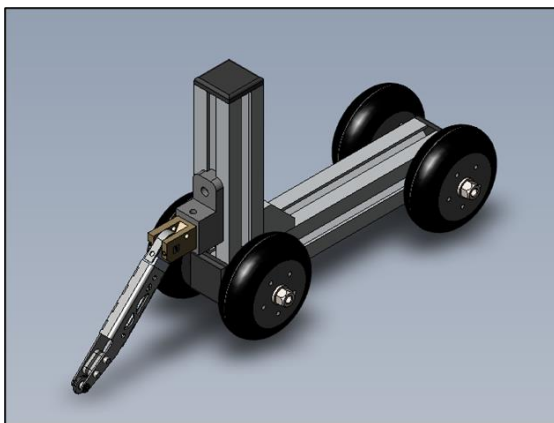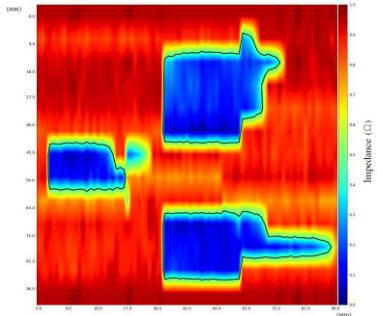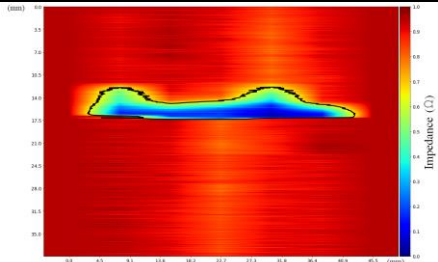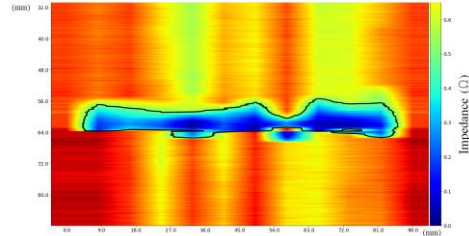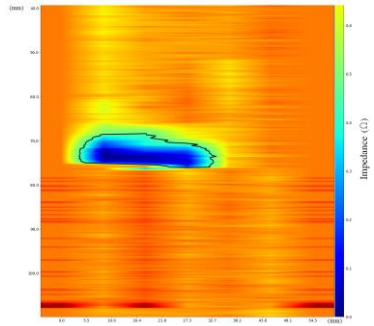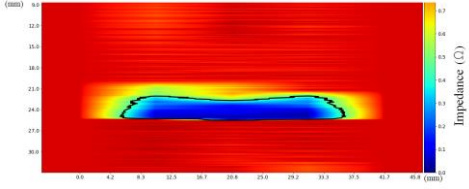
a)   b)

Figure 5. 28: Inspection trolley model for geometric sensor in a) and inspection in progress in b).

Table 5. 10: Representative results of the geometric sensor tests.

Defect	Eddy currents response

Electromagnetic prototype assembling and laboratory tests:

The inspection system was designed to have a set of 16 geometry sensors and 18 EC probes. Each EC probe has 4 EC coils connected in a differential way to make 2 pairs. That means in the end that, a total of 36 EC channels were divided in 18 probes, covering the mandrel surface. Finally, Figure 5.29 shows in a) the prototype design of the inspection system and in b) the prototype already assembled and ready to be tested.

a)   b)
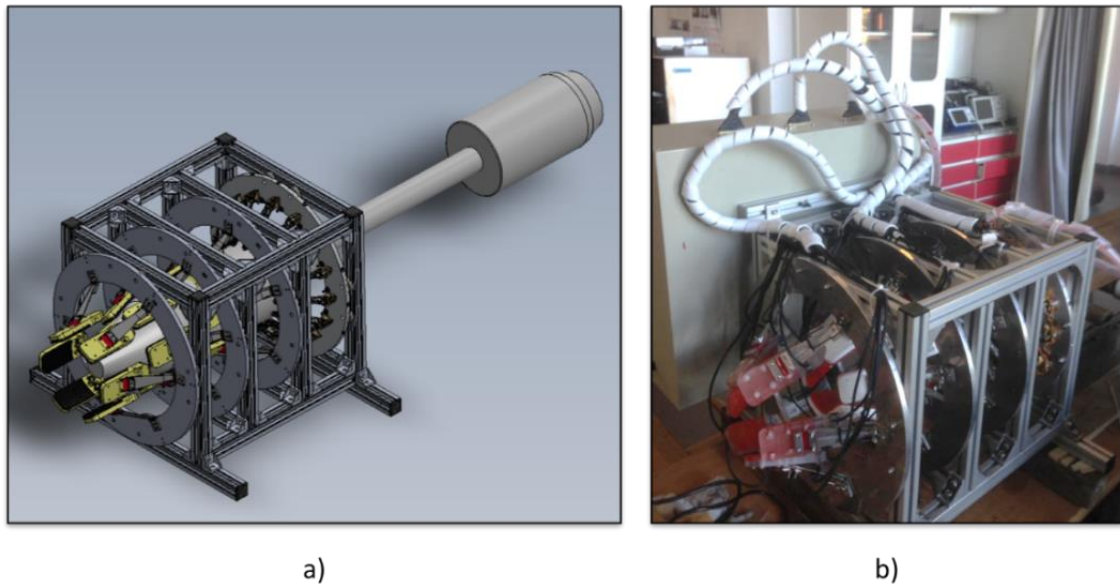
Figure 5. 29: Design of the prototype inspection system in a) and b) the built prototype.

After the construction of the prototype, laboratory tests were performed to verify the system. These tests were performed by passing samples of tubes manually through the inspection system. Figure 5.30 exemplifies the dynamics of the tests and Figures 5.31 and 5.32 show respectively the representative results of the tests with the geometric sensors and with the EC probes.
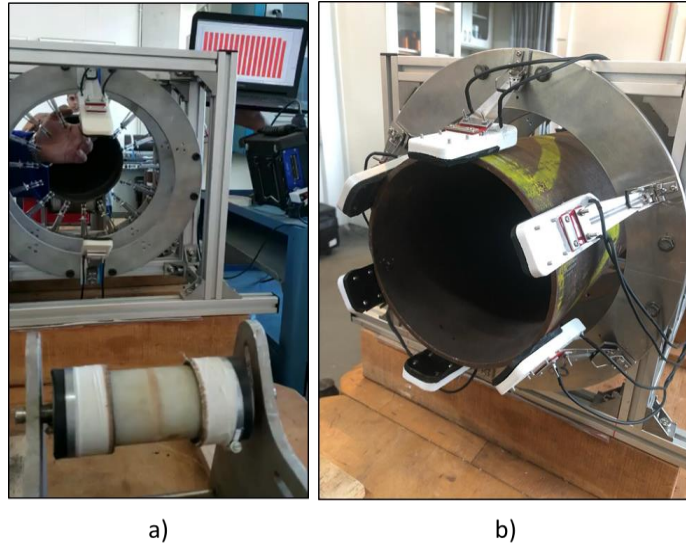
Figure 5. 30: In a) the dynamics of the tests related to the geometric sensors can be observed and in b) the dynamics of the tests related to the EC probes.

Figure 5.31 shows the profiling of one geometric sensor along a sample that had 3 different defects, the first one being a material adhesion, signaled by the green arrows, and two defects simulating material loss, signaled by the red arrows. The positive response of the signals to the areas representing the green arrow is easily observed, showing the adhesion of material in the response signal exposed in the lower part of the Figure, as well as the opposite for defect 4 representative of a loss of material.
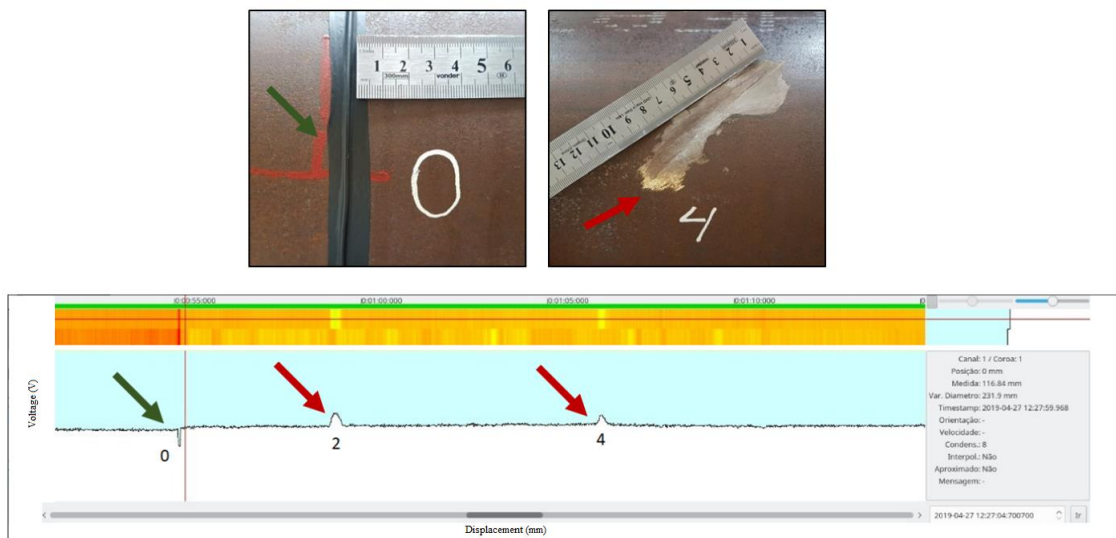
Figure 5. 31: Tests representative of the responses of geometric sensors in relation to profiling of an area with adhesion defects or loss of material.

Figure 5.32 shows representatively the results of the EC probe for the inspection of one defect in the transversal direction and another in the longitudinal direction by the built prototype. It is possible to observe both the detection response in the signals shown by the green arrows and their respective reconstructions in an impedance map signaled by the red arrows. After the laboratory tests, the system was packed and transported for the production line test.
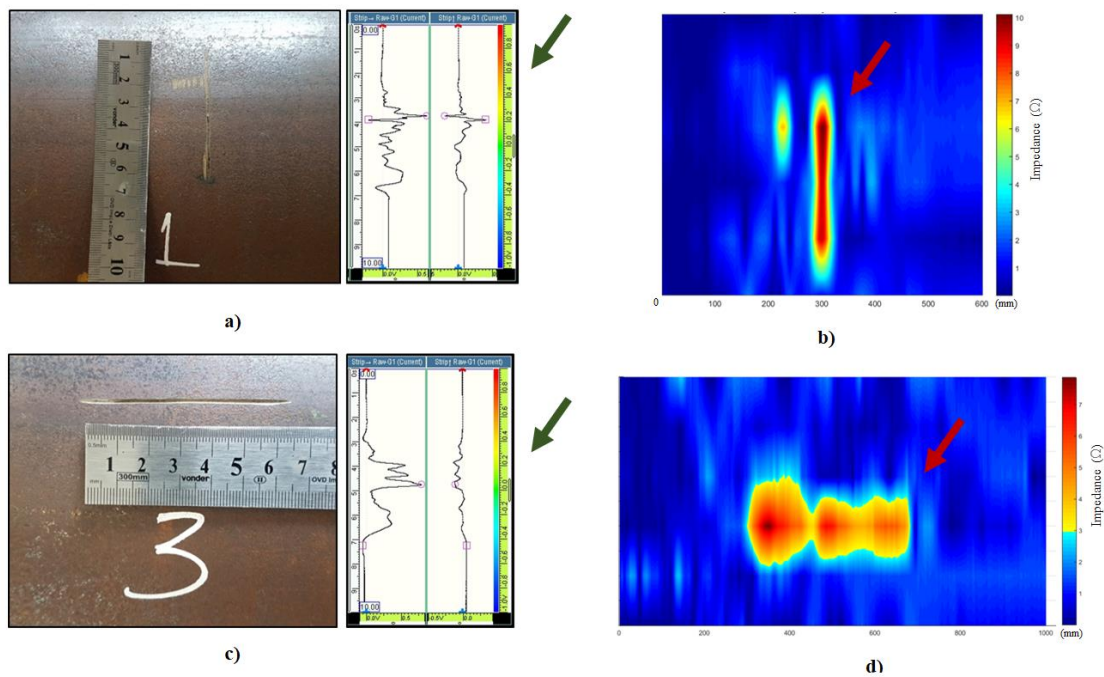
Figure 5. 32: Tests representative of EC probe responses regarding inspection of small defects in transversal and longitudinal directions.

Prototype test in production line – Mandrel Mill

After the construction and testing of the electromagnetic prototype in the laboratory, the system was taken to the production line of the Vallourec's mandrel mill to perform tests on the production line based on the worst boundary conditions of the production process, i.e., 22 m long mandrels, 2.0 m/s mandrel speed, grease dirty mandrels and uninterrupted cycle. Seven mandrels were used for the tests, being the first called mandrel I with Ø 163.00 mm diameter containing several defects, as can be seen in Figure 5.33, a second called mandrel II with Ø 165.50 mm containing a transversal defect along its entire diameter, as can be seen in Figure 5.34, and finally, 5

mandrels called mandrel III-VII with Ø 165.50 mm containing no defects. A tape was placed on the mandrel I along its circumference to be used as a reference for the analysis of the results, as can be seen in the upper left corner of Figure 5.33.

Figure 5. 33: Example of 11 different defects contained in the mandrel I.

Figure 5. 34: Single transversal defect contained along the circumference of mandrel II.

Figure 5.35 shows in a) the front view of the system installed on the production line where it can be observed that the EC probes cover a hundred percent of the

mandrel's surface, in b) it is possible to observe that the system was installed before the mandrel's and in c) exemplary shows the movement of one mandrel's through the inspection system.
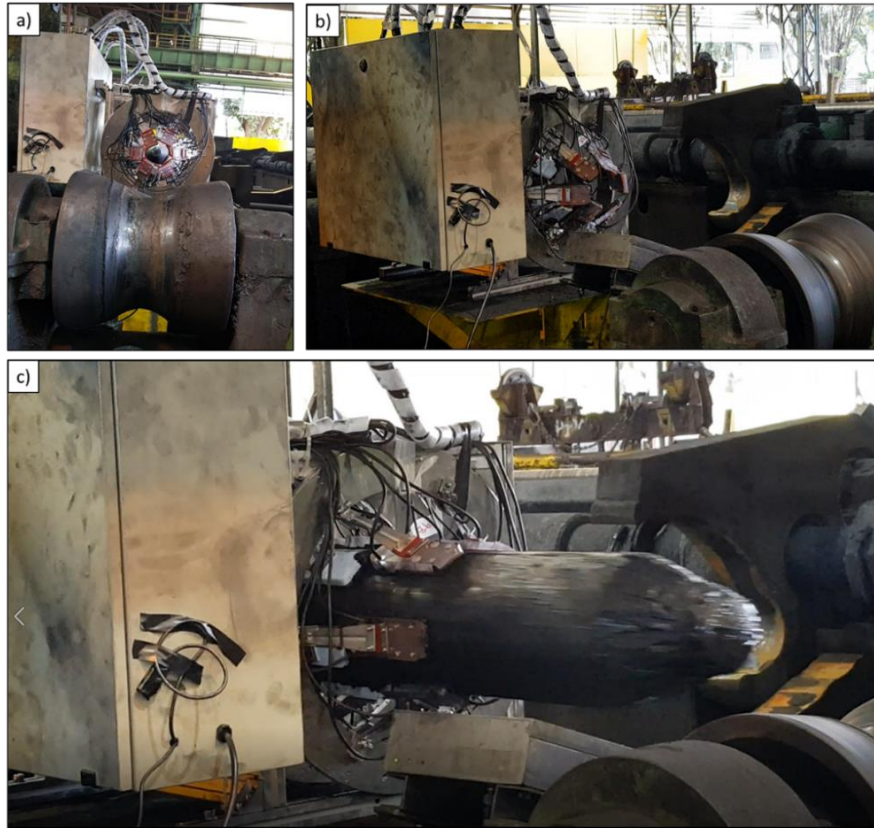
Figure 5. 35: In a) the front view of the system installed on the production line, in b) it is possible to observe the installation point of the system on the production line and in c) it is exemplary the movement of the mandrels through the inspection system.

Geometric sensor results

The results of the inspection by the geometric sensors will be shown representatively for the mandrel I detecting the defect 11 from Figure 5.36 and the diameter measurements performed for all the inspected mandrels will be presented. Figure 5.36 shows the result of one of the geometric sensors along the 22 m of the mandrel profile, where in the signal responses the detection of some indications can already be seen. The great indication right at the beginning of the inspection, left hand side of Figure 5.36 is due to a tape glued around the entire mandrel to be used as a reference point.
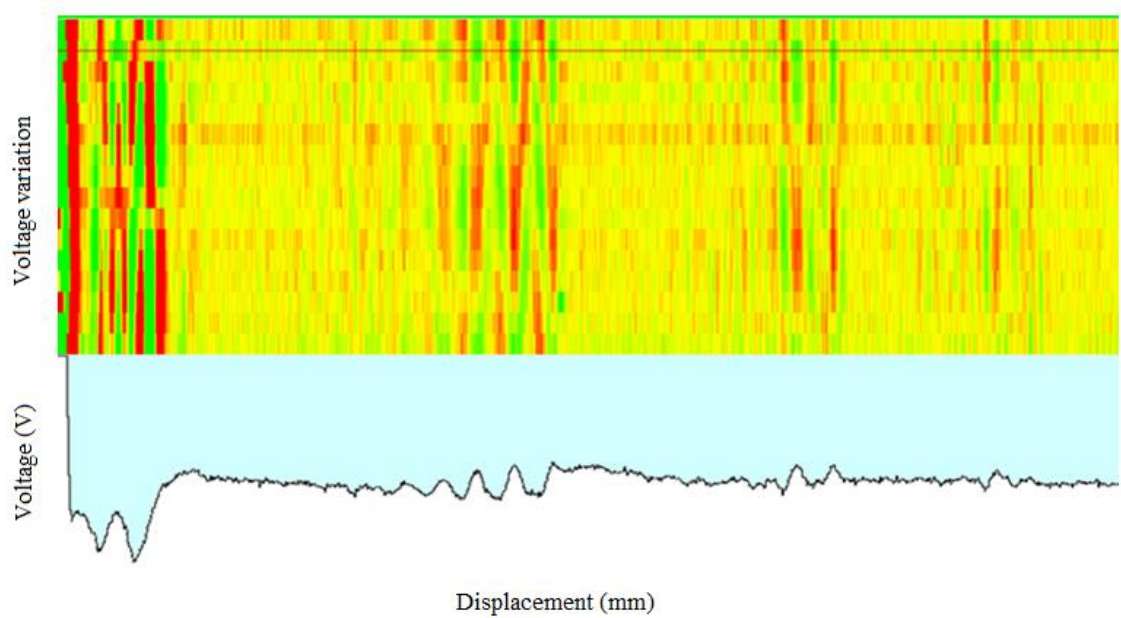
Figure 5. 36: Signal responses for a geometric sensor during mandrel I inspection.

Figure 5.37 shows in detail a region of the indication where the 11th mandrel I defect is located. It shows the "zoom" of the inspected region, where it can be observed the indication in green on the image enlarged to the right and perform the quantification of the defect depth that was 2.5 ± 0.1mm.
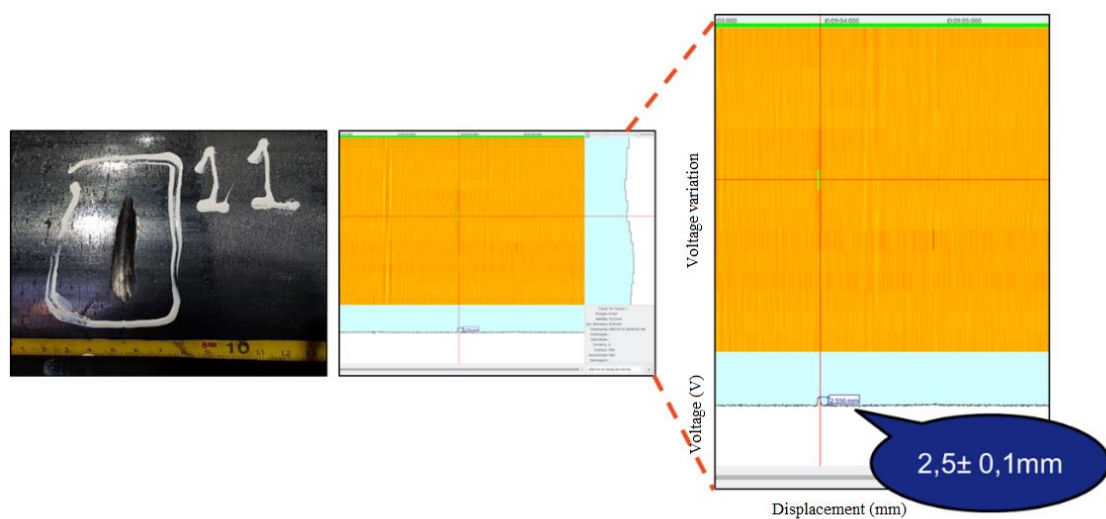
Figure 5. 37: Detection and depth quantification mandrel I 11th defect by geometric sensors.

Figure 5.38 shows in detail an indication region for the mandrel II where its only defect is located along its circumference. In this Figure, the indentation in green can be seen in the enlarged image to the right and the quantification of the defect depth which was 2.1 ± 0.1mm.
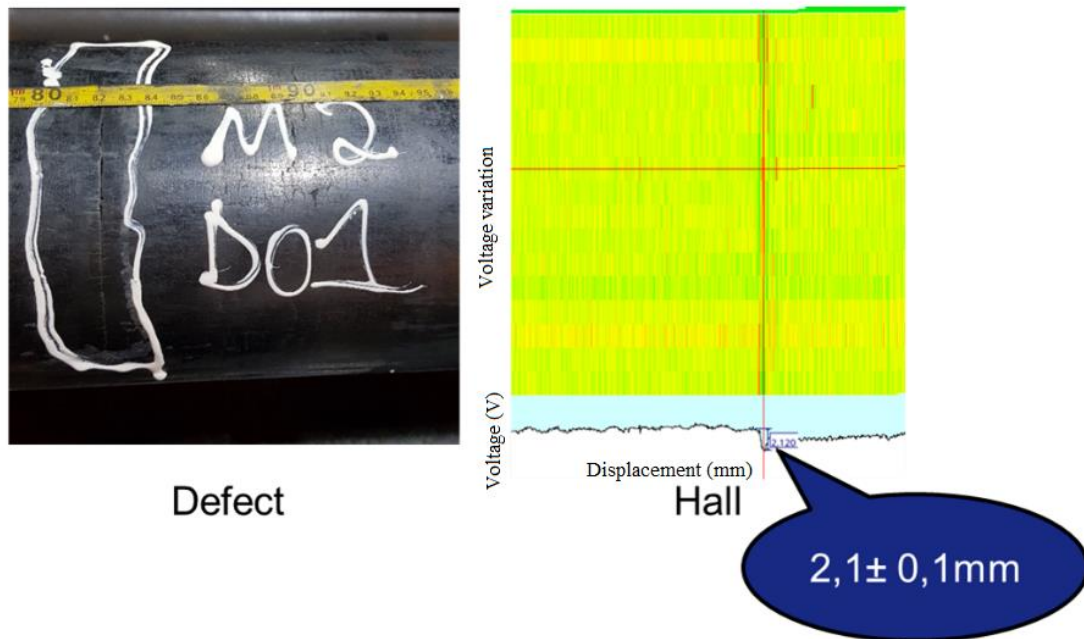
Figure 5. 38: Detection and depth quantification mandrel II only defect by geometric sensors.

Figure 5.39 a) shows the diameter analysis made through the data collected by the geometric sensors and in b) the results of the measurement of the inspected mandrels' diameters are summarized representatively. The system presented measurements with accuracies lower than 2.0 mm. This precision could, theoretically, reach about 0.1 mm, either by calibrating the sensors or by increasing their number.

OD Measurement	
Mandrel I (Ø163,00mm)	Ø(161,94 ± 1,72)mm
Mandrel II (Ø165,50mm)	Ø(164,27 ± 1,38)mm
Mandrel III (Ø165,50mm)	Ø(163,62 ± 1,46)mm
Mandrel IV (Ø165,50mm)	Ø(164,88 ± 1,12)mm

a)   b)
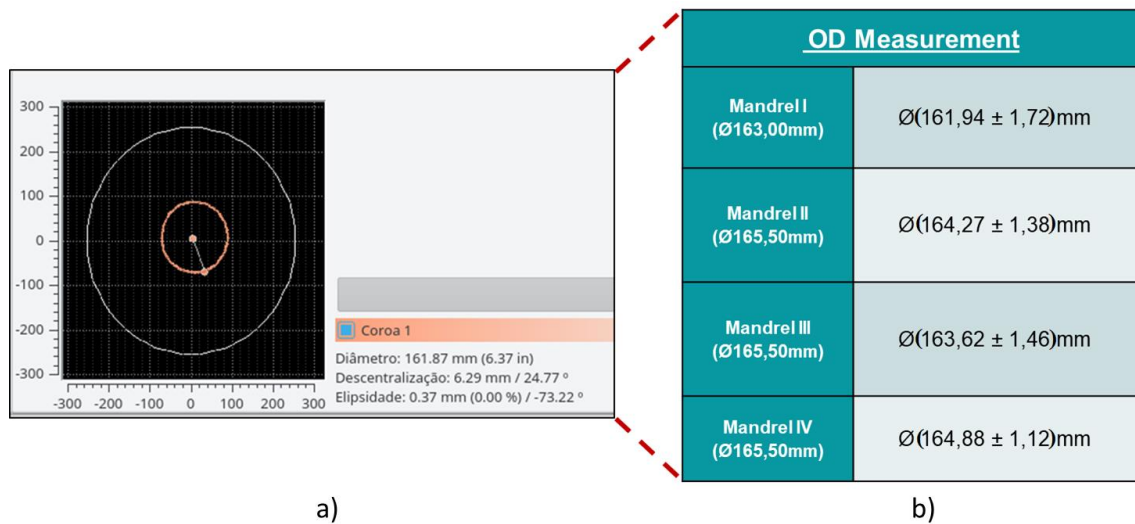
Figure 5. 39: In (a) diameter measurement of mandrels by geometric sensors and in (b) representative summary of the achieved diameter measurements.

Eddy current results

EC probe inspection results are shown representatively both in their detection signals and for the impedance response inspection map. Figure 5.40 shows the result of one of the EC probes along the 22 m of mandrel profile, where in the signal responses the detection of some indications can already be seen. The great indication right at the beginning of the inspection, on the left-hand side of Figure 5.40, is due to the tape glued around the entire mandrel circumference segment to be used as a reference.
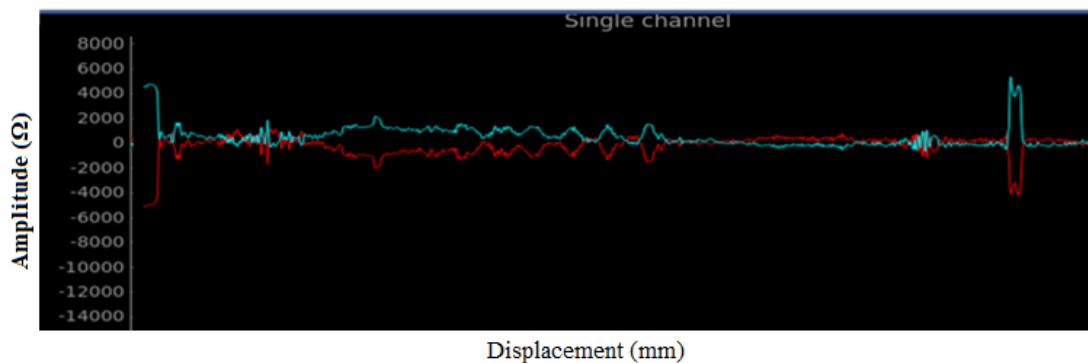
Figure 5. 40: Signal responses for an EC probe throughout mandrel I inspection.

Figure 5.41 shows the map in impedance for the inspection performed along the 22 meters in the mandrel I, larger number of defects, and it is possible to notice areas

123

with indications in red/orange. Figure 5.42 shows the detection of the reference tape glued to the mandrel I. Still in Figure 5.41 it is possible to notice that there are regions with higher indication concentrations in the initial region of the mandrel. By analyzing details of the areas inspected in this map, it is possible to see the response both on a map and on the signals of the EC for defect detection as shown in Figures 5.43, 5.44 and 5.45.
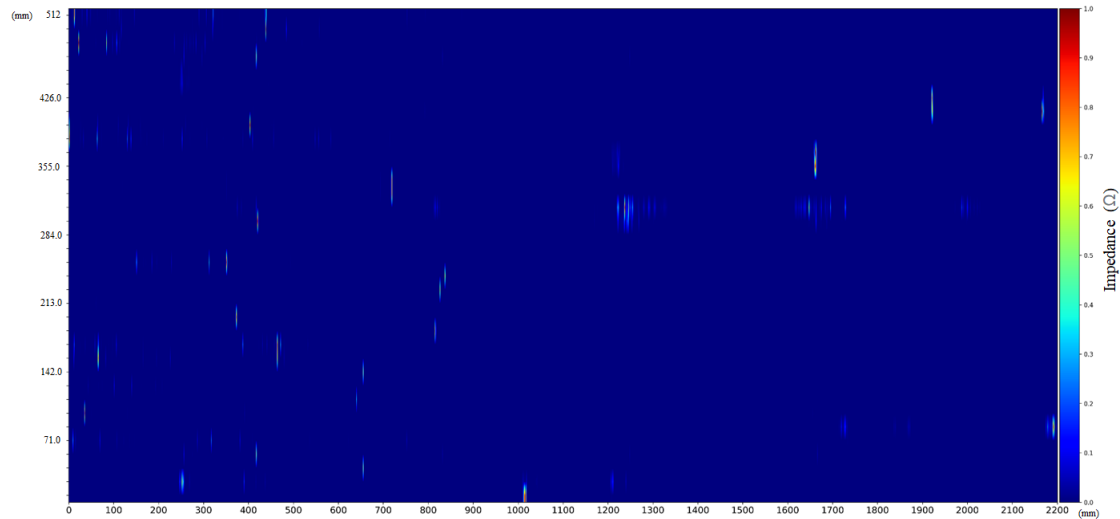
Figure 5. 41: Impedance map of EC inspection for mandrel I.

Figure 5. 42: Detection of the reference tape by the EC probes along the entire circumference of the mandrel I.

Figure 5.43 shows the detection of mandrel I defect 1 in both the impedance map and the resistance signals, inductive reactance and impedance plane. It is possible to clearly identify the quality of the signal-to-noise ratio in the defect detection, as well as the characteristic Figure in the impedance plane, lissajou figure, which distinguishes the detection of defects by EC probes operated in differential mode. These signals are representative of the signals detected also for defects 2 and 8 of the mandrel which are presented in Figures 5.44 and 5.45. These defects represent the different variety of defects present in the mandrel I.
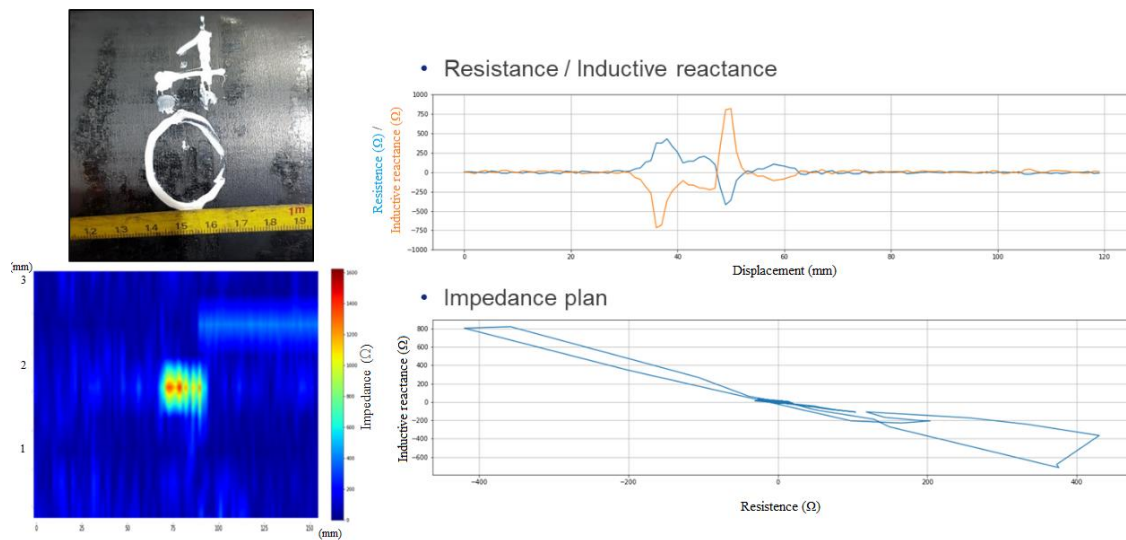
Figure 5. 43: Detection of the defect 1 (smooth loss of material) in mandrel I by EC probe.
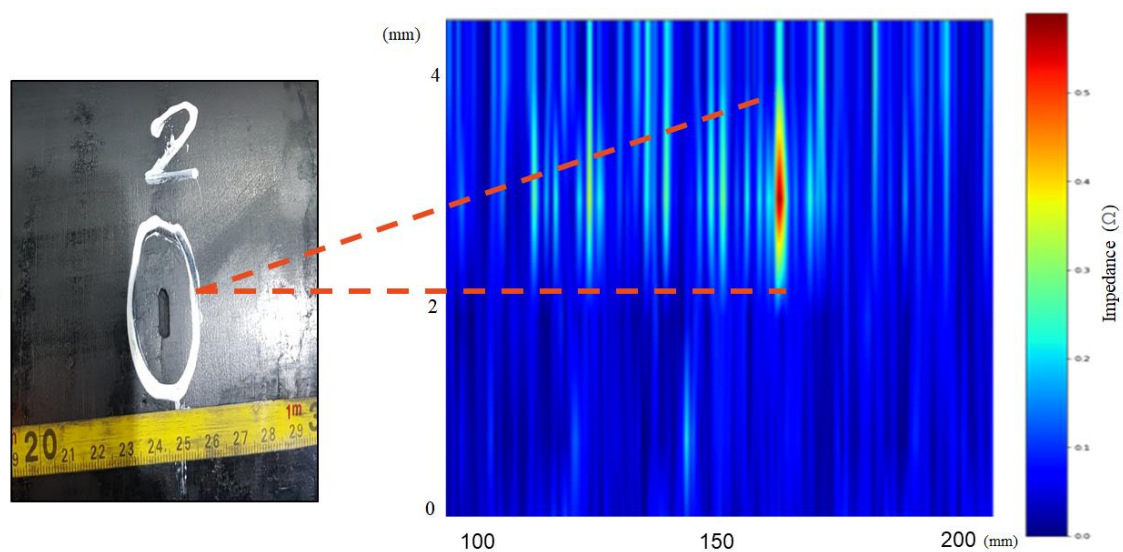
Figure 5. 44: Detection of the defect 2 (loss of material) in mandrel I by EC probe.
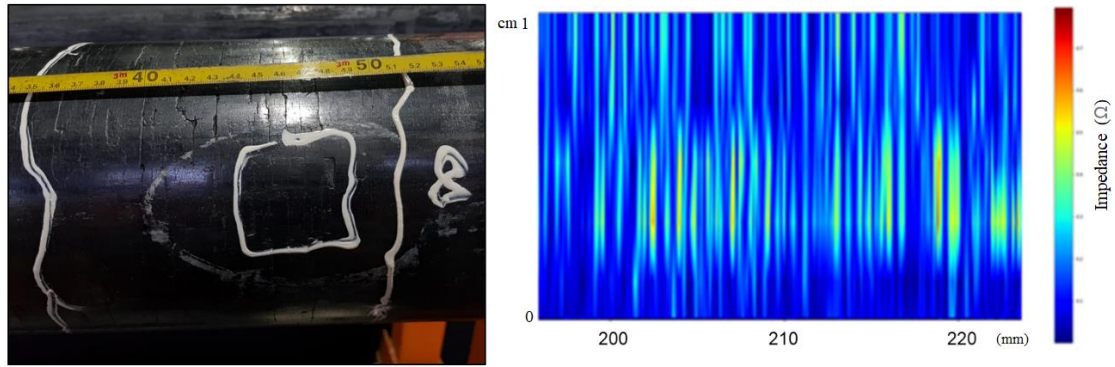
Figure 5. 45: Detection of the defect 8 (several cracks) in mandrel I by EC probe.

The same inspection and data analysis procedure was carried out for mandrel 2 which had only a transversal crack that surrounded the entire surface of this mandrel. Figure 5.46 shows the detection of this defect for the impedance map as well as for the resistance component, inductive reactance and in the impedance, plane forming again the lissajou.
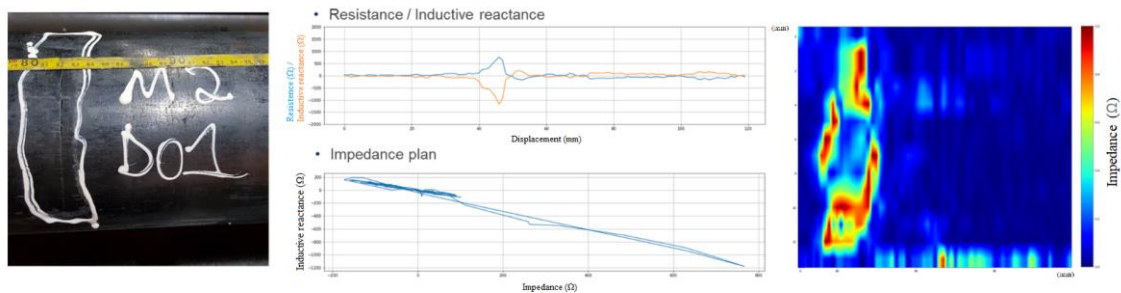
Figure 5. 46: Detection of the circumferential crack in mandrel II by EC probe.

Figure 5.47 shows mandrel III inspection results, which is representative of the results found for the mandrels that did not have any defects. As expected, there are no relevant indications in the impedance map and the signal analysis does not show also any relevant information. The results presented throughout this section are representative of the results found after 77 inspection of the 7 mandrels (11 inspections each one) present for the tests.

126
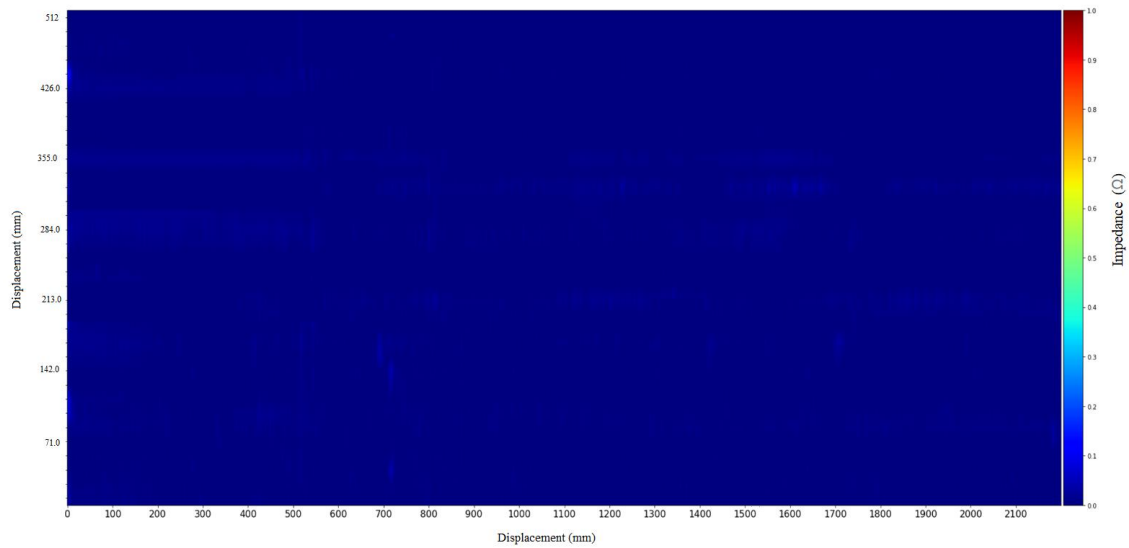
Figure 5. 47: Mandrel III impedance map.

As well as for the results of the optical technique, based on the presented results, it is possible to state that the electromagnetic inspection methodology developed has results extremely positive for the surface defect detection, still proven in an industrial environment. Comparing with the optical methodology, the electromagnetic methodology has the subsurface detection capability and significantly lower data volume due to its lower acquisition rate. However, the geometric fidelity and lateral resolution of the results obtained by the LL are much higher than that compared to the electromagnetic system. Thus, it is perceived that the two different methodologies are not competitive with each other, but complementary, in order to ensure that they cover any type of surface defects. The decision to use one of the methodologies or the simultaneity of the two will be purely based on the necessity and contouring conditions of the final application.

Again, it is important to emphasize the importance of an algorithm able to handle analysis of data generated by different techniques and based on the same evaluation methodology aiming the automatization of the defects recognition and characterization.

5.4. Development and validation of defect recognition and characterization algorithm

This topic described each step of the development of the algorithm to recognize and classify defects based on different data sets. The automatic recognition algorithm will be detailed, showing how each processing step is indispensable. The algorithm applied to the data processing is summarized in Figure 5.48. It is divided in four steps, each one with sub-steps: Import data, pre-processing and the processing itself. These are the necessary steps to prepare the data to the classification routine.
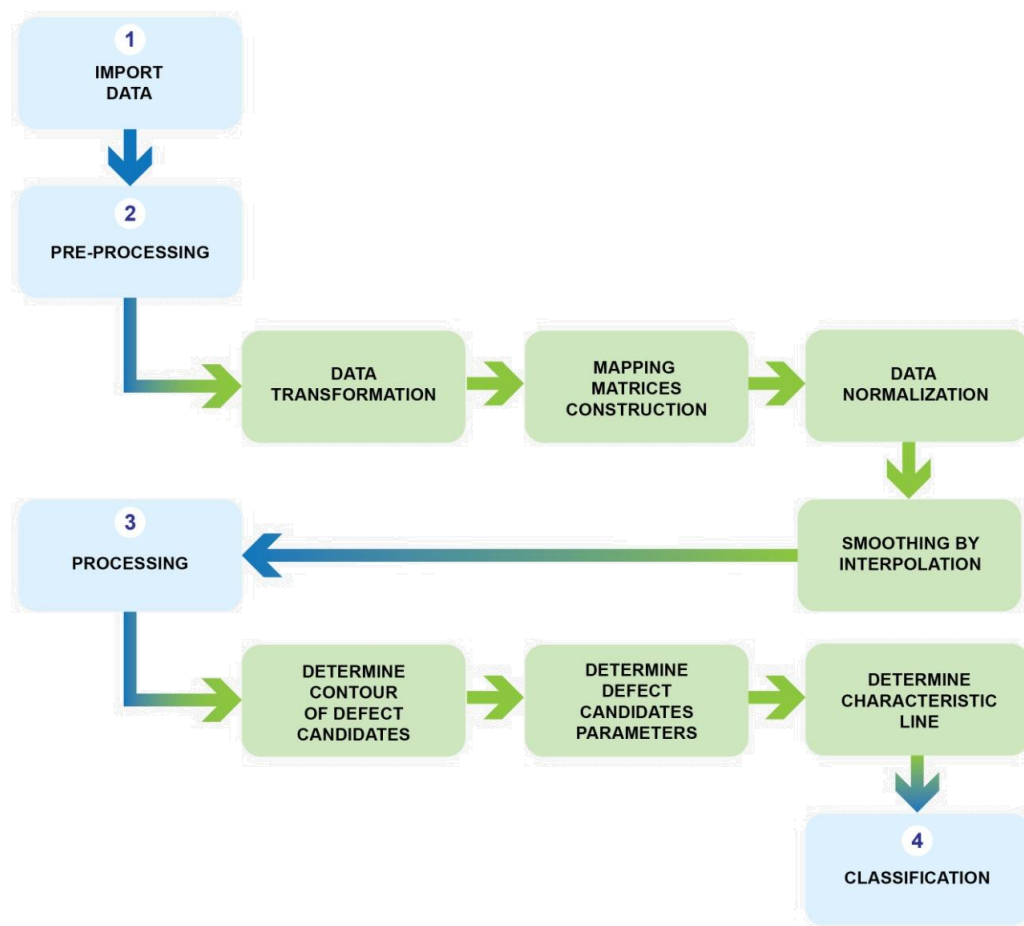
Figure 5. 48: Stages of the data processing algorithm developed in this work.

5.4.1. Data import and pre-processing

Data from the electromagnetic system will be used to show the development of algorithms in this subsection.

a) Data import

The algorithm begins after all the data acquisition from the inspection system is done, starting the pre-processing step. The goal of this stage is to process the data in order to prepare it for the application of classification algorithms, which was responsible for the defects classification into the categories to be further defined. The data can be received from different sensors, as EC sensors, Hall sensors and optical 3D sensors.

EC sensors

The data received from EC sensors is basically structured in a two columns matrix for each probe connected to the inspection system. The two columns are, respectively, the values of resistance and inductive reactance of the coils. The first line of each matrix corresponds to the point where the sensors started to inspect the sample, and the last corresponds to the point where the sensors stopped, following the line in the sample surface. For example, if the system has 18 probes connected to it, each one will generate a two columns matrix of data associated to the points in the line inspected for each probe. To transform this set of matrices in one single map, the data must be transformed through mathematical operations that will be explored in the next subsections.

Hall sensors

Similarly, to the EC the data received from the Hall sensors is structured in one matrix for each probe, where the first and last point corresponds to the first and last acquisition point. But, in other hand, they have only one column, that is already directly associated to the "height" of the measured point in relation to the sample base line, since the sensor is profilometer. Therefore, this data is all ready to be mounted in one single matrix, which will be used to build a map that reconstructs the sample surface.

Optical 3D sensors

The optical 3D data from structured light and laser systems have the same format of data, being structured in one matrix where X, Y and Z coordinates of each measure points are the columns and the lines are each one of the measured points. These maps are the starting point for the defect detection algorithms in the processing step. All the operations necessary to build these maps from the imported data define what is called pre-processing step.

b) Preprocessing

EC data transformation (impedance calculation)

Besides the EC sensors directly measure only R and the XL, they are not the parameter that effectively represents the variation of height in the sample surface, which is the necessary information for the surface reconstruction. This parameter, which is the actual parameter of interest, is the coil impedance (Z). To calculate this value, it is necessary to perform a transformation of the data for each measured point following the Equation 5.1.

$$Z = \sqrt{R^2 + X_L{}^2}$$
Equation 5. 1

After this transformation, the two columns matrices associated to each probe, or, in other words, to each generatrix line in the sample surface upon which the probe has passed, are converted in one column matrices. Along with the hall sensor matrices, this data is all ready to be mounted in a single matrix.

Mapping matrices construction

After the first pre-processing step, it is necessary to unify all one column matrices associated to each probe in one single matrix. This will generate two maps of points that represent the reconstruction of the surface by the EC data and Hall sensor data.

To construct the EC map, for example, it is only necessary to mount a single matrix with each column equal as each one column matrix associated to each probe, ordered in the same sequence that the probes are installed in the equipment. The

procedure is equivalent for the Hall sensor data. After the matrix is constructed, they can be plotted by color mapping, as can be seen in Figure 5.49.
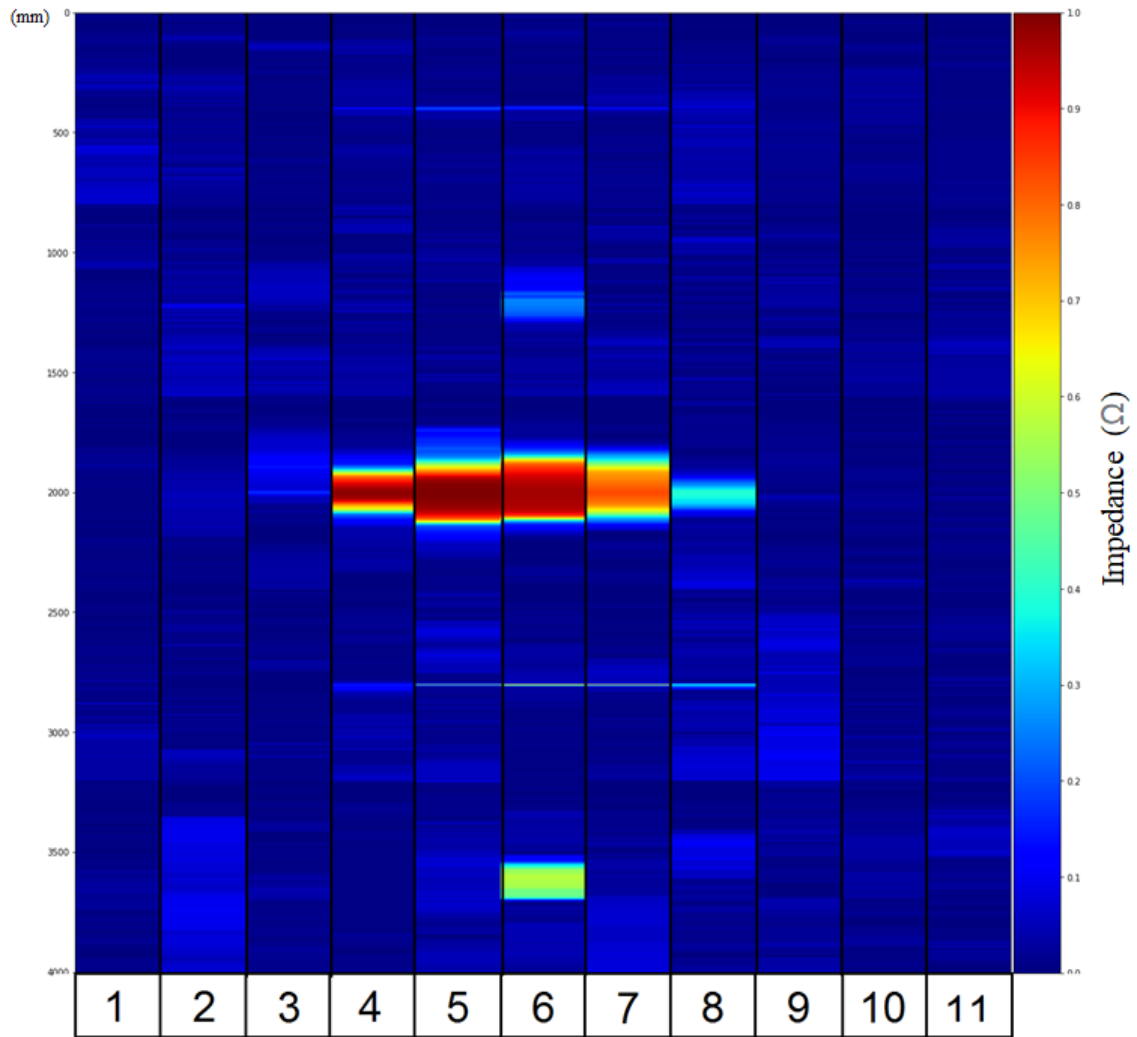
Figure 5. 49: Map of EC impedance from PP sample. Each column numbered from 1 to 11 is the data associated to each probe.

Data normalization

After the set of matrices for each kind of probe are converted in single matrices, each one of them is normalized to guarantee that the data will all belong to the same interval. The limits are chosen as a = 0 and b = 1 so all the points will belong to the [0, 1] interval.

Smoothing by bilinear interpolation

As can be seen in Figure 5.49 furthermore the plotted maps already represent the reconstruction of the measured tubular surface, they are still visually truncated and discontinuous. To improve them, a smoothing technique by interpolation can be applied. In mathematics, bilinear interpolation is an extension of linear interpolation for interpolating functions of two variables (e.g., x and y) on a rectilinear 2D grid.

Bilinear interpolation considers the closest 2x2 neighborhood of known pixel values surrounding the unknown pixel. It then takes a weighted average of these 4 pixels to arrive at its final interpolated value. In the analyzed case, the image is not composed exactly by pixels, but by one value associated to each point in the bidimensional space, the sample surface, what is analogous. The key idea is to perform linear interpolation first in one direction, and then again in the other direction. Although each step is linear in the sampled values and in the position, the interpolation is not linear but rather quadratic in the sample location. Equation 5.2 describes the process of bilinear interpolation (PRESS, TEUKOLSKY *et al.*, 1992).

$$f(x, y) = \sum_{i=0}^{n} \sum_{j=0}^{n} a_{ij} x^i y^j \qquad \text{Equation 5. 2}$$

Applying the bilinear interpolation to the case dataset, it is possible to receive a much smoother looking image, what is a main requirement for the success of the processing algorithms. It can be seen in Figure 5.50, for example, that the limits of the inhomogeneous areas are much more evident. Once the data is pre-processed and smoothed, processing for feature extraction can be started.
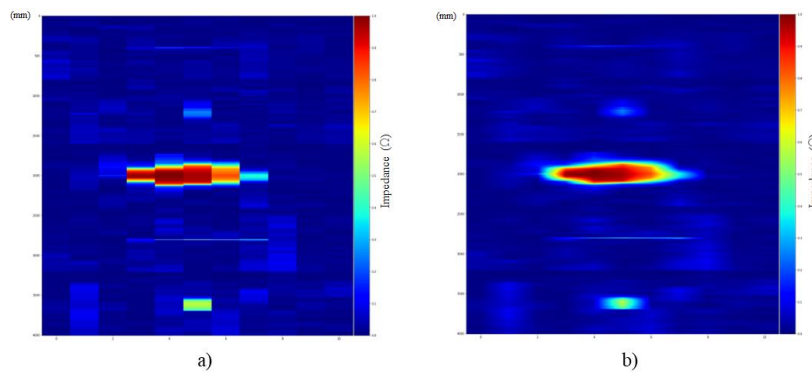
Figure 5. 50: EC impedance map of PP sample without interpolation a) and after bilinear interpolation b).

c) Processing – Features extraction

Through the processing step can be obtained the necessary features for classifying the defects in the further steps. In this work, it is proposed to extract the following features: dx = Maximum dimension in x; A = Area; dy = Maximum dimension in y; h = Maximum depth; P = Perimeter; CV = Characteristic curve and N = Number of closed contours in the image. For this, the following steps are necessary:

Determine the contour of defect candidates

To calculate the contours of defects candidates, the "marching squares" (MS) algorithm was applied. According to chapter 2.3.1, to find the MS reference value N in the detection of the contours, i.e., the minimum intensity value to consider a point as part of a defect area, it has been considered that the statistical distribution of both EC and Hall data is normal. Therefore, after several tests N has been defined as 1.7 times the standard deviation for data from the Hall sensor and 0.7 times the standard deviation for EC data. In this approach, the defects are considered statistical outliers of the data distributions. The results of the contouring process for the inspections performed for sample PP thought EC can be seen in Figure 5.51. It is possible to observe that the developed algorithm recognizes the defects automatically and contours each one of them through the adapted algorithm of MS.
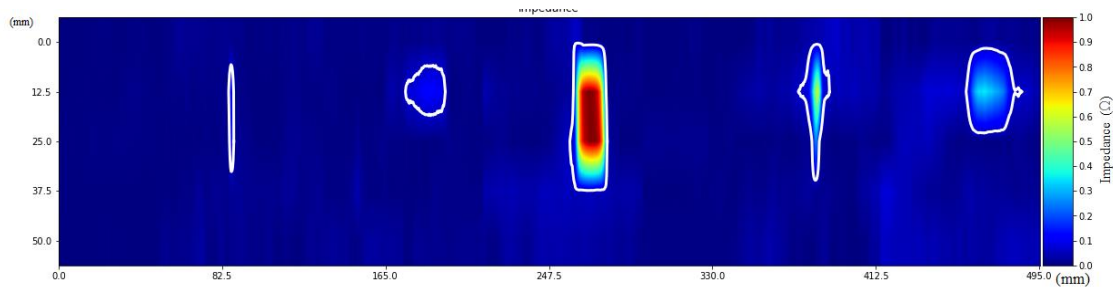
Figure 5. 51: 2D impedance of sample PP inspection using coil 5 with optimized frequency of 5 kHz.

Extracting features of the recognized defects

Table 5.11 shows the extraction proceedings to extract features of each area determined by the contour.

Table 5. 11: Definition of the main parameters to be extracted from the contoured region.

Perimeter

Defined as the length of the isoline associated to the defect candidate. Measured directly as the number of points in each isoline.
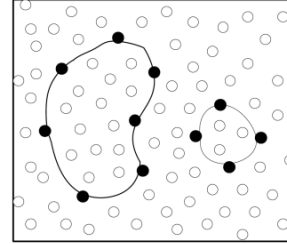
Dimensions in x/y

Defined as the distance between the two farthest points inside the contour in the x or y axis directions.
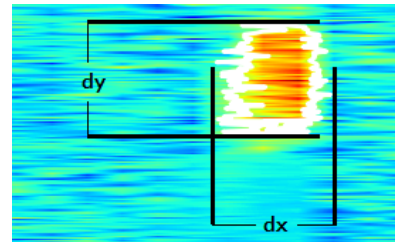
Minimum/maximum values

Defined as the points with minimum and maximum values in the contour intern area.
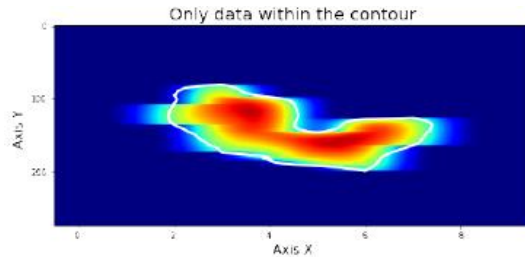
Area

Defined as the area inside the isoline associated to the defect candidate. Measured through the Shoelace equation, considering a polygon P with vertices (x_i, y_i):

$$A = \frac{1}{2} \left| \sum_{i=1}^{N} x_i y_{i+1} - x_{i+1} y_i \right|$$

Equation 4. 3
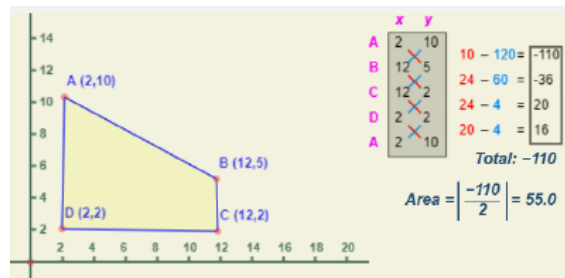
After these extracted parameters have been calculate, another important feature defined to characterize the defects candidates is a central line that traverses the centroid of the contoured regions called Characteristic Curve (CV). These lines are calculated through an algorithm that combines two techniques, the Voronoi tessellation and graphs analysis. The theoretical basis of these two methods were described in (Okabe *et al.*, 2009) and (Gross *et al.*, 2013), and its can be summarized as follow.

Voronoi Diagram is a special type of decomposition of a given space, in the case of this work the contoured region, determined by the distance to a given family of objects in space. These objects are usually called sites or generators. Each site is associated with a corresponding Voronoi cell, i.e. a set of all points in the given space which the distance to the given site is no greater than its distance from the other objects. In other words, it parameterizes the entire interior of the surrounded region, subdividing a plan in regions close to certain important or special points with which the diagrams are created. Already with the inner region of the contour detailed, through the adapted graph algorithm several lines are drawn that connect the edges of the contour perpendicular to their greater orientation between "dx" and "dy". The central point of each of these lines is interconnected and, in this way, the characteristic curve is obtained.

After obtaining the Voronoi diagram through the tessellation, all lines outside the defect are retained so that the central line can be found, and then converted to a graph. This is made to guarantee that the best way to link the initial and final vertices can be found. Figure 5.52 shows the contours and the characteristic curve extracted from the inspection impedance map of sample PP, described on Table 4.1, by coil 5 with a frequency of 5 kHz.
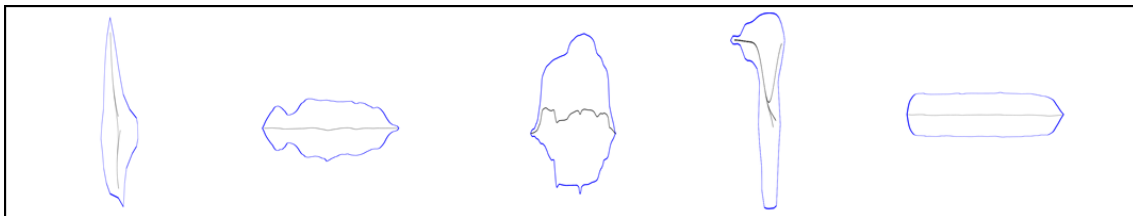
Figure 5. 52: Extraction of the contours (in blues) and characteristic curve (in black) of the PP sample using MS adapted algorithms for the contours and Voronoi adapted algorithms for the characteristic curve.

d) Defects classification

Once all the necessary parameters have been extracted from the defects, the procedure for classifying the defects is started. After extensive tests and studies related to the defect catalogues of pipe mills, a classification methodology divided into three stages is being proposed, which are the defect orientation, defect morphology and defect depth. An illustration can be seen in Figure 5.53 and the subsequent items will show details of the developed classification algorithm.
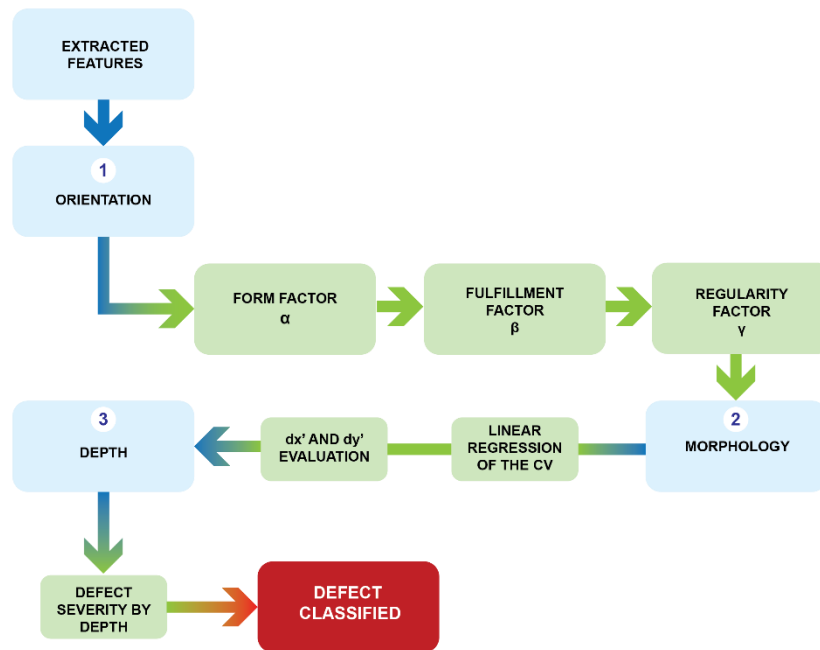
Figure 5. 53: Illustration of the steps for defect classification.

i. Orientation
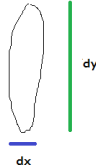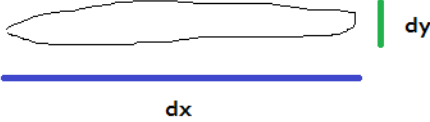
Based on the defect catalogues of the pipe mill, the defect orientation can be divided into longitudinal, transversal, oblique, circular, irregular and complex, as described in Figure 4.14 of chapter 4.5.2. To separate each of these defect orientations, 3 non-dimensional factors are proposed, being the form factor α, fulfillment factor β and the regularity factor γ. The threshold values for each of these factors were defined based on experience.

The form factor α compares the maximum defect size in x and y, being its objective to distinguish between the transversal and longitudinal orientations. However,

form factor α does not distinguish the circular, oblique, irregular and complex orientations. The form factor α is determined Equation 5.4 and Table 5.12 shows the values of the form factor α for the distinction of the transversal and longitudinal orientations determined so far, as well as schematic illustrations of the defects.

$$\alpha = \frac{dx}{dx+dy}$$

Equation 5. 4

Table 5. 12: Classification based on form factor α.

α condition	Classification
α < 0.3	Transversal
α > 0.7	Longitudinal
0.3 ≥ α ≤ 0.7	Oblique, circular, irregular or complex

The fulfillment factor β compares the area of the defect with the area of a circumscribed circle whose diameter is the maximum size of the defect, being applied to distinguish the circular defects of the others. However, fulfillment factor β does not distinguish oblique, irregular and complex defects. The fulfillment factor β is determined by Equation 5.5 and Table 5.13 shows the values of the fulfillment factor β for the classification of the irregular and oblique orientation determined so far, as well as schematic illustrations of the defects.

$$\beta = \frac{A}{\pi*\left(\frac{max(dx,dy)}{2}\right)^2}$$

Equation 5. 5

137
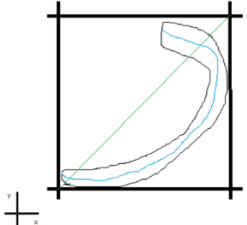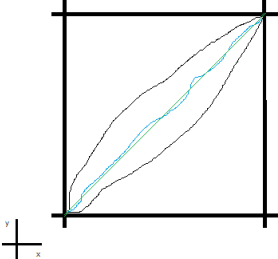
Table 5. 13: Classification based on fulfilment factor β.

β condition	Classification
	Circular
β > 0.6	
	Oblique, irregular or complex
β < 0.6	

The regularity factor γ Compares the diagonal of a rectangle circumscribed to the defect oriented with the X and Y axes to the length of the central curve of the defect, being applied to distinguish irregular and oblique defects to the others. However, regularity factor γ does not distinguish complex defects. The regularity factor γ is determined by Equation 5.6 and Table 5.14 shows the values of the regularity factor γ for the classification of the circular orientation determined so far, as well as schematic illustrations of the defects.
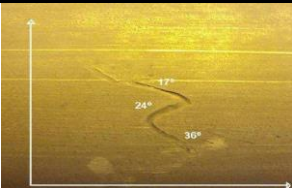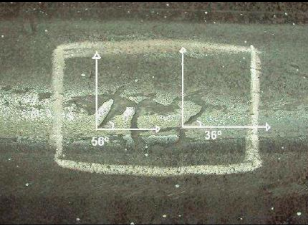
$$\gamma = \frac{\sqrt{dx^2 + dy^2}}{\sqrt{dx^2 + dy^2} + length(CV)}$$ Equation 5. 6

Table 5. 14: the values of the regularity factor γ for the classification of the circular orientation.

γ condition	Classification
	Irregular
γ < 0.3	
	Oblique
γ > 0.3	

Using the form factor α, fulfilment factor β and the regularity factor γ it is possible to distinguish between the directions of longitudinal, transversal, circular, irregular and oblique defects. Consequently, it is also possible to distinguish complex defects by exclusion. Table 5.15 summarizes the rules developed so far for the classification of defects.

Table 5. 15: Summary of factors for classifying defects in terms of their orientation.

Orientation	Example	Condition: Determinant metrics / Non-determining metrics
Longitudinal		if $\alpha > 0.7$ defect = Longitudinal
Transversal		if $\alpha < 0.3$ defect = Transversal
Circulars		if $0.3 \geq \alpha \leq 0.7$ if $\beta > 0.6$ defect = Circular
Oblique		if $0.3 \geq \alpha \leq 0.7$ if $\beta < 0.6$ if $\gamma > 0.3$ defect = Oblique
Irregular		if $0.3 \geq \alpha \leq 0.7$ if $\beta < 0.6$ if $\gamma < 0.3$ defect = Irregular
Complex		else

ii. Morphology

Also based on the defect catalogues of the pipe mill, the defect morphology can be divided into cracks, dents, scratch and extended scratch as described in chapter 4. To separate each of these defect morphology two rules were stablished the first being for the cases where the defects have transversal, longitudinal or oblique orientations a

sequence of dimensional comparisons should be performed. Follow below the sequence to be performed and Figure 5.54 a) shows an illustration of the linear regression and in Figure 5.54 b) shows the parameters dx' and dy' to be calculated in the axis orientation according to the linear regression of the CV.
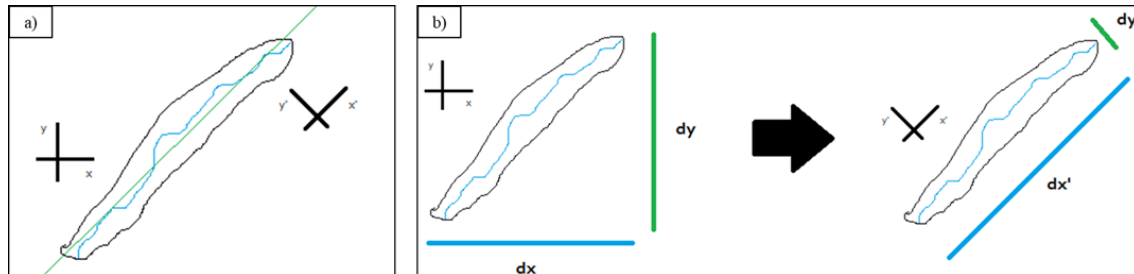
Figure 5. 54: a) illustration of the linear regression; b) shows the parameters dx' and dy' to be calculated in the axis orientation according to the linear regression of the CV.

If defect = transversal, longitudinal or oblique, follow:

- Linear regression of the CV ➔ axis x' of defect
- Calculate maximum axis dimensions x' and y' ➔ dx' and dy'
- If dx' > 200 mm ➔ **Extended scratch**
- If dy' < 3 mm ➔ **Crack**
- If 3 mm ≥ dy' ≤ 10 mm ➔ **Scratch**
- If dy' > 10 mm ➔ **General defect**

The second one is for the cases where the defects have circular orientation a comparison based on its depth should be performed, aiming the classification between dent and intense dent.

If defect = circular ➔ **Dent**

iii. Depth

The intensity of the test response is used as a relative measure of the defect depth, thus generating an estimation of the severity of the detected defect. Table 5.14 shows the indication of the severity of the classified defect.

141

Table 5. 16: Defect severity classification.

Depth	Severity
h < 6% Wall thickness	Green
6% ≥ h ≤ 10% Wall thickness	Yellow
h > 10% Wall thickness	Red

5.4.2. Validation of the developed algorithm

This subsection presents the validation of the developed algorithm based on the structured light measurements results of all defects on the several samples from section 4.1 As an example, the reconstruction by structured light of defect 4 of Pipe 01 is shown in Figure 5.55 a) and in Figure 5.55 b) is shown the result map together with the recognition of the defect (contour of the defect) made by the algorithm developed. In Figure 5.55 c) is shown only the region of contour together with the CV of defect 4. Figure 5.56 shows the developed algorithm representative result of some other defects. The Table 5.17 shows the nominal differences between the main values extracted by the software with the real defects values measured by SLS and Figure 5.57 a), b), c), d) and e) shows the bar diagram of respectively comparison of the SLS and the developed algorithm measurements of length, width, depth, perimeter and area.. Based on these, it is possible to see the similarity of the results towards the validation of the algorithm developed.
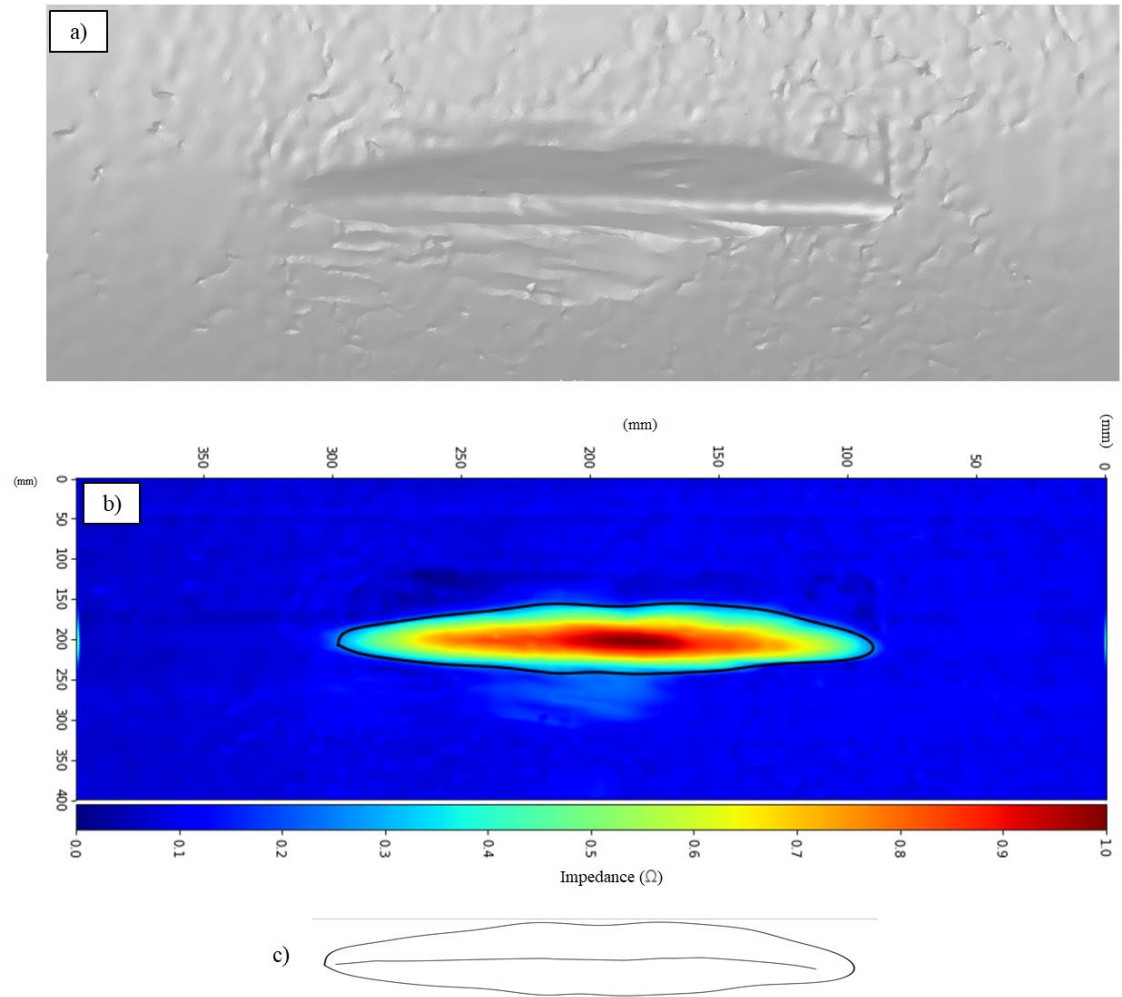
Figure 5. 55: a) Result for the structured light inspection of defect 4; b) the defect recognition map is shown together with its contour delimitation made by the developed algorithm; c) the contour and the defect's CV are shown.

a)   b)

c)   d)

e)   f)

g)   h)

i)   j)

k)   l)
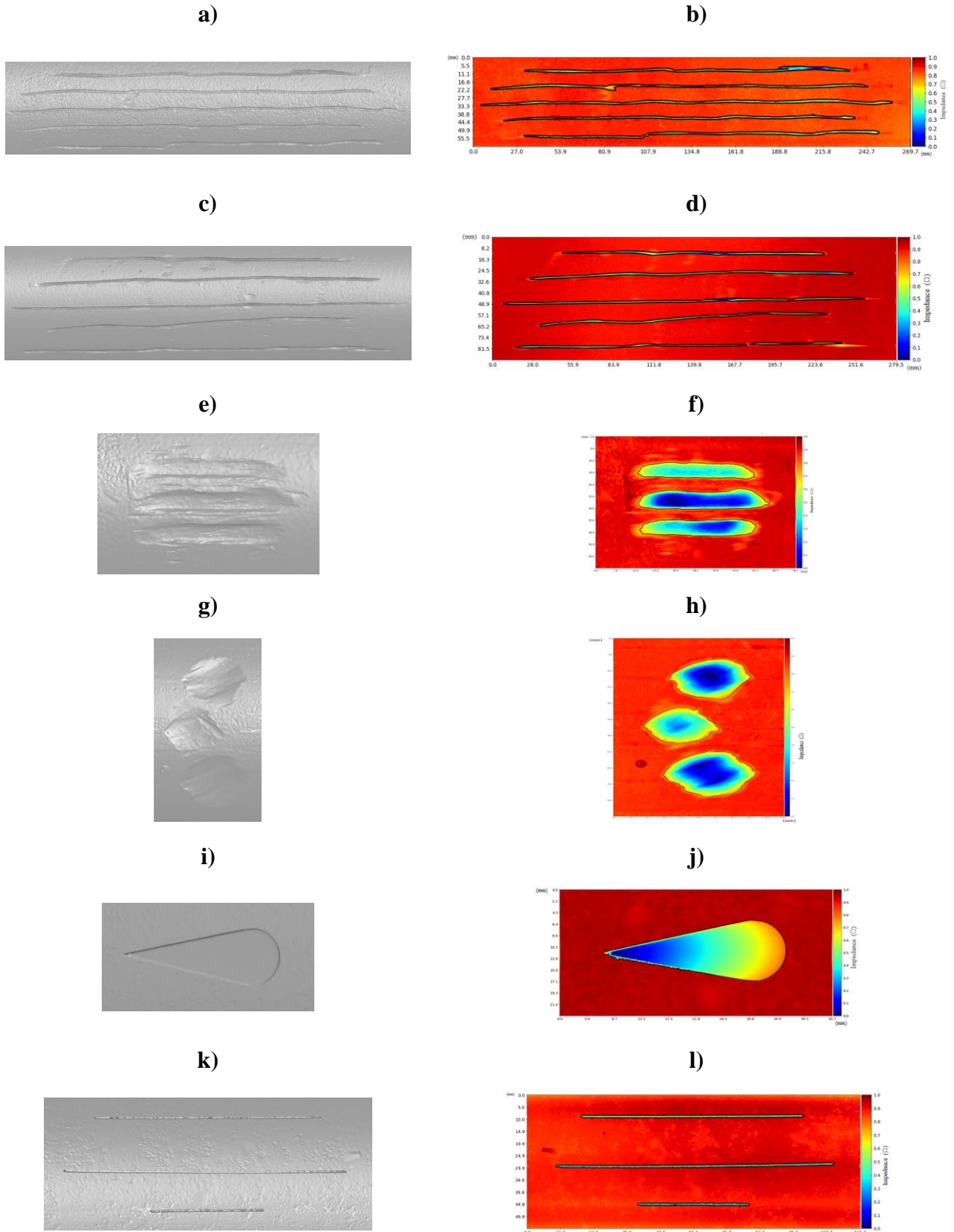
Figure 5. 56: Digital twin of defects by structured light respectively in a), c), e), g), i) and k) with their respective maps and contours made by the developed algorithm in b), d), f), h), j) and l).

144

Table 5. 17: Differences of measures between the SLS and the algorithm developed.

Defect	Length (mm)	Width (mm)	Depth (mm)	Perimiter (mm)	Area (mm²)
Defect 1	-0.54	-0.87	-0.02	-7.88	-16.07
Defect 2	0.01	-0.94	0.03	5.66	-2.59
Defect 3	-0.39	-0.06	0.03	-2.90	-9.00
Defect 4	-0.62	-0.33	0.02	-2.62	7.43
Defect 5	0.46	-0.36	-0.03	-7.45	-15.08
Defect 6	0.30	-0.66	-0.01	2.76	8.01
Defect 7	0.67	0.71	-0.06	-2.11	-6.59
Defect 8	-0.49	0.61	-0.12	-4.78	-14.11
Defect 9	0.44	-0.53	-0.11	-4.12	-11.76
Defect 10	-0.55	-0.69	0.03	-6.68	-12.89
Defect 11	-0.15	-0.13	0.08	2.16	-15.95
Defect 12	0.47	-0.35	0.07	-6.61	15.59
Defect 13	-0.42	0.14	-0.06	-5.63	-16.99
Defect 14	-0.18	-0.52	-0.06	-8.90	-13.39
Defect 15	-0.88	0.36	-0.08	-4.97	4.34
Defect 16	0.86	-0.40	-0.06	9.53	11.95
Defect 17	0.24	-1.26	-0.05	-3.94	-18.75
Defect 18	-0.37	-0.22	-0.07	-6.40	-8.10
Defect 19	-0.16	-0.19	-0.02	-4.19	-9.44
Defect 20	-0.18	-0.42	-0.06	3.98	-20.15
Defect 21	0.10	-0.24	-0.02	-2.20	-7.51
Defect 22	-0.15	-0.45	-0.11	-8.31	-11.11
Defect 23	-0.37	-0.59	0.18	2.81	-14.78
Defect 24	-0.35	-0.13	-0.11	-8.28	-17.67
Defect 25	-0.39	-0.48	0.15	-7.40	-12.97
Defect 26	-0.65	-0.30	0.10	-9.30	-9.75
Defect 27	-0.11	-0.85	-0.18	-5.47	-15.34
Defect 28	-0.25	-0.16	-0.48	-0.43	-2.64
Defect 29	-0.03	0.15	0.06	1.89	-0.82
Defect 30	0.10	0.20	0.07	-4.63	0.82
Defect 31	0.05	0.09	-0.05	-1.61	0.79
Defect 32	0.05	-0.35	0.03	-0.86	-1.83
Defect 33	-0.11	-0.16	-0.20	-0.19	-1.40
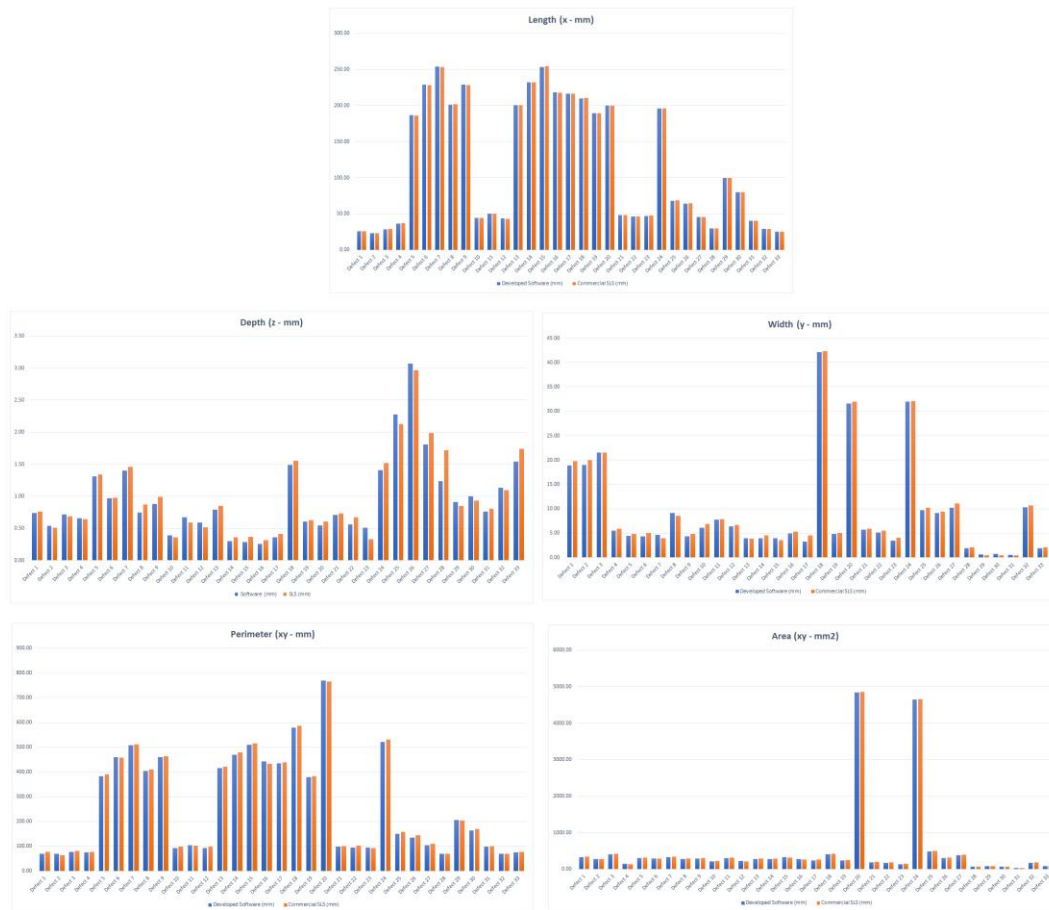
Figure 5. 57: Comparison of length a), width b), depth c), perimeter d) and area e)
measurements between the SLS and the developed algorithm.

In order to analyze the precision of the developed algorithm, it was first investigated if the difference error for length, width and depth would also behave as a random sampling from normal distribution. With the software Minitab®, it was possible to visually compare the Probability Distribution Plot of Difference (PDPD), as can be seen in Figure 5.58. It can be observed that the depth has a greater precision, because its curve is narrower compared to the length and width curves. Both the length and the width have very similar accuracies, because their curves have roughly the same spread and average. Then it was performed an Anderson-Darling test (STEPHENS, 1974) for each dimension which consists in a statistical test that confronts the calculated p-value for the dataset with an "AD" critical value, as shown in Figure 5.59. If the data's p-value is less than the AD statistic, the dataset should not be considered to be normally distributed.
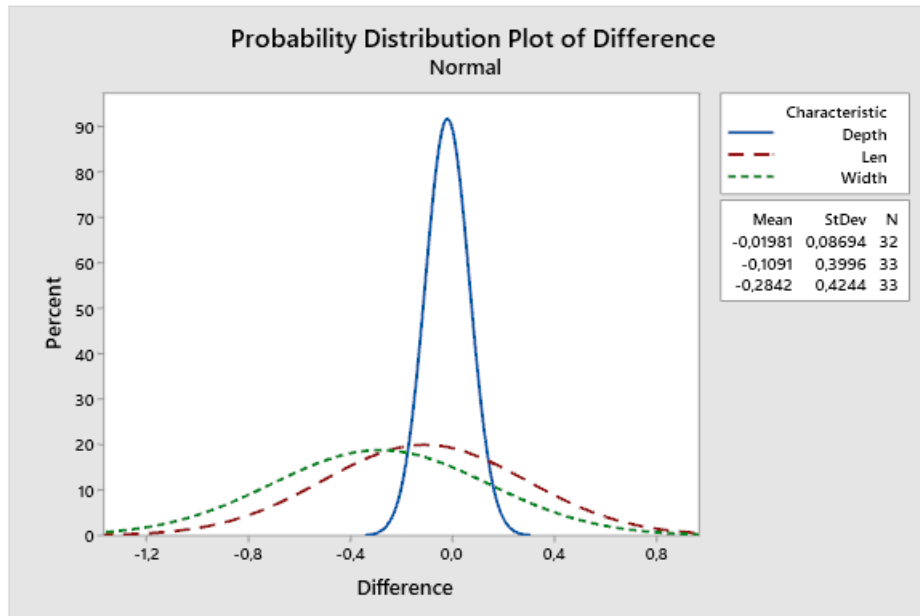
Figure 5. 58: Probability distribution plot of the difference between commercial SLS and developed algorithm.
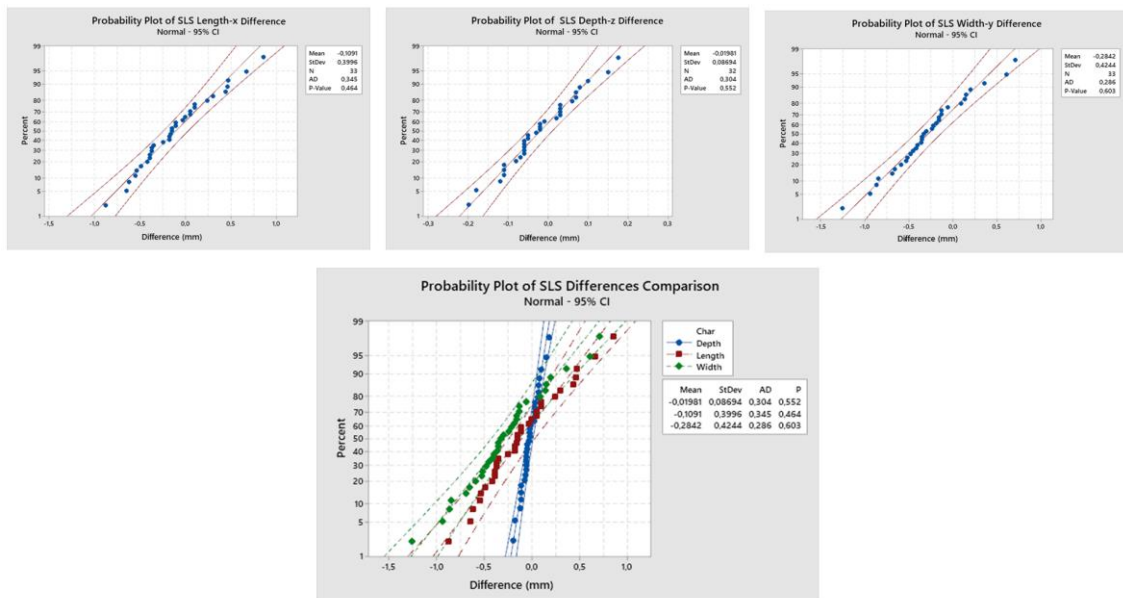
Figure 5. 59: Anderson-Darling test to verify if the difference data could be treated as normally distribute.

In Table 5.18 all the parameters could be treated as normally distributed as the data p-value was higher than the critical AD value for each case. Thus, resulting in an average error of only 0.3 mm for the superficial characteristics (length, width) and close

to zero error in depth data (0.02 mm). Based on the collected data for length, width and depth, it is expected that the results will be comprehended mostly between -0.88 mm and 0.86 mm maximum error for the length, -1.26 mm and 0.71 mm for width and -0.20 mm and 0.17 mm for depth, enough for engineering applications.

Table 5. 18: Statistical evaluation of the measurement errors.

Dimension	Average (mm)	Standard Deviation (mm)	Mini- mum (mm)	Maximum (mm)	P_value (-)	AD_stat (-)
Length	-0.11	0.40	-0.88	0.86	0.464	0.286
Width	-0.29	0.42	-1.26	0.71	0.603	0.345
Depth	-0.02	0.08	-0.20	0.17	0.552	0.304

The Gaussian probability distribution chart cannot be used to evaluate the results for the perimeter and area because they do not follow a normal data distribution. An alternative probability function that can represent a sum of square values, such as the perimeter, or the multiplication of dimensional values, such as the area, is the 3 parameter Weibull probability distribution. Figure 5.60 shows the Weibull for the perimeter results and Figure 5.61 for the area results. In addition, the AD test is also applied to check whether the data can be represented by the Weibull of three parameters and, consequently, the accuracy of the results obtained by the developed algorithm can be evaluated.
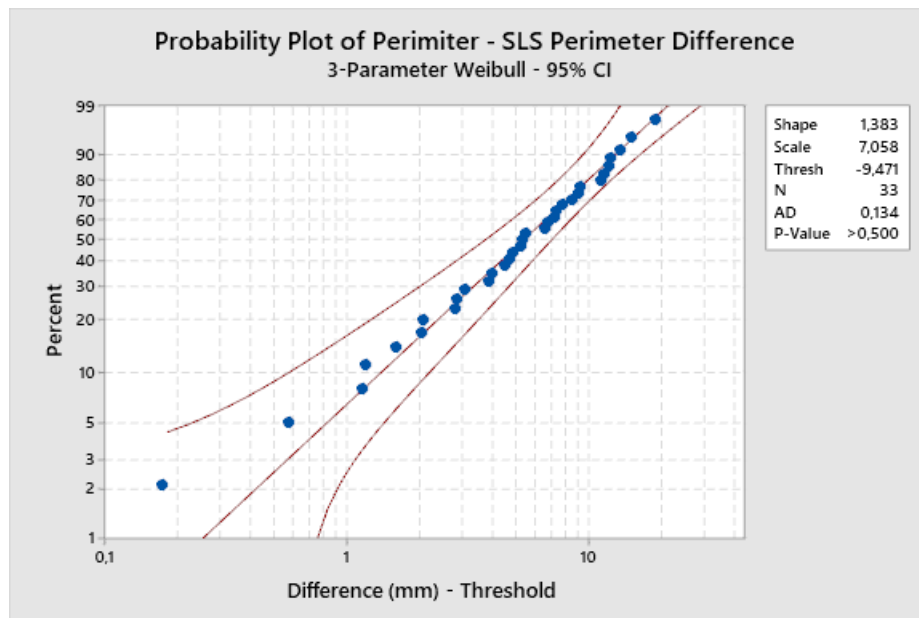
Figure 5. 60: Anderson-Darling test to verify if the difference SLS data of perimeter could be treated as 3 parameter Weibull distribution.
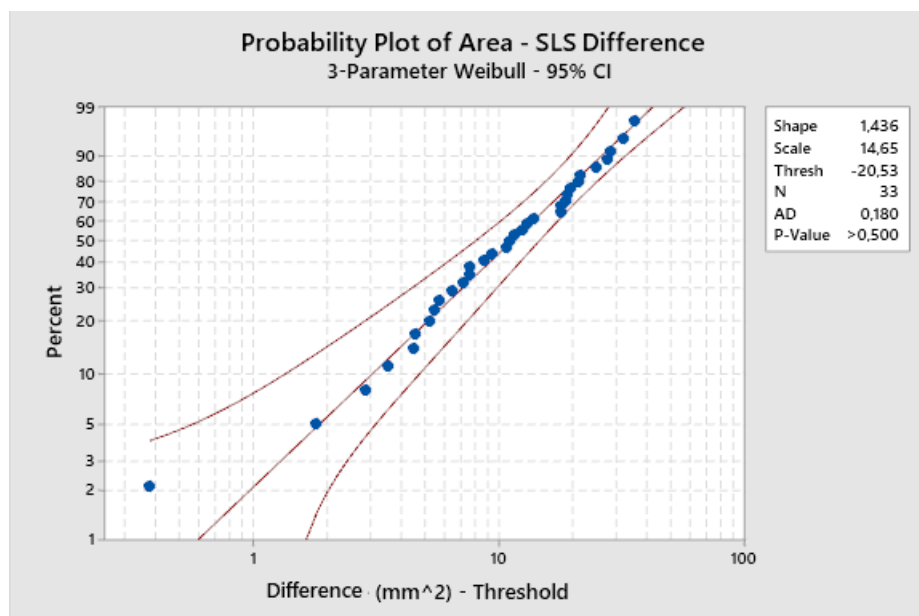
Figure 5. 61: Anderson-Darling test to verify if the difference SLS data of area could be treated as 3 parameter Weibull distribution.

As the p-value is higher than the AD-value for both the perimeter and the area, it can be stated that in Table 5.19 all the parameters could be treated as 3-Parameter Weibull distribution. The obtained error median was of 4.12 mm for the perimeter and

9.44 mm^2 for area data. Based on the collected data is expected that the results will be comprehended mostly between -9.30 mm to 9.53 mm maximum error for the perimeter and -20.15 mm^2 to 15.59 mm^2 for area, enough for engineering and the algorithm applications itself. In addition, it can still be noted that the majority of the data is contained between -0.31 mm and -6.64 mm for the perimeter and between -1.11 mm^2 and -14.93 mm^2 for the area.

Table 5. 19: Statistical evaluation of difference of the measurement errors.

Dimension	Perimeter	Area
Median	-4.12 mm	-9.44 mm^2
First quartile	-0.31 mm	-1.11 mm^2
Third quartile	-6.64 mm	-14.93 mm^2
Minimun	-9.30 mm	-20.15 mm^2
Maximun	9.53 mm	15.59 mm^2
P_value	>0.500	>0.500
AD_stat	0.134	0.180

Based on the results presented so far in this section, it is possible to validate the accuracy and functionality of the developed algorithm using the SLS technique. It can be conservatively stated that the length and width have an accuracy of ±1 mm, the depth of ±0.5 mm, the perimeter of ±10 mm and the area of ±25 mm^2.

Based on the measurements made by the algorithm, the process of classification of defects was performed in accordance with section 5.4.1 d). The following Table 5.20 shows the result for the classification of the defects inspected by SLS and processed by the developed algorithm. As it can be observed, still in table 5.20, the developed algorithm classification response for the 33 inspected defects was excellent, since there was only one deviation from reality. This deviation occurred for defect 3, where the developed algorithm indicated a non-conservative response as to the severity of the defect. This question can be easily resolved by inserting a safety margin or even a

variation in the rule for determining the severity of the defect, according to the required demand.

Table 5. 20: Classification of defects according to their orientation, morphology and severity (by color scale).

Defect	Real (Orientation / Morphology)	Algorithm (Orientation / Morphology)
Defect 1	Circular / Intense dent	Circular / Intense dent
Defect 2	Circular / Intense dent	Circular / Intense dent
Defect 3	Circular / Intense dent	Circular / Intense dent
Defect 4	Longitudinal / Scratch	Longitudinal / Scratch
Defect 5	Longitudinal / Scratch	Longitudinal / Scratch
Defect 6	Longitudinal / Extended scratch	Longitudinal / Extended scratch
Defect 7	Longitudinal / Extended scratch	Longitudinal / Extended scratch
Defect 8	Longitudinal / Extended scratch	Longitudinal / Extended scratch
Defect 9	Longitudinal / Extended scratch	Longitudinal / Extended scratch
Defect 10	Longitudinal / Scratch	Longitudinal / Scratch
Defect 11	Longitudinal / Scratch	Longitudinal / Scratch
Defect 12	Longitudinal / Scratch	Longitudinal / Scratch
Defect 13	Longitudinal / Extended scratch	Longitudinal / Extended scratch
Defect 14	Longitudinal / Extended scratch	Longitudinal / Extended scratch
Defect 15	Longitudinal / Extended scratch	Longitudinal / Extended scratch
Defect 16	Longitudinal / Extended scratch	Longitudinal / Extended scratch
Defect 17	Longitudinal / Extended scratch	Longitudinal / Extended scratch
Defect 18	Longitudinal / Extended scratch	Longitudinal / Extended scratch
Defect 19	Longitudinal / Extended scratch	Longitudinal / Extended scratch
Defect 20	Longitudinal / Extended scratch	Longitudinal / Extended scratch
Defect 21	Longitudinal / Scratch	Longitudinal / Scratch
Defect 22	Longitudinal / Scratch	Longitudinal / Scratch
Defect 23	Longitudinal / Scratch	Longitudinal / Scratch
Defect 24	Longitudinal / Extended scratch	Longitudinal / Extended scratch
Defect 25	Longitudinal / Scratch	Longitudinal / Scratch
Defect 26	Longitudinal / Scratch	Longitudinal / Scratch
Defect 27	Longitudinal / Scratch	Longitudinal / Scratch
Defect 28	Longitudinal / Crack	Longitudinal / Crack
Defect 29	Longitudinal / Crack	Longitudinal / Crack
Defect 30	Longitudinal / Crack	Longitudinal / Crack
Defect 31	Longitudinal / Crack	Longitudinal / Crack
Defect 32	Longitudinal / Scratch	Longitudinal / Scratch
Defect 33	Longitudinal / Scratch	Longitudinal / Scratch

The technique of measurement and data generation by SLS has proved to be suitable for evaluation and validation of the developed algorithm. The performance of the developed algorithm demonstrated its efficiency in automatically analyzing the data obtained by the structured light system, as well as performing the defect recognition and evaluation with an accuracy conservatively stated for length and width of ±1 mm, for depth of 0.5 mm, for perimeter of 10 mm and for area of 25 mm. In addition, it was also demonstrated the functionality of the developed classification algorithm regarding defect's orientation, morphology and severity, proving then to be a worthy tool to reach the automation of surface inspections processing on-line data from in-line inspection system.

5.4.3. Results processed by the developed algorithm

Once the developed algorithm has been validated, the data obtained by inspections with laser line, ECs and Hall sensor were processed by the algorithm to evaluate its performance.

a. Laser line system

It is possible to observe representatively the mapping results achieved by the algortithm in Figure 5.62, on the right column. On the left column there are the results from the Digital Twin. It's clear the resolution of the defect's detection through the colour map shows a similarity results between the digital twin and the algorithm. An important detail to highlight is on the comparison between defect 29 on Figure 5.56 l) and Figure 5.62 l), because although the qualitative result of this defect for LL appears worse than that of the digital twin, there is no influence on the quantitative results, as will be shown below.

a) **b)**

c) **d)**

e) **f)**

g) **h)**

i) **j)**

k) **l)**
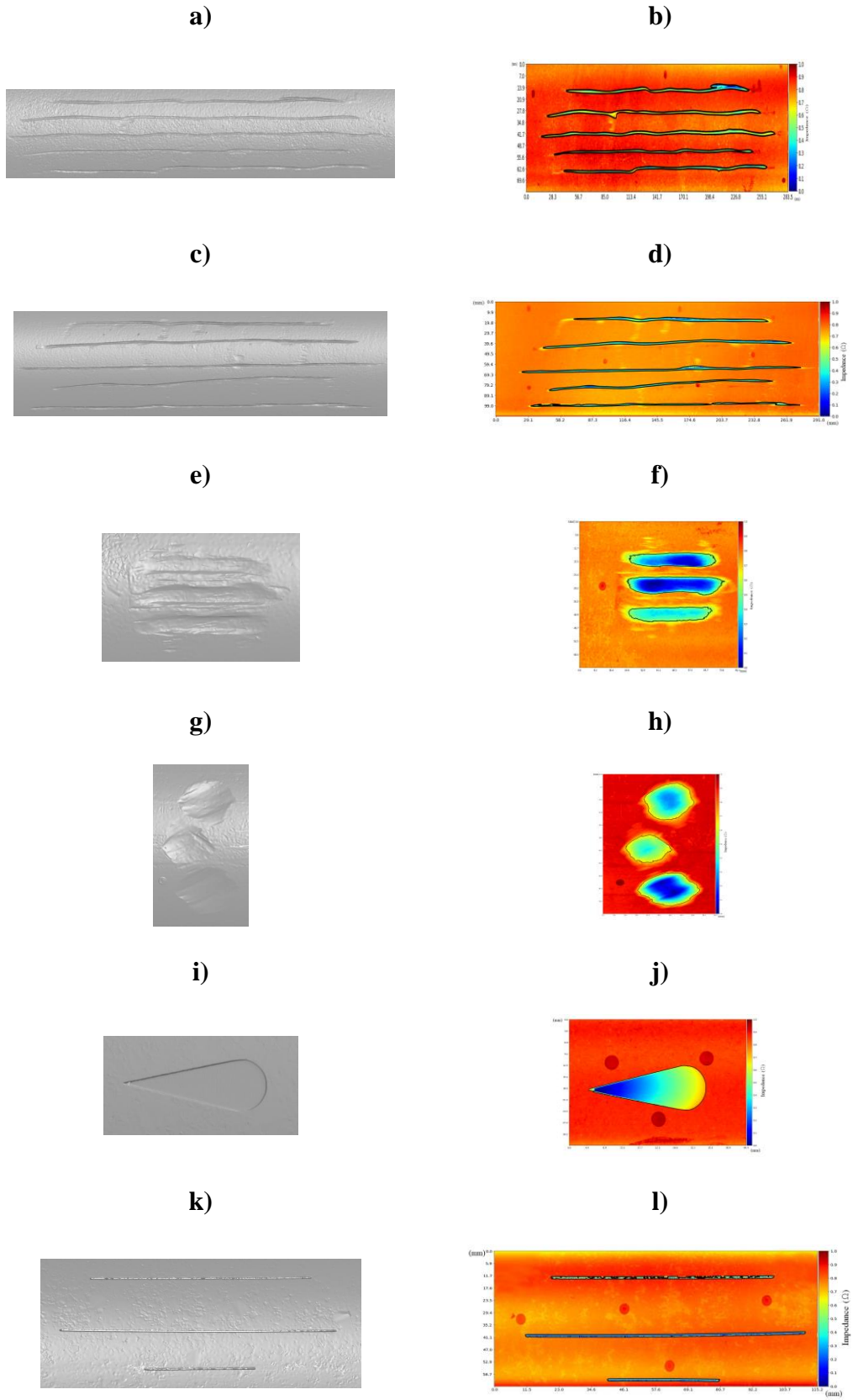
Figure 5. 62: Reconstruction of defects by structured light respectively in a), c), e), g), i) and k) with their respective maps and contours made by the developed algorithm using LL data in b), d), f), h), j) and l).

153

The Table 5.21 and 5.22 shows the nominal differences between the main values extracted by the developed algorithm from LL's data with the real defect's values measured by SLS commercial software from LL's data.

Table 5. 21: Differences of measures between the LL measures on SLS commercial software and the LL's from the developed algorithm – Part 1.

Defect	Length (mm)	Width (mm)	Depth (mm)	Perimeter (mm)	Area (mm²)
Defect 1	0.24	-0.59	-0.03	-2.57	-10.71
Defect 2	-0.20	0.64	0.06	11.19	7.07
Defect 3	0.21	-0.12	0.02	5.04	-0.63
Defect 4	-0.53	-0.44	-0.03	2.80	15.36
Defect 5	0.69	-0.13	-0.02	-1.95	-8.40
Defect 6	-0.31	0.20	-0.10	11.64	14.23
Defect 7	-0.42	0.88	-0.02	7.18	2.33
Defect 8	-0.91	0.41	0.25	5.48	-5.26
Defect 9	0.14	-0.91	0.08	2.72	-1.62
Defect 10	-0.51	0.19	0.06	0.06	-4.15
Defect 11	0.52	-0.05	0.01	8.05	-6.16
Defect 12	0.18	-0.19	0.02	3.53	22.46
Defect 13	-0.66	-0.17	-0.05	5.23	-6.55
Defect 14	-0.11	0.03	0.13	0.58	-3.71
Defect 15	0.99	-0.48	0.29	0.33	12.81
Defect 16	1.01	0.14	0.18	15.70	21.92
Defect 17	0.48	-0.30	0.27	3.85	-10.39
Defect 18	0.14	-0.40	0.08	1.28	0.06
Defect 19	0.75	-0.06	0.22	2.76	-2.52
Defect 20	-0.06	-0.46	0.08	12.15	-12.88
Defect 21	-0.46	-0.13	-0.14	5.47	2.43
Defect 22	0.19	0.94	-0.19	0.68	-2.53
Defect 23	-0.30	0.30	0.19	11.47	-7.41
Defect 24	0.67	0.82	-0.06	-2.70	-12.51
Defect 25	-0.91	-0.58	-0.06	2.91	-6.80

Table 5. 22: Differences of measures between the LL measures on SLS commercial software and the LL's from the developed algorithm – Part 2 continuation.

Defect	Length (mm)	Width (mm)	Depth (mm)	Perimeter (mm)	Area (mm²)
Defect 26	0.28	0.63	-0.10	0.49	0.71
Defect 27	-0.96	-0.11	0.12	5.52	-7.92
Defect 28	-0.37	0.16	-0.03	6.41	2.50
Defect 29	-0.44	-0.02	0.10	8.45	8.37
Defect 30	-0.67	0.33	0.09	1.36	6.64
Defect 31	-0.14	0.31	0.05	9.17	7.57
Defect 32	0.09	-0.09	0.00	8.96	3.76
Defect 33	-0.19	0.04	0.02	9.64	6.60

In order to analyze the precision of LL's results on the developed algorithm, it was first investigated if the difference error for length, width and depth would also behave as a random sampling from normal distribution on Minitab®. It was possible to visually compare the PDPD, as can be seen in Figure 5.63. It can be observed that the depth has a greater precision, because its curve is narrower compared to the length and width curves. Both the length and the width have very similar accuracies, because their curves have roughly the same spread and average. Then it was performed an Anderson-Darling test (STEPHENS, 1974) for each dimension, as shown in Figure 5.64.
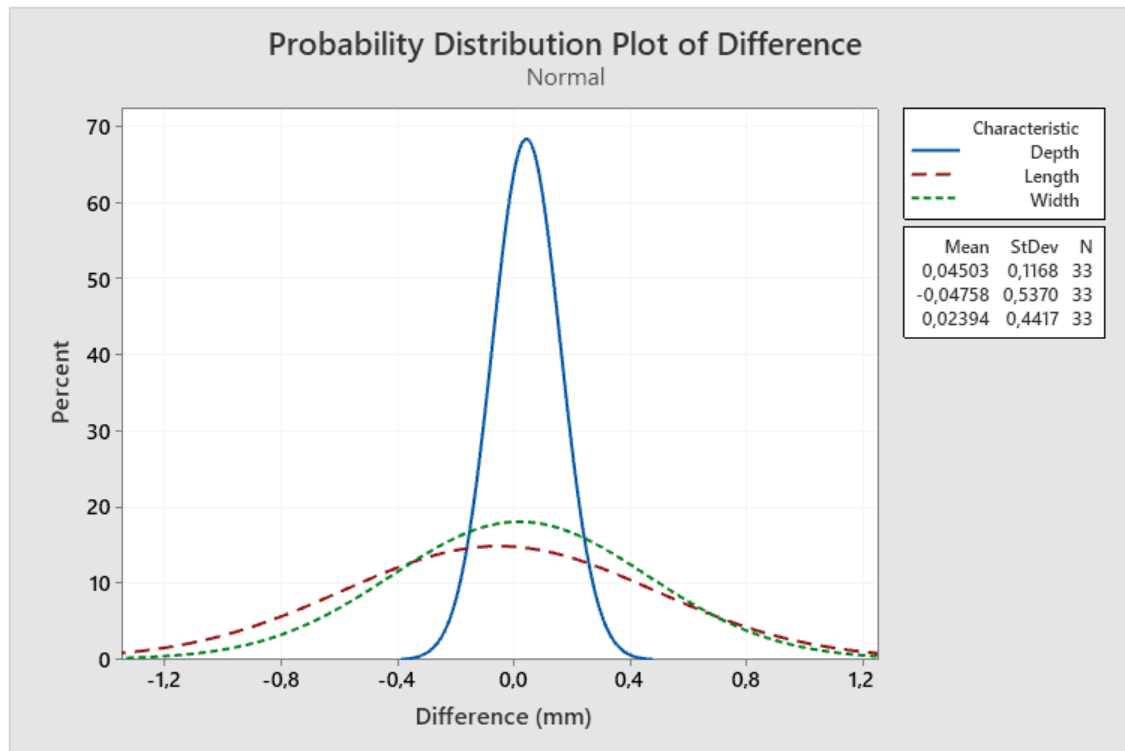
Figure 5. 63: Probability distribution plot of the difference between LL and developed algorithm.
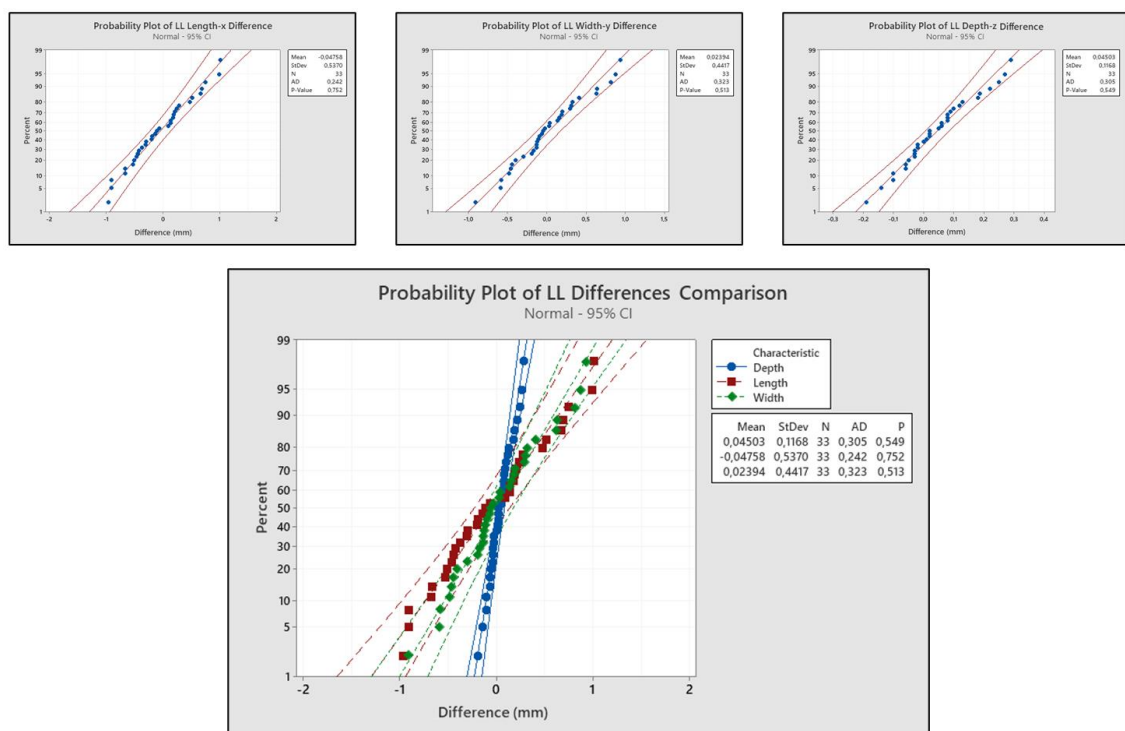
Figure 5. 64: Anderson-Darling test to verify if the difference LL data could be treated as normally distribute.

In Table 5.23 all the parameters could be treated as normally distributed as the data p-value was higher than the critical AD value for each case. Thus, resulting in an average error of only 0.2 mm for the width and close to zero error in depth and length data. Based on the collected data for length, width and depth data is expected that the results will be comprehended mostly between -0.96 mm and 1.01 mm maximum error for the length, -0.91 mm and 0.94 mm for width and -0.19 mm and 0.29 mm for depth.

Table 5. 23: Statistical evaluation of the measurement errors.

Dimension	Average (mm)	Standard Deviation (mm)	Minimum	Maximum	P_value (-)	AD_stat (-)
Length	-0.05	0.54	-0.96	1.01	0.752	0.242
Width	0.20	0.44	-0.91	0.94	0.513	0.323
Depth	0.04	0.12	-0.19	0.29	0.549	0.305

As already clarified the Gaussian probability distribution chart cannot be used to evaluate the results for the perimeter and area because they do not follow a normal data distribution. Figure 5.66 shows the Weibull result of three parameters for the perimeter results and Figure 5.67 for the area results. In addition, the AD test is also applied to check whether the data can be represented by the Weibull of three parameters and, consequently, the accuracy of the results obtained by the developed algorithm can be evaluated.
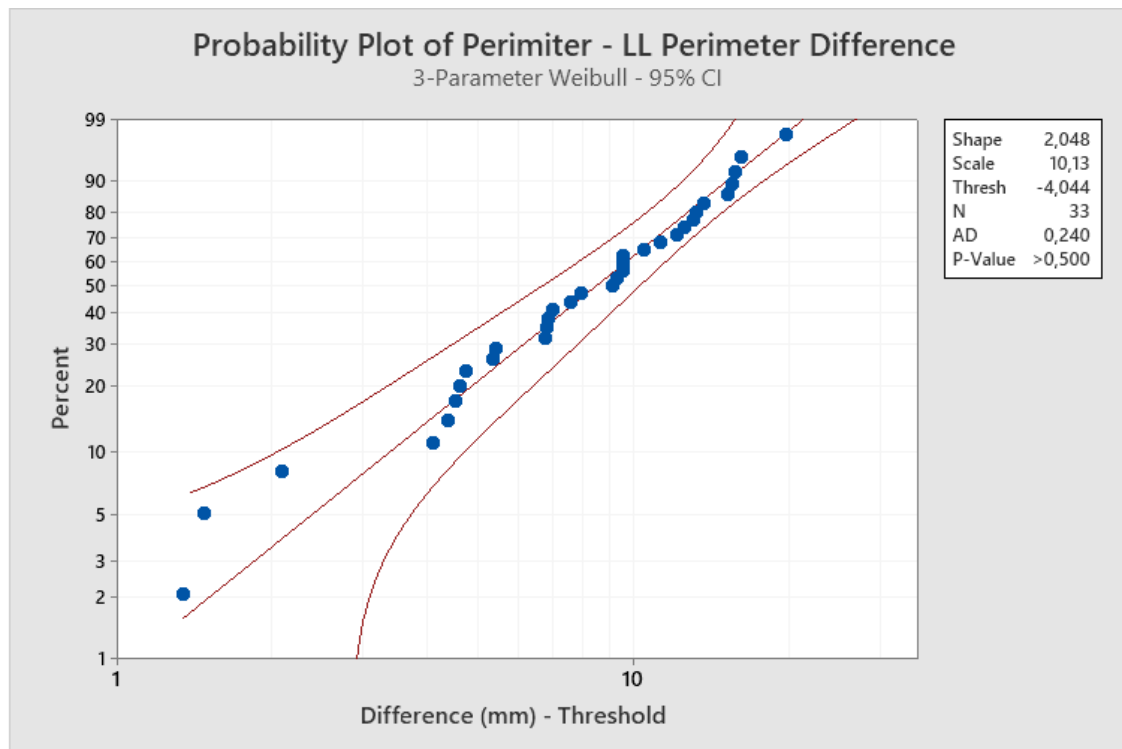
Figure 5. 65: Anderson-Darling test to verify if the difference LL data of perimeter could be treated as 3 parameter Weibull distribution.
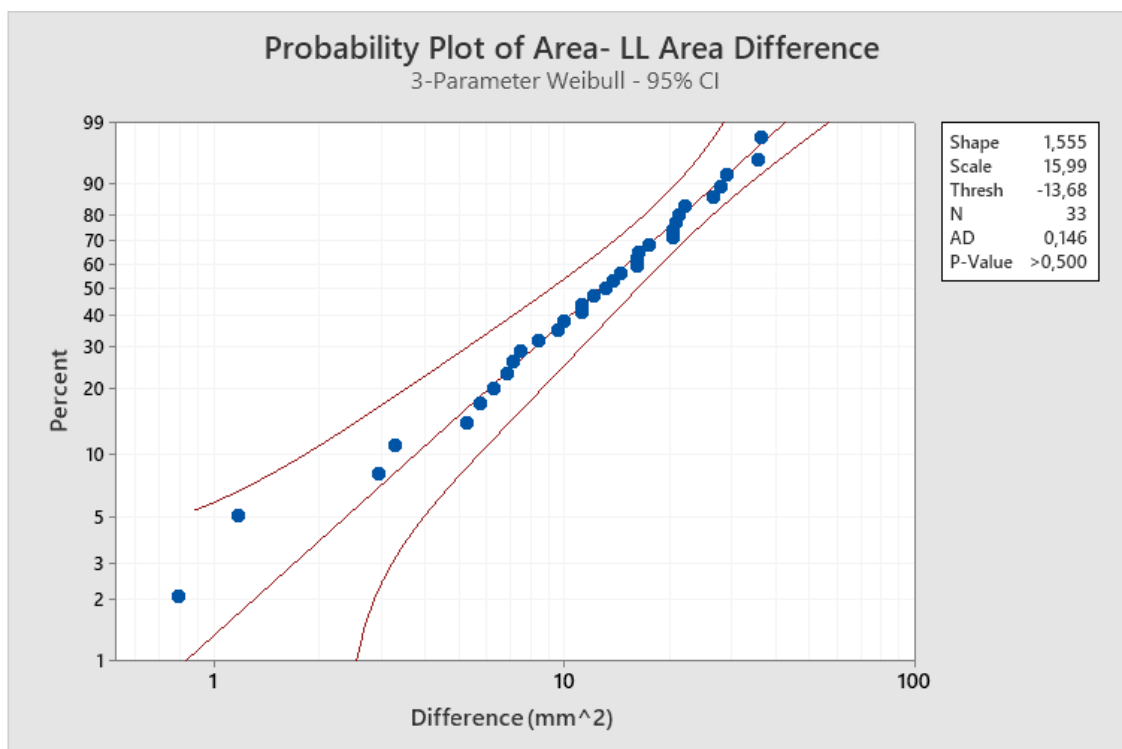
Figure 5. 66: Anderson-Darling test to verify if the difference LL data of area could be treated as 3 parameter Weibull distribution.

As the p-value is higher than the AD-value for both the perimeter and the area, it can be stated that the in Table 5.24 all the parameters could be treated as 3-Parameter Weibull distribution. The obtained error median was of -5.04 mm for the perimeter and 0.62 mm^2 for area data. Based on the collected data is expected that the results will be comprehended mostly between -2.70 mm to 15.69 mm maximum error for the perimeter and -12.89 mm^2 to 22.45 mm^2 for area. In addition, it can still be noted that the majority of the data is contained between 0.98 mm and 8.70 mm for the perimeter and between -6.67 mm^2 and 6.85 mm^2 for the area.

Table 5. 24: Statistical evaluation of difference of the measurement errors.

Dimension	Perimeter	Area mm^2
Median	-5.04 mm	-0.62 mm^2
First quartile	0.98 mm	-6.67 mm^2
Third quartile	8.70 mm	6.85 mm^2
Minimum	-2.70 mm	-12.89 mm^2
Maximum	15.69 mm	22.45 mm^2
P_value	>0.500	>0.500
AD_stat	0.240	0.146

Also based on the measurements made by the algorithm on LL data, the process of classification of defects was performed. The following Table 5.26 and 5.27 shows the result for the classification of the defects inspected by LL and processed by the developed algorithm. As it can be observed, still in Table 5.25 and 5.26, the developed algorithm classification response for the 33 inspected defects was also excellent, since there was only two deviation from reality. This deviation occurred for defect 4 and defect 22, where the developed algorithm indicated a conservative response for the severity of the defect. As already mentioned, this question can be easily resolved by inserting a safety margin or even a variation in the rule for determining the severity of the defect, according to the required demand.

Table 5. 25: LL's classification of defects according to their orientation, morphology and severity (by color scale) – part 1.

Defect	Real (Orientation / Morphology / Severity - color)	Algorithm (Orientation / Morphology / Severity - color)
Defect 1	Circular / Intense dent	Circular / Intense dent
Defect 2	Circular / Intense dent	Circular / Intense dent
Defect 3	Circular / Intense dent	Circular / Intense dent
Defect 4	Longitudinal / Scratch	Longitudinal / Scratch
Defect 5	Longitudinal / Scratch	Longitudinal / Scratch
Defect 6	Longitudinal / Extended scratch	Longitudinal / Extended scratch
Defect 7	Longitudinal / Extended scratch	Longitudinal / Extended scratch
Defect 8	Longitudinal / Extended scratch	Longitudinal / Extended scratch
Defect 9	Longitudinal / Extended scratch	Longitudinal / Extended scratch
Defect 10	Longitudinal / Scratch	Longitudinal / Scratch
Defect 11	Longitudinal / Scratch	Longitudinal / Scratch
Defect 12	Longitudinal / Scratch	Longitudinal / Scratch
Defect 13	Longitudinal / Extended scratch	Longitudinal / Extended scratch
Defect 14	Longitudinal / Extended scratch	Longitudinal / Extended scratch
Defect 15	Longitudinal / Extended scratch	Longitudinal / Extended scratch
Defect 16	Longitudinal / Extended scratch	Longitudinal / Extended scratch
Defect 17	Longitudinal / Extended scratch	Longitudinal / Extended scratch
Defect 18	Longitudinal / Extended scratch	Longitudinal / Extended scratch
Defect 19	Longitudinal / Extended scratch	Longitudinal / Extended scratch
Defect 20	Longitudinal / Extended scratch	Longitudinal / Extended scratch
Defect 21	Longitudinal / Scratch	Longitudinal / Scratch
Defect 22	Longitudinal / Scratch	Longitudinal / Scratch

Table 5. 26: LL's classification of defects according to their orientation, morphology and severity (by color scale) – part 2 continuation.

Defect	Real (Orientation / Morphology)	Algorithm (Orientation / Morphology)
Defect 23	**Longitudinal / Scratch**	**Longitudinal / Scratch**
Defect 24	**Longitudinal / Extended scratch**	**Longitudinal / Extended scratch**
Defect 25	**Longitudinal / Scratch**	**Longitudinal / Scratch**
Defect 26	**Longitudinal / Scratch**	**Longitudinal / Scratch**
Defect 27	**Longitudinal / Scratch**	**Longitudinal / Scratch**
Defect 28	**Longitudinal / Crack**	**Longitudinal / Crack**
Defect 29	**Longitudinal / Crack**	**Longitudinal / Crack**
Defect 30	**Longitudinal / Crack**	**Longitudinal / Crack**
Defect 31	**Longitudinal / Crack**	**Longitudinal / Crack**
Defect 32	**Longitudinal / Scratch**	**Longitudinal / Scratch**
Defect 33	**Longitudinal / Scratch**	**Longitudinal / Scratch**

LL technique has also proved to bring excellent results for the developed algorithm. The performance of the developed algorithm demonstrated, as well for SLS, its efficiency in automatically analyzing the data obtained by laser line system. Besides that, it was also possible to observe the algorithm's good performance for the defect recognition and evaluation with an accuracy conservatively stated for length and width of ±1.0 mm, the depth of ±0.5 mm, the perimeter of 20 mm and the area of 25 mm^2 and, in addition, it was demonstrated the functionality regarding defect's orientation, morphology and severity.

b. Electromagnetic System

The same statistical evaluation done so far for SLS and LL were done for EC and Hall sensor geometric profilometer (HGP) results. However, for these techniques the representative defects were selected to be processed in the developed algorithm. For EC defects from 1 to 4, 20, 25 to 28, 32 and 33 were analyzed and defects from 1 to 4, 10 to 12, 25, 27, 28 and 32 were used for HGP.

i. EC data

It is possible to observe the exemplary mapping results achieve by the developed algorithm in Figure 5.67 for EC on the right column and its comparison with the digital twin on the left column. The result of the EC maps is not as clear as those presented for

LL and SLS, as was already expected, but it is still evident the detection of defects by the technique along with the processing performed. A peculiarity of the EC results can be observed in Figure 5.67 d), where the EC technique detects the different notches seen in c) as a single defect. This was also expected, as the EC technique has a volumetric response of the inspected region and the diameter of the coils being greater than the distance between the notches the response signal mixes.

a)   **b)**

c)

d)

e)
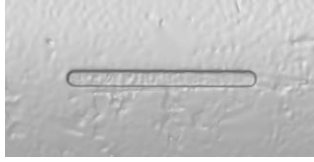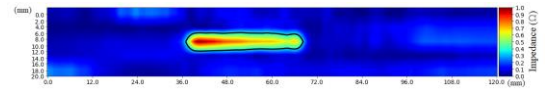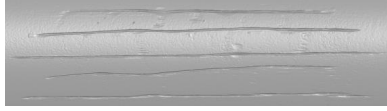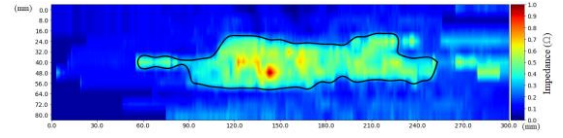
f)
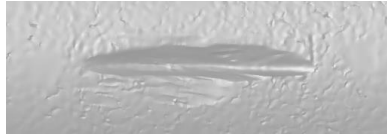
g)
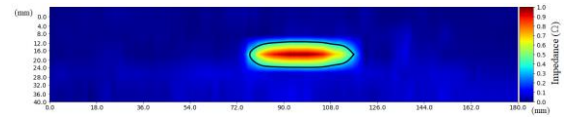
h)
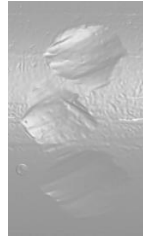
i)
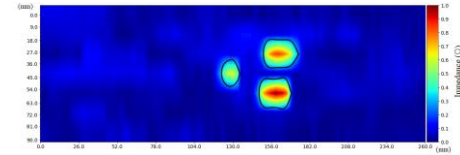
j)
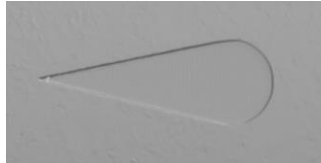
k)
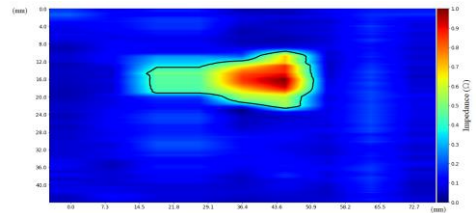
l)
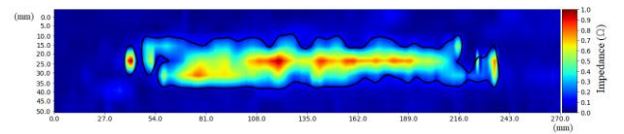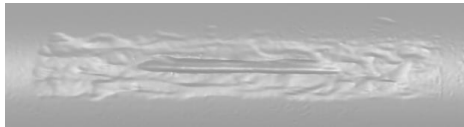
Figure 5. 67: Reconstruction of defects by structured light respectively in a), c), e), g), i) and k) with their respective maps and contours made by the developed algorithm using EC data in b), d), f), h), j) and l).

The Table 5.27 shows the nominal differences between the main values extracted by the developed algorithm from EC's data with the real defect's values measured by SLS commercial software from its digital twin data. Unlike the other results presented so far, the depth of defects will not be evaluated for EC data, since the EC response is a voltage and due to the volumetric effect of it the depth versus voltage relation is not direct. The development of this correlation itself should be a separate research work and it is outside the scope of the present work.

Table 5. 27: Differences of measures between the SLS measures on SLS commercial software and the EC's from the developed algorithm.

Defect	Length (mm)	Width (mm)	Perimeter (mm)	Area (mm²)
Defect 1	-4.14	-3.05	13.41	25.24
Defect 2	-11.21	-1.08	6.40	-113.15
Defect 3	-5.00	-1.00	-9.82	-52.03
Defect 4	3.22	5.01	10.19	29.60
Defect 20	8.65	6.84	-28.12	128.78
Defect 25	-4.39	1.28	-4.36	-55.13
Defect 26	-0.26	-1.61	-41.19	-35.39
Defect 27	-3.52	1.61	37.29	67.44
Defect 28	0.43	1.13	-6.85	0.27
Defect 32	-0.06	1.02	7.10	144.02
Defect 33	1.73	3.23	-19.14	51.22

In order to analyze the precision of EC's results on the developed algorithm, it was first investigated if the difference error for length and width would also behave as a random sampling from normal distribution on Minitab®. It was possible to visually compare the PDPD, as can be seen in Figure 5.68 and it can be observed that the width has a slightly greater precision, because its curve is narrower compared to the length curve. Then it was performed an Anderson-Darling test (Stephens, 1974) for both dimensions, as shown in Figure 5.69.
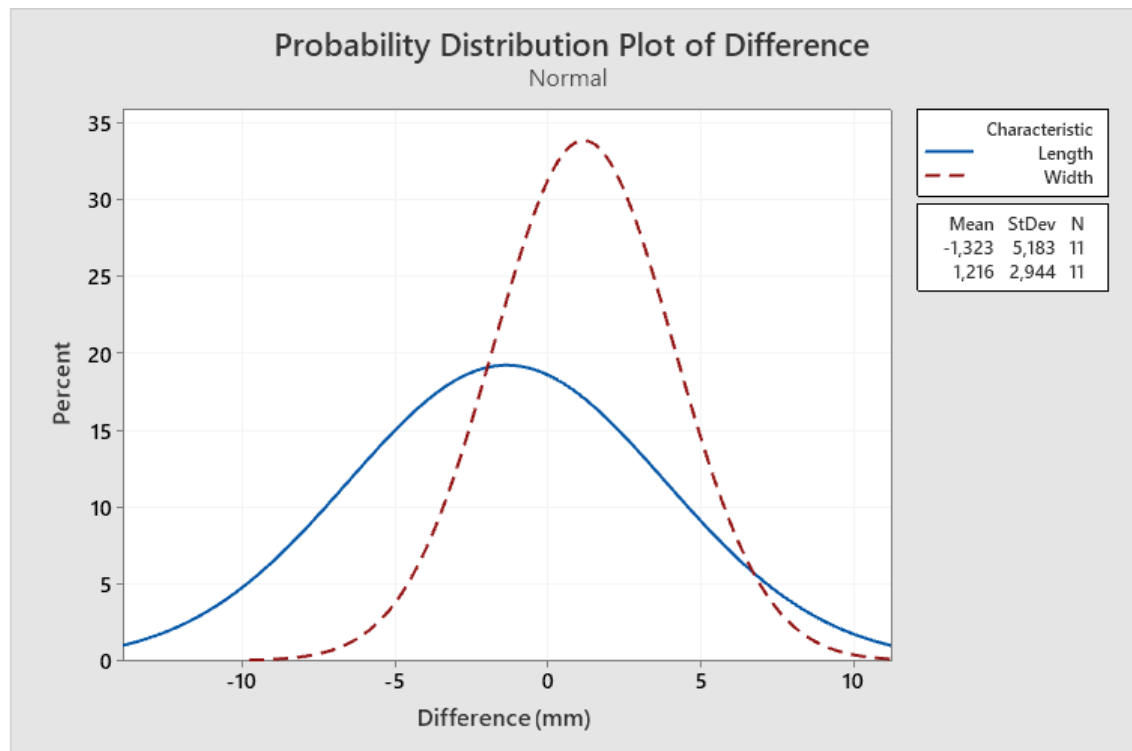
Figure 5. 68: Probability distribution plot of the difference between EC and developed algorithm.
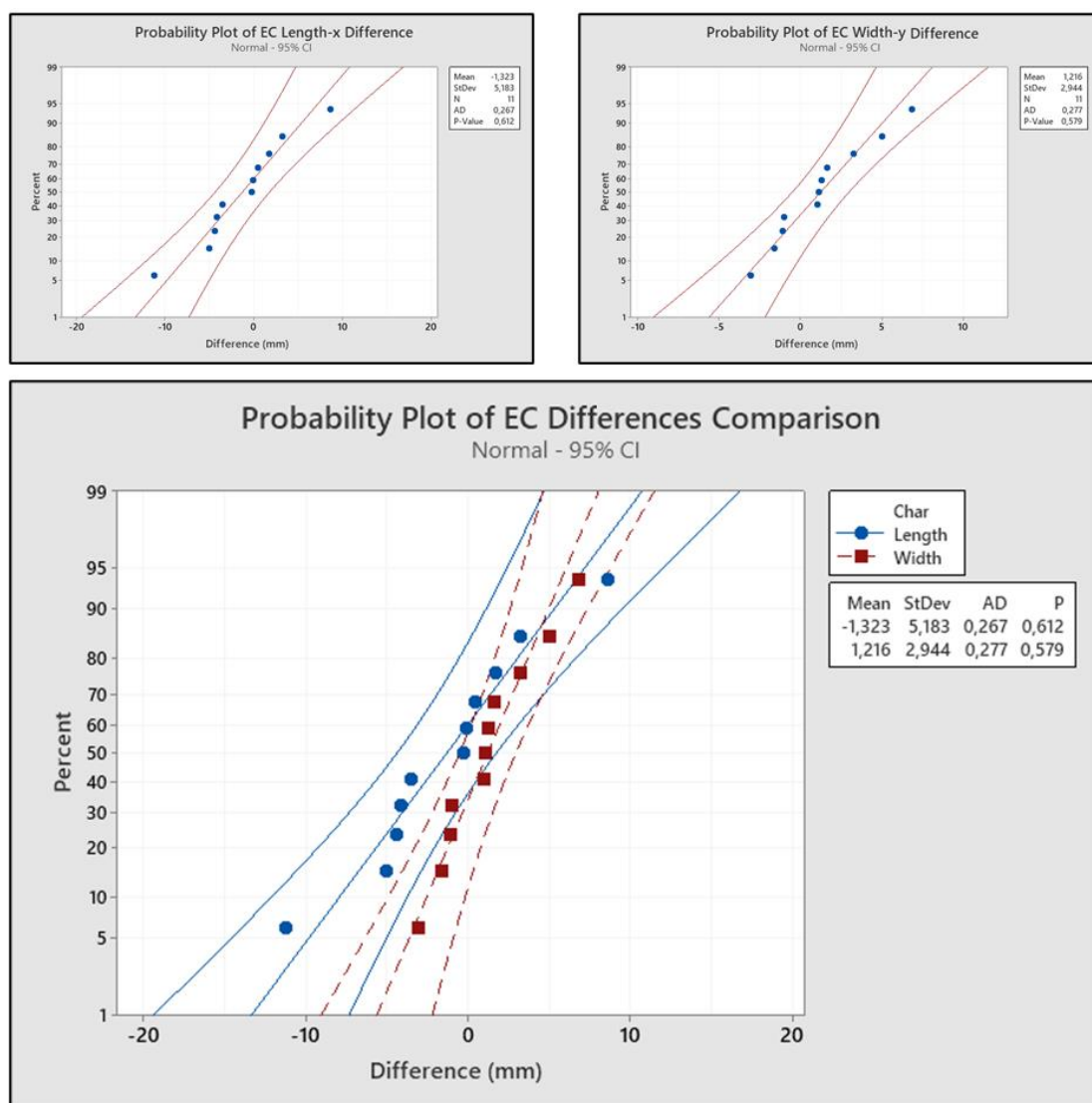
Figure 5. 69: Anderson-Darling test to verify if the difference EC data could be treated as normally distribute.

In Table 5.28 all the parameters could be treated as normally distributed as the data p-value was higher than the critical AD value for each case. Thus, resulting in an average error of -13.23 mm for the length and 1.21 mm for width. Based on the collected data for length and width data's is expected that the results will be comprehended mostly between -11.21 mm and 8.65 mm maximum error for the length and -3.05 mm and 6.84 mm for width.

Table 5. 28: Statistical evaluation of the measurement errors.

Dimension	Average	Standard	Minimum	Maximum	P_value	AD_stat

	(mm)	Deviation (mm)			(-)	(-)
Length	-1.32	5.18	-11.21	8.65	0.612	0. 267
Width	1.21	2.94	-3.05	6.84	0. 579	0.277

Figure 5.70 shows the Weibull result of three parameters for the perimeter results and Figure 5.71 for the area results. In addition, the AD test is also applied to check whether the data can be represented by the Weibull of three parameters and, consequently, the accuracy of the results obtained by the developed algorithm can be evaluated.
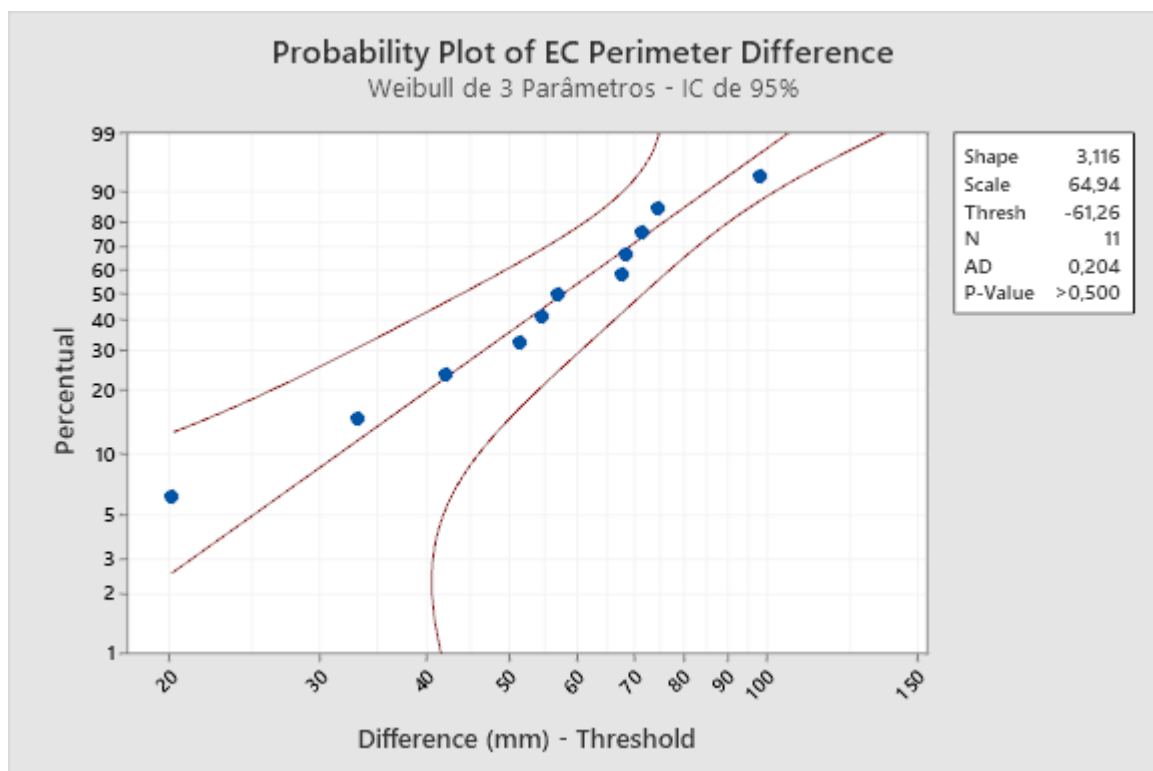
Figure 5. 70: Anderson-Darling test to verify if the difference EC data of perimeter could be treated as 3 parameter Weibull distribution.
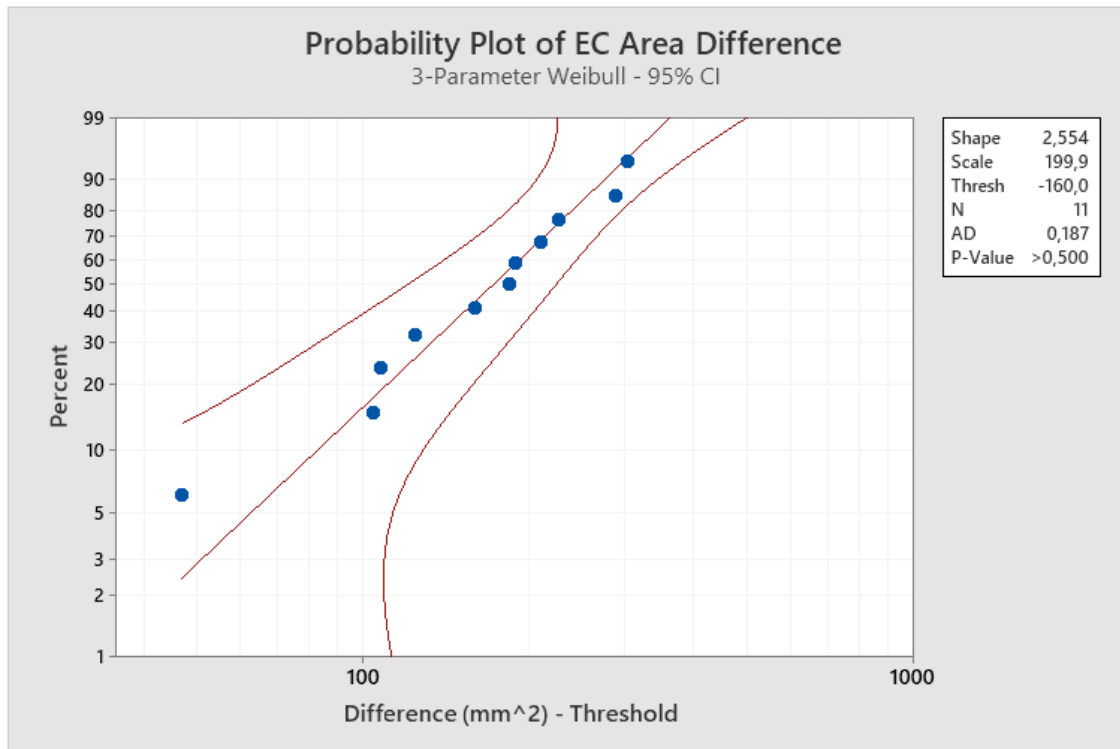
Figure 5. 711: Anderson-Darling test to verify if the difference EC data of area could be treated as 3 parameter Weibull distribution.

As the p-value is higher than the AD-value for both the perimeter and the area, it can be stated that the in Table 5.30 all the parameters could be treated as 3-Parameter Weibull distribution. The obtained error median was of -4.36 mm for the perimeter and 25.24 mm^2 for area data. Based on the collected data is expected that the results will be comprehended mostly between -41.19 mm and 37.29 mm maximum error for the perimeter and -113.50 mm^2 and 144.02 mm^2 for area. In addition, it can still be noted that the majority of the data is contained between -19.14 mm and 10.19 mm for the perimeter and between -52.03 mm^2 and 67.44 mm^2 for the area.

Table 5. 29: Statistical evaluation of difference of the measurement errors.

Dimension	Perimeter	Area
Median	-4.36 mm	25.24 mm^2
First quartile	-19.14 mm	-52.03 mm^2
Third quartile	10.19 mm	67.44 mm^2
Minimum	-41.19 mm	-113.150 mm^2
Maximum	37.29 mm	144.02 mm^2
P_value	>0.500	>0.500
AD_stat	0.204	0.187

Based on the results presented for EC data, it is also possible to validate the accuracy and functionality of the algorithm using the EC technique. It can be conservatively stated that the length has an accuracy of ±15.0 mm, the width of ±10.0 mm, the perimeter of ±45 mm and the area of ±150 mm^2. As expected, these values are very similar with the results obtained by SLS. These results are much less accurate when compared to the results of optical techniques. It is important to emphasize that a relevant part of these errors is associated to human error due to manual inspection and, consequently, variation in the speed of inspection and variation in the lateral resolution of the inspection matrix performed. However, the algorithm developed was able to automatically process EC data and extract its main geometric features.

Also based on the measurements made by the algorithm on EC data, the process of classification of defects was performed. The following Table 5.30 shows the result for the classification of the defects inspected by EC and processed by the developed algorithm. As it can be observed, still in Table 5.30 the algorithm classification response for the 11 inspected data of defects was also good, since there was no deviation from reality, regarding the defect orientation and morphology.

Table 5. 30: EC's classification of defects according to their orientation and morphology.

Defect	Real (Orientation / Morphology)	Algorithm (Orientation / Morphology)
Defect 1	Circular / Dent	Circular / Dent
Defect 2	Circular / Dent	Circular / Dent
Defect 3	Circular / Dent	Circular / Dent
Defect 4	Longitudinal / Scratch	Longitudinal / Scratch
Defect 20	Longitudinal / Extended scratch	Longitudinal / Extended scratch
Defect 25	Longitudinal / Scratch	Longitudinal / Scratch
Defect 26	Longitudinal / Scratch	Longitudinal / Scratch
Defect 27	Longitudinal / Scratch	Longitudinal / Scratch
Defect 28	Longitudinal / Crack	Longitudinal / Crack
Defect 32	Longitudinal / Scratch	Longitudinal / Scratch
Defect 33	Longitudinal / Scratch	Longitudinal / Scratch

EC technique has also proved to bring excellent results for the developed algorithm, even with the issues regarding the manually data acquisition. The performance of the developed algorithm demonstrated its functionality in automatically analyzing the data obtained by EC tests. Besides that, it was also possible to observe the algorithm's performance for the defect recognition and evaluation with an accuracy conservatively stated for length have an accuracy of ±15.0 mm, the width of ±10.0 mm, the perimeter of ±45 mm and the area of ±150 mm^2 and, in addition, it was demonstrated the defect's orientation and morphology classification.

ii.   HGP data

It is possible to observe a representatively mapping results achieve by the developed algorithm in Figure 5.72 for HGP on the right column and its comparison with the digital twin on the left column. The result of the HGP maps is also not as clear as those presented for LL and SLS, as was already expected, but it is still evident the detection of defects by the technique along with the processing performed. A significant point for HGP results is that their lateral resolution is highly dependent on the distance

between the inspection steps and the region where the tip of the rod touches the defect. For this reason, the results of the defect maps are slightly deformed, despite the excellent signal to noise ratio obtained.
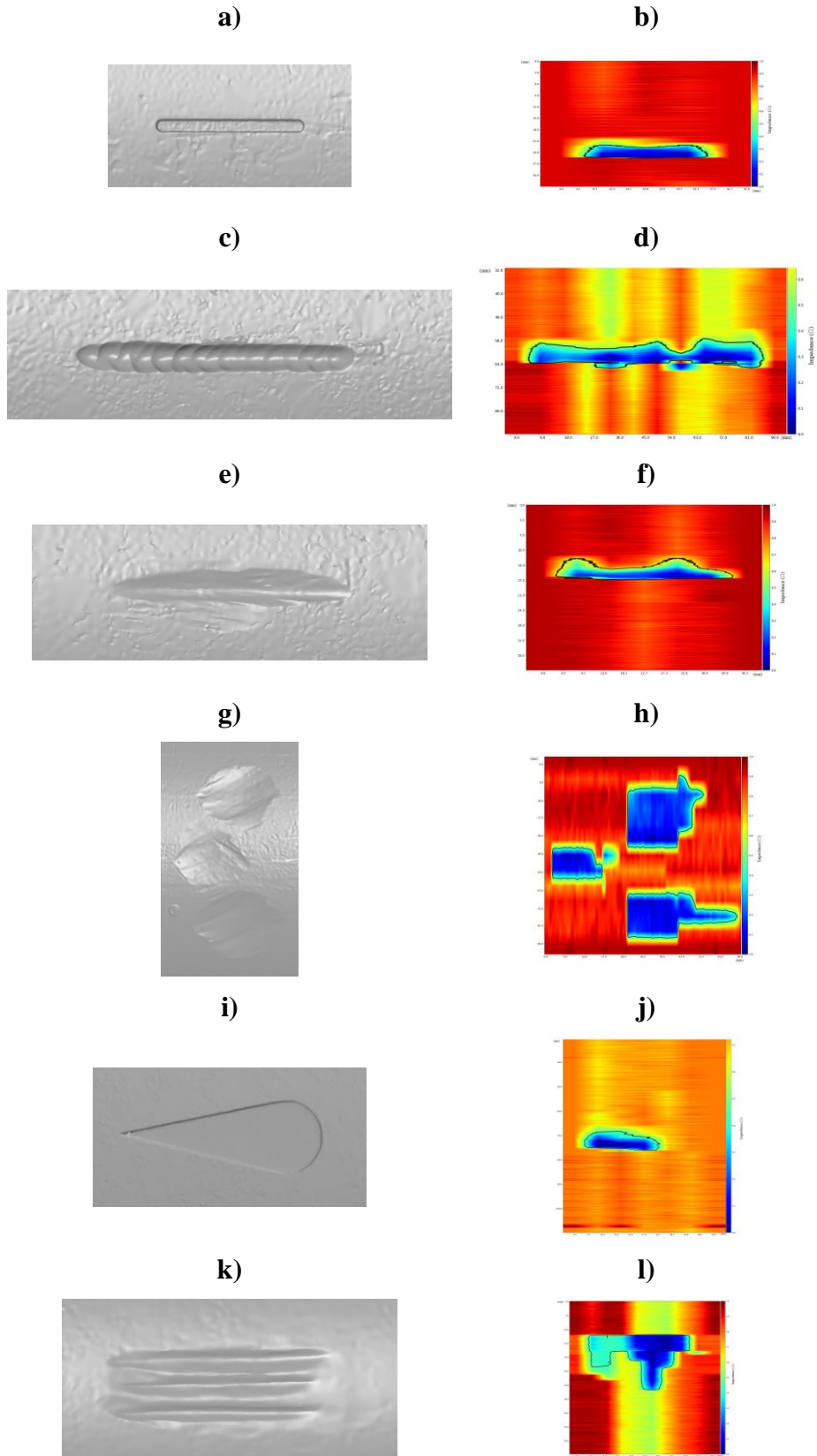
Figure 5. 72: Reconstruction of defects by structured light respectively in a), c), e), g), i) and k) with their respective maps and contours made by the developed algorithm using HGP data in b), d), f), h), j) and l).

The Table 5.31 shows the nominal differences between the main values extracted by the developed algorithm from HGP's data with the real defect's values measured by SLS commercial software from the digital twin data.

Table 5. 31: Differences of measures between the SLS measures on SLS commercial software and the HGP's from the developed algorithm.

Defect	Length (mm)	Width (mm)	Depth (mm)	Perimeter (mm)	Area (mm²)
Defect 1	-3.36	-2.00	-0.12	-8.31	-32.67
Defect 2	-0.26	-1.18	0.02	-10.13	-25.36
Defect 3	1.48	1.72	-0.12	-8.43	-28.42
Defect 4	0.00	-1.35	0.06	21.53	-31.53
Defect 10	2.78	1.60	0.06	-26.16	14.13
Defect 11	-2.89	0.57	-0.11	-30.16	25.34
Defect 12	4.37	1.98	-0.05	-25.61	18.97
Defect 25	-3.34	-0.13	0.10	-43.71	-78.38
Defect 27	-2.23	-3.10	-0.24	-6.31	-9.71
Defect 28	-0.37	1.03	-0.22	4.38	0.16
Defect 32	-0.30	-2.05	-0.10	0.51	-37.92

In order to analyze the precision of HGP's results on the developed algorithm, it was first investigated if the difference error for length, width and depth would also behave as a random sampling from normal distribution on Minitab. It was possible to visually compare the PDPD, as can be seen in Figure 5.73. It can be observed that the depth has also a greater precision, because its curve is narrower compared to the length and width curves. Both the length and the width have very similar accuracies, because their curves have the same tendency. Unlike the lateral and longitudinal resolution that depend, respectively, on the inspection steps and the encoder acquisition rate, the depth comes from the calibration shown in section 5.33 and, therefore, has more accurate results. Then it was performed an Anderson-Darling test (Stephens, 1974) for each dimension, as shown in Figure 5.74.
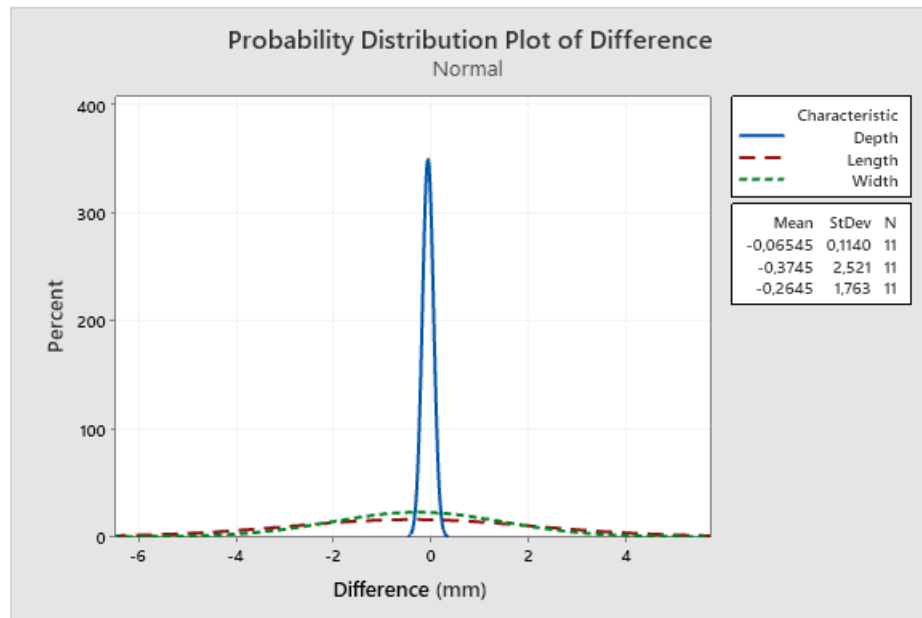
Figure 5. 73: Probability distribution plot of the difference between HGP and developed algorithm.
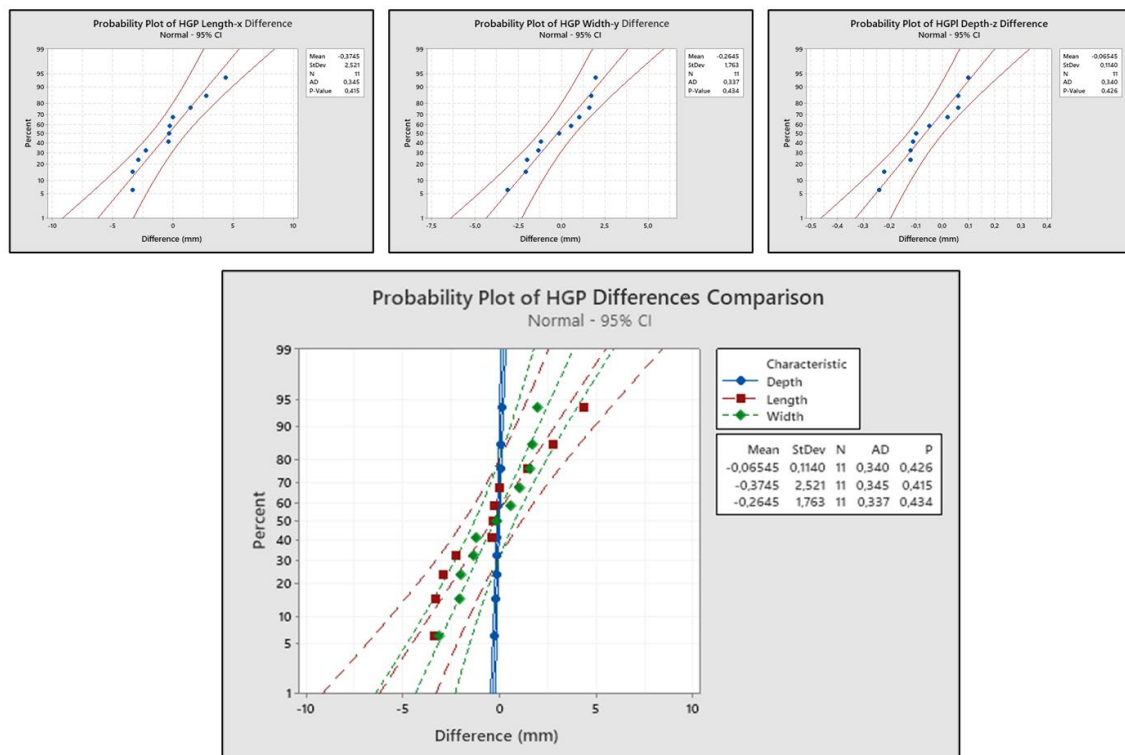
Figure 5. 74: Anderson-Darling test to verify if the difference HGP data could be treated as normally distribute.

In Table 5.32 all the parameters could be treated as normally distributed as the data p-value was higher than the critical AD value for each case. Thus, resulting in an average error of only 0.4 mm for the length and width and close to zero error in depth data (-0.07mm). Based on the collected data for length, width and depth data is expected that the results will be comprehended mostly between -3.36 mm and 4.37 mm maximum error for the length, -3.10 mm and 1.98 mm for width and -0.24 mm and 0.10 mm for depth.

Table 5. 32: Statistical evaluation of the measurement errors.

Dimension	Average (mm)	Standard Deviation (mm)	Minimum (mm)	Maximum (mm)	P_value (-)	AD_stat (-)
Length	-0.37	2.52	-3.36	4.37	0.415	0.345
Width	-0.26	1.76	-3.10	1.98	0.434	0.337
Depth	0.06	0.11	-0.24	0.10	0.426	0.340

As already clarified the Gaussian probability distribution chart cannot be used to evaluate the results for the perimeter and area because they do not follow a normal data distribution. Figure 5.75 shows the Weibull result of three parameters for the perimeter results and Figure 5.76 for the area results. In addition, the AD test is also applied to check whether the data can be represented by the Weibull of three parameters and, consequently, the accuracy of the results obtained by the developed algorithm can be evaluated.
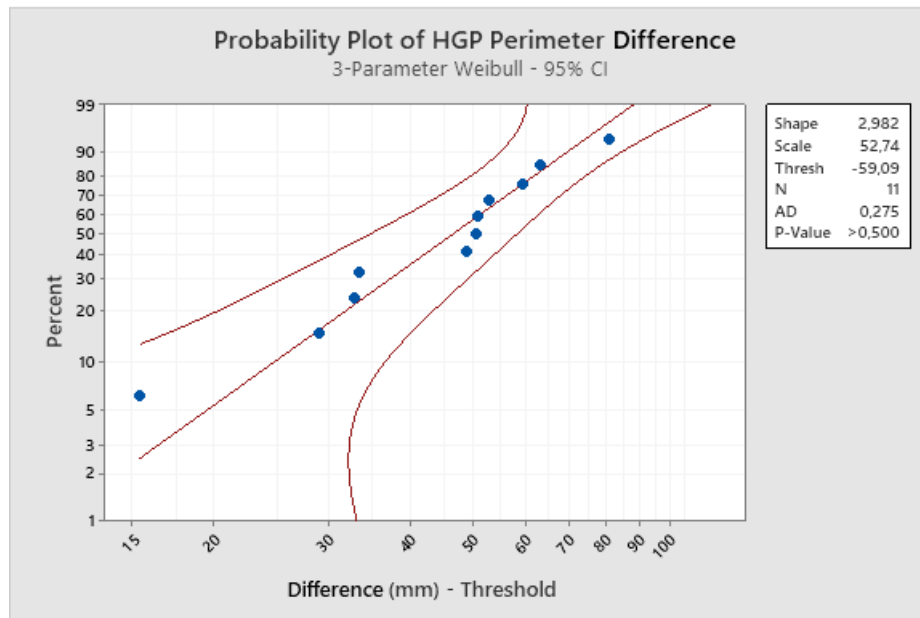
Figure 5. 75: Anderson-Darling test to verify if the difference HGP data of perimeter could be treated as 3 parameter Weibull distribution.
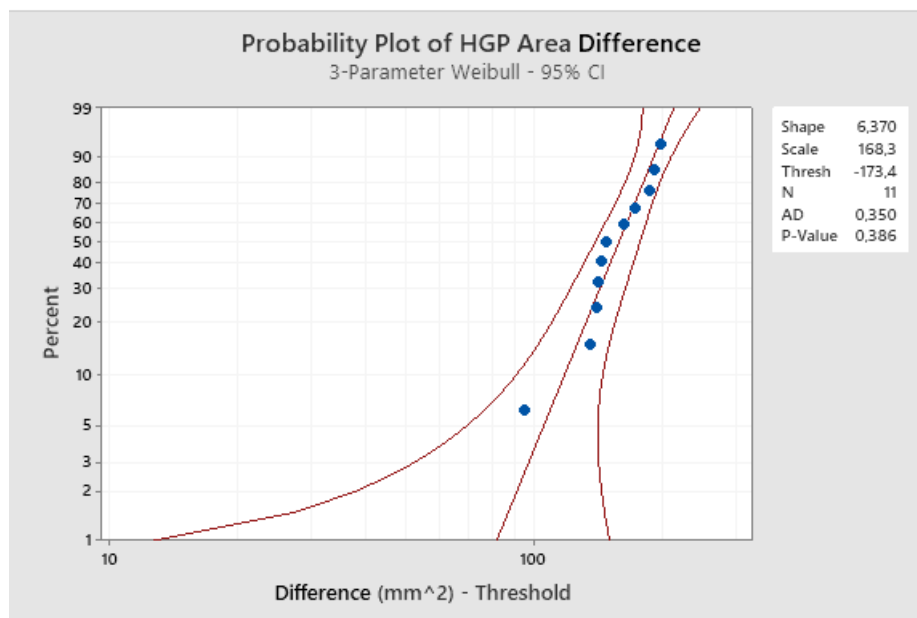
Figure 5. 76: Anderson-Darling test to verify if the difference HGP data of area could be treated as 3 parameter Weibull distribution.

As the p-value is higher than the AD-value for both the perimeter and the area, it can be stated that the in Table 5.33 all the parameters could be treated as 3-Parameter Weibull distribution. The obtained error median was of -8.43 mm for the perimeter and

176

-25.36 mm^2 for area data. Based on the collected data is expected that the results will be comprehended mostly between -43.70 mm and 21.53 mm maximum error for the perimeter and -78.38 mm^2 and 25.34 mm^2 for area. In addition, it can still be noted that the majority of the data is contained between -26.16 mm and 0.51 mm for the perimeter and between -32.67 mm^2 and 14.13 mm^2 for the area.

Table 5. 33: Statistical evaluation of difference of the measurement errors.

Dimension	Perimeter	Area
Median	-8.43 mm	-25.36 mm^2
First quartile	-26.16 mm	-32.67 mm^2
Third quartile	0.51 mm	14.13 mm^2
Minimum	-43.71 mm	-78.38 mm^2
Maximum	21.53 mm	25.34 mm^2
P_value	>0.500	0.386
AD_stat	0.275	0.350

Also based on the measurements made by the algorithm on HGP data, the process of classification of defects was performed. The following Table 5.34 shows the result for the classification of the defects inspected by HGP and processed by the developed algorithm. As it can be observed, still in Table 5.34, the algorithm classification response for the 11 inspected data defects was also excellent since there was only two deviation from reality. This deviation occurred for defect 1 and defect 28, where the developed algorithm indicated a non-conservative response for the severity of defect 1 and indicate defect 28 as a Scratch while it is a crack. As already mentioned, this question can be easily resolved by inserting a safety margin or even a variation in the rule for determining the severity of the defect, according to the required demand.

Table 5. 34: HGP's classification of defects according to their orientation, morphology and severity (by color scale).

	Real (Orientation / Morphology)	Algorithm (Orientation / Morphology)
Defect 1	**Circular / Dent**	**Circular / Dent**
Defect 2	**Circular / Dent**	**Circular / Dent**
Defect 3	**Circular / Dent**	**Circular / Dent**
Defect 4	**Longitudinal / Scratch**	**Longitudinal / Scratch**
Defect 10	**Longitudinal / Scratch**	**Longitudinal / Scratch**
Defect 11	**Longitudinal / Scratch**	**Longitudinal / Scratch**
Defect 12	**Longitudinal / Scratch**	**Longitudinal / Scratch**
Defect 25	**Longitudinal / Scratch**	**Longitudinal / Scratch**
Defect 27	**Longitudinal / Scratch**	**Longitudinal / Scratch**
Defect 28	**Longitudinal / Crack**	**Longitudinal / Scratch**
Defect 32	**Longitudinal / Scratch**	**Longitudinal / Scratch**

HGP technique demonstrated its good performance on the results for the developed algorithm. It was possible to observe its efficiency in automatically analysing the data obtained by HGP. Not only that, but it was also possible to observe the algorithm's good performance on defect recognition and evaluation with an accuracy conservatively stated for length and width of ± 4.0 mm, the depth of ± 0.5 mm, the perimeter of 50 mm and the area of 80 mm^2 and, in addition, it was demonstrated the functionality regarding defect's orientation, morphology and severity.

6. Final considerations

After the presentation, analysis and discussion of the results in the previous chapter, the following main conclusions can be reached:

− The structured light technique demonstrated to be an excellent technique as reference system for the LL, EC and HGP techniques studied along this work. It allowed the precise construction of the inspected surface samples digital twin, as well as their evaluation through the manual commercial SLS software with precision in the micrometer magnitude;

− The results achieved with the automatic laser line inspection based on the optimized parameters developed showed the technique's ability to reconstruct tubular surfaces in great detail. Even with a higher data volume when compared to the SLS, it was possible to process the data automatically, obtaining dimensional measurement results equivalent to those obtained by the SLS. Moreover, a great advantage of this technique is its dynamic operation and high data acquisition rate leading, consequently, to a large spatial resolution;

− The hybrid configuration of the proposed electromagnetic system proved to be a promising solution for the detection of surface defects on tubular surfaces, aiming at the automation of the inspection process into the pipe mill. Both laboratory and field test results proved that the developed system is able not only to detect defects up to 1 mm^3 but also to have robustness during production line operation;

− An EC probe has been developed especially for the detection of defects in cylindrical surfaces of ferromagnetic materials. The main optimal construction parameters of the developed probe were 8.0 mm diameter, 3.5 mm height, 800 turns of AWG 38 copper wire and 3.5 mm ferrite core. It has been proven both experimentally and by computer simulation that the optimum frequency for surface defect detection by the developed probe is 5 Khz;

– The HGP technique has shown its efficiency for the geometric description of surfaces as well as the detection of long defects with low depth. As for EC, a very important factor of these techniques for its application for automatic detection and classification of surface defects is its lateral resolution. In order to achieve more precise results in terms of defect geometry, the distance between the sensors in the test matrix must be reduced as much as possible;

– The developed algorithm has demonstrated excellent results in the field of automatic defect recognition and classification from different data sources. From the statistical analysis of the data obtained by the algorithm and its difference between the main geometric characteristics of the defects measured in the reference of the digital twin, it was demonstrated that the data from the LL are equivalent to those from the SLS, due to the proximity of its averages and standard deviation. Thus, it is shown the application of the LL methodology developed together with the optimization of parameters in a reliable, accurate and efficient way for dynamic inspections. The analysis of the results also shows that the average error of HGP depth is equivalent to the results found for LL and SLS data, based on the average error values, being so a great tool to monitor difference on the depth geometry tubular goods. EC results for length and width showed the greatest error dispersion, due to the amplitude of the maximum and minimum values of the analyzed data set and also due to the value of being standard deviation. The results for perimeter and area measurements for EC and HGP data also have a high dispersion due to the lateral resolution employed, i.e., they can be improved by decreasing the distance between the inspection steps or sensors;

Differently from what has been found so far both in the literature and in the market, this work has developed the concept of the hybridization of electromagnetic and optical techniques aiming at the automation of surface inspection. Besides developing an electromagnetic methodology, with optimized sensors for cylindrical surfaces, and an optical methodology, it was also presented a unique concept through the algorithm developed to be able to automatically process data from different sources, recognizing, characterizing and automatically classifying the defects detected.

7. Outlook and further studies

Following below are recommendations for future work:

− Construction of LL-based system and electromagnetic techniques in the same prototype;

− Perform tests to formulate the relation of the impedance response voltage of the ECs to the depth of defects;

− To test algorithm developed for a matrix with more defects and different types, in relation to its morphology, orientation and depth;

− To verify limitations of the industrial environment for prototype based on the optical system;

8. References

Abu-Nabah, B. A., 2018, "Eddy current evaluation of metallic coating thicknesses over nonmagnetic metals". *IOP Conference Series: Materials Science and Engineering,* 372, Japão.

Abu-Nabah, B. A., Nagy, P. B., 2007, "Lift-off effect in high-frequency eddy current conductivity spectroscopy". *NDT&E International*, v.40, pp. 555-565 .

Ali, A. A., Yanling, G., Zifan, C., 2017, "Study of hall effect sensor and variety of temperature related sensitivity", *Journal Eng. Technol. Sci.*, v. 49, n. 3, pp. 308-321.

ALTERNATIVES, C. -C. (2009, 4 21). Patent No. US8270254/EP2269054.

Altschuler., J. P., 1982, "Surface measurement by space-encoded projected beam systems", *Computer Graphics and Image Processing*, v. 18, n. 1, pp. 1-17.

Ames, N., LaMorte, C. R., 2012, "Laser based inspection for welds and pipeline corrosion", *EWI Technical Brief*.

Amid, E., Aghdam, S. R., Amindavar, H., 2012, "Enhanced performance for support vector machines as multiclass classifiers in steel surface defect detection", *International Journal of Electrical and Computer Engineering*, v. 6, n. 7, pp. 693-697.

Amza, C. G., & Cicic, D., 2015, "Industrial image processing using fuzzy-logic", *Procedia Engineering*, v.100, pp. 492-498.

Amza, C. G., Gheorghe, A., Nitoi, D., Luchian, C., 2008, "Fuzzy logic for non-destructive testing for various composite materials", *Nonconventional Technologies Review*, n. 4, pp. 27-34.

AZANI, A. L., & GUITIERREZ, J. A., 2008, "Surface inspection of hot rolled seamless tube", *MPT International*.

Benhadda, N., Bouchala, T., Guettafi, A., Abdelhadi, B., 2014, "Study of the influence of conductive defect characteristics on eddy current differential probe signal", *Journal of Electrical Engineering*, v. 14.

Breuckmann, B., 2014, "25 Years of high definition 3d scanning: history, state of art, outlook". *Eletronic Visualization and the Arts*, 10.14236/ewic/eva2014.31.

Brid, R. S., "Decision Trees: a simple way to visualize a decision". Disponível em: https://medium.com/greyatom/decision-trees-a-simple-way-to-visualize-a-decision-dc506a403aeb. Acesso em: 05 maio de 2019.

Bowler, N., 2019, "Eddy-current nondestructive evaluation!, 1 ed. New York, Springer-Verlag.

Camerini, C. G., 2012, "Desenvolvimento de sondas de correntes parasitas para detecção e quantificação de fase sigma em aço inoxidável duplex". Dissertação de M.Sc., COPPE/UFRJ, Rio de Janeiro, RJ, Brasil.

CAMERINI, C. G., 2018, "Sistema de inspeção para detecção de trincas de fadiga em juntas soldadas de dutos metalurgicamente cladeados". Tese de D.Sc., COPPE/UFRJ, Rio de Janeiro, RJ, Brasil.

NDT Resource Center. Probes - Mode of operation. Disponível em: https://www.nde-ed.org/EducationResources/CommunityCollege/EddyCurrents/ProbesCoilDesign/ProbesModeOp.htmRetrieved. Acesso em: 04 mar. 2019.

Chady, T., Enokizono, M., Sikora, R., 1999, "Crack detection and recognition using an eddy current differential probe", *IEEE Transactions on Magnetics*, v. 35, pp. 1849-1852.

Chaiba, S., Ayad, A., Ziani, D., Le Bihan, Y., García, M. J., 2018, "Eddy current probe parameters identification using a genetic algorithm and simultaneous perturbation stochastic approximation", *Journal of Nondestructive Evaluation*, v. 37, n. 55, pp. 1-7.

Chen, Z., Miya, K., 1998, "A new approach for optimal design of eddy current testing probes" *J Nondestruct Eval*, v. 17, pp. 105–116.

Cho, D. H., Lee, S. L., 2013, "Defect Classification Using Machine Learning Techniques for Flat Display Panels", *Applied Mechanics and Materials*, v. 365-366, pp. 720–724.

"EN 13018: Non-destructive testing - visual testing - general principles", Comite Europeen de Normalisation, 2016

Correa, M. P., 2017, "Caracterização magnética da microestrutura de diferentes estados de envelhecimento de uma liga austenítica HP modificada ao Nb-Ti". Tese de D.Sc., COPPE/UFRJ, Rio de Janeiro, RJ, Brasil.

Curless, B. L., 1997, "New methods for surface reconstruction from range images". Thesis of PhD, Stanford University, California, United Stats.

D'Angelo, G. &., 2015, "Shape-based defect classification for Non-destructive testing", *2nd IEEE International Workshop on Metrology for Aerospace, MetroAeroSpace 2015 - Proceedings*, pp. 406-410.

Eisenbeis, R., 2014, "Understanding & Applying Hall Effect Sensor Datasheets", Texas Instruments, SLIA086.

ENVISION, Encyclopedia of Machine Vision. Disponível em: https://blog.envision.co.kr/47. Acesso em: 10 jul 2019.

Fernandes, N. T., 2012, "Reconstrução de Superfícies usando um Scanner 3D de Luz Estruturada". Dissertação de M.Sc., Instituto Superior de Engenharia do Porto, Porto, Portugal.

FREITAS, M. A., 2009, "Monitoramento de tensão mecânica em risers flexíveis por eletromagnetismo". Tese de D.Sc., PUC, Rio de Janeiro, RJ, Brasil.

García, M. J., Gil, J. G., Sánchez, E. V., 2011, "Non-destructive techniques based on eddy current testing", *Sensors Journal*, v. 11, pp. 2525-2565.

Gedney, S., 1994, "The finite element method in electromagnetics", *Antennas and Propagation Magazine*.

Geng, J., 2011, "Structured-light 3D surface imaging: a tutorial", *Advances in Optics and Photonics*, v. 160, n. 2, pp. 128–160.

Giachino, J. M., 1986, "Smart sensors", *Sensors and Actuators Journal*, v. 10, pp. 239-248.

Giesko T., Z. A., 2007, "Laser profilometers for surface inspection and profile measurement", *Problemy Eksploatacji*, v. 1, pp. 97-108.

Gross, J. L., Yellen, J., Zhang, P., 2013 "Handbook of graph theory" Chapman and Hall/CRC.

Goldfine, N., Sheiretov, Y., 2008, "System identification for NDT, using sensor response databases", *Materials Evaluation*.

Goumeidane, A. B., Bouzaieni, A., Nacereddine, N., & Tabbone, S., 2015, "Bayesian Networks-Based Defects Classes Discrimination in Weld Radiographic Images", G. Azzopardi and N. Petkov (Eds.), CAIP 2015, Switzerland, Part II, LNCS 9257,, pp. 554-565, Springer International Publishing.

Griffiths, D. J., 1999, "Introduction to Electrodynamics*"*, 3 ed. New Jersey, Prentice Hall .

Guyon, I., Elisseeff, A., 2006, "An Introduction to Feature Extraction", In I. Guyon, S. Gunn, M. Nikravesh, & L. Zadeh ed., Berlin, Springer.

Krause, H. J., Kreutzbruck, M. V., 2002, "Recent developments in SQUID NDE", *Physica C: Superconductivity*, v. 368, pp. 70–79.

Heremans, J., 1993, "Solid state magnetic field sensors and applications" *Journal of Physics D: Applied Physics*, v. 26, n. 8, pp. 1149–1168.

Jander, A., Smith, C., Schneider, R., 2005, "Magnetoresistive sensors for nondestructive evaluation", *Advanced Sensor Technologies for Nondestructive Evaluation and Structural Health Monitoring*, SPIE 5770, San Diego, CA, United Stats.

Kang, S., Lee, J. H., Song, K. Y., Pahk, H. J., 2009, "Automatic defect classification of TFT-LCD panels using machine learning", *IEEE International Symposium on Industrial Electronics, pp. 2175-2177*.

Karthik, V. U., Mathialakan, T., Jayakumar, P., 2015, "Coil positioning for defect reconstruction in a steel plate". *31st International Review of Progress in Applied Computational Electromagnetics (ACES)*, Williamsburg, VA, 2015, pp. 1-2.

Kokubum, C., Tommaselli, A., Reiss, M., 2005, "Classificação Automática de Padrões Projetados por um Sistema de Luz Estruturada", *Boletim de Ciências Geodésicas*, v. 11, n. 1, pp. 89-116.

Kumar, G., Bhatia, P., 2014, "A Detailed Review of Feature Extraction in Image Processing Systems", *IEEE Fourth International Conference on Advanced Computing & Communication Technologies*. Rohtak, Haryana, India.

Kuntze, H. B., Haffner. H., 1998, "Experiences with the development of a robot for smart multisensoric pipe inspection", *Robotics and Automation, Proceedings*.

Latimer, W., "Understanding laser-based 3D triangulation methods". Disponível em: https://www.vision-systems.com/articles/print/volume-20/issue-6/features/understanding-laser-based-3d-triangulation-methods.html. Acesso em: 09 jun 2019.

Legarda-Saenz, R., Bothe, T., & Jüptner, P. W., 2004, "Accurate procedure for the calibration of a structured light system", *Optical Engineering*, v. 43, n. 2, pp. 464-471.

Malcomb, J. R., 2014, "Laser Profilometry For Non-Contact Automated Countersink Diameter Measurement", *SAE International Journal of Aerospace*, v. 7, pp. 263-268.

Marani, R., Roselli, G., Nitti, M., Cicirelli, G., D'Orazio, T., Stella, E. (2013). « A 3D vision system for high resolution surface reconstruction". Seventh International Conference on Sensing Technology (ICST), 10.1109/ICSensT.2013.6727634.

Martin, J. G., Gil, J. G., Sánchez, E. V., 2011, "Non-destructive techniques based on eddy current testing', Sensors Journal, vol. 11, pp. 2525-2565.

Miresmailli, S., Badulescu, D., Mahdaviani, M., Zamar, R., Isman, M., 2007, "Integrating plant chemical ecology, sensors and artificial intelligence for accurate pest monitoring", *In Tomatoes: Agricultural procedures, pathogen interaction and health effects*, Nova Science Publishers.

Montilla, M., Orjuela-Vargas, S., Philips, W., 2014, "State of the art of 3D scanning systems and inspection of textile surfaces". The International Society for Optical Engineering, 9018.

Multiphysics, C. Disponível em: https://br.comsol.com/release/5.4. Acessado em: 18 abr 2019.

NDT Resource Center, Impedance plane diagram. Disponível em: https://www.nde-ed.org/EducationResources/CommunityCollege/EddyCurrents/Instrumentation/impedanceplane.htm. Acesso em: 04 abr. 2019.

Ng, A., 2013, "Video Endoscopic Metrology for Pipeline Welding", *Singapore International NDT Conference & Exhibition.*

NOVKOVSKI N., 2006, "Progress and limitations in magnetic field measurements", Dordrecht, Springer,

Okabe, A., et al., 2009, "Spatial tessellations: concepts and applications of Voronoi diagrams", *John Wiley & Sons*, v. 501.

Olympus. Disponível em: http://www.olympus-ims.com/en/omniscan-eca/. Acesso em: 15 set. 2019.

Pascucci, V., "2D Scalar Visualization". Disponível em: http://www.sci.utah.edu/~pascucci/classes/2009_fall/files/lec06-07-notes.pdf. Acesso em: 3 mar 2019.

Pereira, D., 2014, "Avaliação do método de correntes parasitas para caracterização microestrutural e inspeção de defeito". Dissertação de M.Sc. UFRGS, Porto Alegre, RS, Brasil.

Pernkopf, F., 2004, "Detection of surface defects on raw steel blocks using Bayesian network classifiers", London, Springer-Verlag.

Pfeifer, N., & Briese, C., 2007, "Laser scanning – principles and applications". International Exhibition and Scientific Congress.

RP Photonics, "Scanning Lenses". Disponível em: https://www.rp-photonics.com/scanning_lenses.html. Acesso em 12 jul. 2019.

Pikas, J., 2007, "Understanding 3D Strctured Light to Assess Corrosion Defects", *Automation Science and Engineering*, pp. 118-126.

Pohl, R., Erhard, A., Montag, H. J., Thomas, H., Wüstenberg, H., 2004, "NDT techniques for railroad wheel and gauge corner inspection", *NDT E Int*, v. 37, pp. 89-94.

Popovic, R. S., Flanagan, J., Besse, P., 1996, "The future of magnetic sensors", *Sensors and Actuators*, v. 56, pp. 39-55.

Portas, R., Colombel, L., 2007, "Accuracy of Hall-Effect current measurement transducers in automotive battery management applications using current integration", *Automotive Power Electronics*, pp. 1-8.

Press, W. H., Teukolsky, S. A., Vetterling, W. T., Flannery, B. P., 1992, "Numerical recipes in C: the art of scientific computing", 2 ed. New York, Cambridge University Press.

Reiss, M., 2007, "Reconstrução tridimensional digital de objetos à curta distância por meio de luz estruturada". Tese de D.Sc., Universidade Estadual Paulista, São Paulo, Brasil.

Rocha, T. J., Ramos, H. G., Ribeiro, A. L., 2015, "Magnetic sensors assessment in velocity induced eddy current testing", *Sensor Actuat A-Phys*, v. 228, pp. 55–61.

Salvi J., F. S., 2010, "A state of the art in structured light patterns for surface profilometry", *Pattern Recognition*, v. 43, n. 8, pp. 2666–2680.

Sansoni, G., Trebeschi, M., Docchio, F., 2009, "State-of-The-Art and Applications of 3D Imaging Sensors in Industry, Cultural Heritage, Medicine, and Criminal Investigation", *Sensors Journal*, v. 9, pp. 568-601.

Schroeder, W., Martin, K., & Lorensen, B., 2006, "The Visualization Toolkit: An Object-Oriented Approach To 3D Graphics", Kitware, 4 ed. United States.

Schwarte R., X. Z., 1997, "New electro-optical mixing and correlating sensor: facilities and applications of the photonic mixer device (PMD)", *SPIE*, v. 3100, pp. 245–253.

Silva, L. K., 2018, "Detecção de trincas por correntes parasitas de liga austenítica HP modificada ao Nióbio". Dissertação de M.Sc., COPPE&UFRJ, Rio de Janeiro, RJ, Brasil.

Silva, V. M., 2016, "Caracterização por correntes parasitas de aços inoxidáveis austeníticos deformados a frio". Dissertação de M.Sc. COPPE/UFRJ, Rio de Janeiro, RJ, Brasil.

Slobodnk, K., 2017, "Detection and evaluation of subsurface defects using pulse eddy current differential probe", *18th International Conference on Computational Problems of Electrical Engineering (CPEE)*.

Song, J., Kim, Y., Park, T., 2018, "SMT defect classification by feature extraction region optimization and machine learning", *International Journal of Advanced Manufacturing Technology*.

Stephens, M. A., 1974, "EDF statistics for goodness of fit and some comparisons", *Journal of the American Statistical Association*, v. 69, pp. 730 – 737.

Summan, Rahul, Jackson, William, Dobie, Gordon, Macleod, Charles, Mineo, Carmelo, West, Graeme, offin, Doug, Bolton, Gary, Marshall, Stephen, Lille, Alexander, 2017, "A Novel Visual Pipework Inspection System", *AIP Conference Proceedings*.

Sumesh, A., Nair, B. B., Santhakumari, A., Raja, A., Mohandas, K., 2018, "Decision tree based weld defect classification using current and voltage signatures in GMAW process", *Materials Today: Proceedings*, v. 5, pp. 8354-8363.

Thielenmann, J., Skotheim, O., Berg, A., 2009, "Optical 3D measurements aid Pipeline Inspecction", *SPIE Newsroom*.

Törnblom, N., 2010, "Underwater 3D Surface Scanning using Structured Light". Thesis project, Uppsala Universitet, Uppsala, Sweden.

Tumanski, S., 2013, "Modern magnetic field sensors - a review" *Przeglad Elektrotechniczny*, v. 89, pp. 1-12.

Vilela, A. R., 2008, "Uma metodologia para reconstrução de superfícies a partir de luz estruturada". Dissertação de M.Sc. Universidade Federal de Juiz de Fora, Brasil.

Wang, Y., & Guo, H., 2014, "Application of Support Vector Machine in Weld Defect Detection and Recognition of X-ray Images", *Computer Aided Drafting, Design and Manufacturing*, v. 24, n. 3, pp. 22-26.

Weid, J. P., Camerini, C., Freitas, M, Salcedo, T., 2008, "Feeler Pig: a simple way to detect and size internal corrosion", *7th International Conference*, Alberta, Canada, IPC2008-64626.

Wilm, J. A., 2015, "Real Time Structured Light and Applications". Thesis of PhD. Technical University of Denmark, Denmark.

Yang, X., Feng, Y., Li, S., 2018, "Influence of Measuring Coil Geometry on Detection Performance of Eddy Current Sensor", *IOP Conference Series: Materials Science and Engineering*, v. 452.

Yin, L., Ye, B., Zhang, Z., Tao, Y., Xu, H., Salas Avila, J., & Yin, W. (2019). "A novel feature extraction method of eddy current testing for defect detection based on machine learning". NDT & E International.

Yin, Y., Tian, G. Y., Yin, G. F., Luo, A. M., 2008, "Defect Identification and Classification for Digital X-Ray Images", *Applied Mechanics and Materials*, v. 10-12, pp. 543-547.

Zahran, O., Al-Nuaimy, W., 2004, "Automatic Defect Classification in Time-Of-Flight-Diffraction Data Using Fuzzy Logic", *43rd Annual British Conference on Non-Destructive Testing*, v. 14 -16, Torquay, United Kingdom.

Zhang, S., 2018, "High-speed 3D shape measurement with structured light methods: A review", *Optics and Lasers in Engineering*, v. 106, pp. 119-131.

Zhang, S., Huang, P. S., 2006, "Novel method for structured light system calibration", *Optical Engineering*, v. 45, pp. 1-8.

Zhou, H., Hou, K., Pan, H., Chen, J., Wang, Q., 2015, "Study on the Optimization of Eddy Current Testing Coil and the Defect Detection Sensitivity", *Procedia Engineering*, v. 130, pp. 1649-1657.

Zhuang, B. H., Zhang, W., Cui, D. Y., "Noncontact laser sensor for pipe inner wall inspection", *Optical Engineering*, v. 37, n. 5.

Zilberstein, V., Shaz, I., Lyons, R., Golfine, N., Malow, T., Reiche, R., 2013, "Validation of multi-frequency eddy-current MWM sensors and MWM-Arrays for coating production quality and refurbishment assessmen", *ASME Turbo Expo*, pp. 581-590.